

Forschungsberichte
aus
dem Institut
für Höchstfrequenztechnik
und Elektronik
der
Universität Karlsruhe (TH)

Herausgeber:
Prof. Dr.-Ing. W. Wiesbeck

Marwan Younis

Digital Beam-Forming for High Resolution Wide Swath Real and Synthetic Aperture Radar

Copyright: Institut für Höchstfrequenztechnik und Elektronik
Universität Karlsruhe (TH)

alle Rechte vorbehalten

Druck: Druckerei Gunter Dünnbier, 02779 Großschönau,
Tel. 035841-36757

ISSN: 0942-2935

Vorwort des Herausgebers

Als Anfang der 60-iger Jahre die vorteilhafte Nutzung der digitalen Technik gegenüber der analogen Technik in vielen Bereichen erkennbar wurde, waren die meisten der analogen Technik nahe stehenden Ingenieuren und Wissenschaftler verunsichert. Es wurden Fronten aufgebaut und in zahlreichen Publikationen nachgewiesen, warum die digitale Technik nicht leistungsfähig ist. Diese Einstellungen gehören zwischenzeitlich der Vergangenheit an. Die nachkommenden Generationen an Ingenieuren und Wissenschaftlern standen digitalen Problemlösungen offener gegenüber. Heute hat die Digitaltechnik in vielen Bereichen vorteilhaft die analoge Technik abgelöst. Um dies zu untermauern, muss man sich nicht auf die Errungenschaften in der Computertechnik beschränken. Herausragende Beispiele sind auch der digitale Mobilfunk, die digitale Fotografie und der digitale Rundfunk. Wie sehr gerade beim Letzteren die analoge Technik verwurzelt war und ist, zeigt sich daran, dass das Wort digital in den Bezeichnungen DAB, DVB-T explizit verwendet wird. So sind zwischenzeitlich die meisten analogen Basisstationen gefallen. Hartnäckig hält sich allerdings die analoge Technik in der Formung der Richtcharakteristiken von Antennen. Die Dissertation von Dr. Younis liefert in diesem Bereich grundlegende Beiträge zum sog. *digital beam-forming* speziell für die Radarsensorik. Hierfür wird in Mehrantennensystemen durch geeignete Raum-Zeit Signalverarbeitung eine äußerst flexible Strahlformung erreicht. Es steht zu erwarten, dass Inhalte der Arbeit in wenigen Jahren zahlreiche monostatische und bistatische Radaranwendungen revolutionieren werden.

Forschungsberichte aus dem Institut für Höchstfrequenztechnik und Elektronik der Universität Karlsruhe (TH)

Herausgeber: Prof. Dr.-Ing. Werner Wiesbeck

- Band 1 Daniel Kähny
Modellierung und meßtechnische Verifikation polarimetrischer, mono- und bistatischer Radarsignaturen und deren Klassifizierung
- Band 2 Eberhardt Heidrich
Theoretische und experimentelle Charakterisierung der polarimetrischen Strahlungs- und Streueigenschaften von Antennen
- Band 3 Thomas Kürner
Charakterisierung digitaler Funksysteme mit einem breitbandigen Wellenausbreitungsmodell
- Band 4 Jürgen Kehrbeck
Mikrowellen-Doppler-Sensor zur Geschwindigkeits- und Wegmessung - System-Modellierung und Verifikation
- Band 5 Christian Bornkessel
Analyse und Optimierung der elektrodynamischen Eigenschaften von EMV-Absorberkammern durch numerische Feldberechnung
- Band 6 Rainer Speck
Hochempfindliche Impedanzmessungen an Supraleiter / Festelektrolyt-Kontakten
- Band 7 Edward Pillai
Derivation of Equivalent Circuits for Multilayer PCB and Chip Package Discontinuities Using Full Wave Models
- Band 8 Dieter J. Cichon
Strahlenoptische Modellierung der Wellenausbreitung in urbanen Mikro- und Pikofunkzellen
- Band 9 Gerd Gottwald
Numerische Analyse konformer Streifenleitungsantennen in mehrlagigen Zylindern mittels der Spektralbereichsmethode
- Band 10 Norbert Geng
Modellierung der Ausbreitung elektromagnetischer Wellen in Funksystemen durch Lösung der parabolischen Approximation der Helmholtz-Gleichung

Forschungsberichte aus dem Institut für Höchstfrequenztechnik und Elektronik der Universität Karlsruhe (TH)

- Band 11 Torsten C. Becker
Verfahren und Kriterien zur Planung von Gleichwellennetzen für den Digitalen Hörrundfunk DAB (Digital Audio Broadcasting)
- Band 12 Friedhelm Rostan
**Dual polarisierte Microstrip-Patch-Arrays für zukünftige satelliten-
gestützte SAR-Systeme**
- Band 13 Marcus Demmler
**Vektorkorrigiertes Großsignal-Meßsystem zur nichtlinearen
Charakterisierung von Mikrowellentransistoren**
- Band 14 Andreas Froese
Elektrochemisches Phasengrenzverhalten von Supraleitern
- Band 15 Jürgen v. Hagen
**Wide Band Electromagnetic Aperture Coupling to a Cavity: An
Integral Representation Based Model**
- Band 16 Ralf Pötzschke
**Nanostrukturierung von Festkörperflächen durch elektrochemische
Metallphasenbildung**
- Band 17 Jean Parlebas
**Numerische Berechnung mehrlagiger dualer planarer Antennen mit
koplanarer Speisung**
- Band 18 Frank Demmerle
**Bikonische Antenne mit mehrmodiger Anregung für den räumlichen
Mehrfachzugriff (SDMA)**
- Band 19 Eckard Steiger
**Modellierung der Ausbreitung in extrakorporalen Therapien
eingesetzter Ultraschallimpulse hoher Intensität**
- Band 20 Frederik Küchen
**Auf Wellenausbreitungsmodellen basierende Planung terrestrischer
COFDM-Gleichwellennetze für den mobilen Empfang**
- Band 21 Klaus Schmitt
**Dreidimensionale, interferometrische Radarverfahren im Nahbereich
und ihre meßtechnische Verifikation**

**Forschungsberichte aus dem
Institut für Höchstfrequenztechnik und Elektronik
der Universität Karlsruhe (TH)**

- Band 22 Frederik Küchen, Torsten C. Becker, Werner Wiesbeck
Grundlagen und Anwendungen von Planungswerkzeugen für den digitalen terrestrischen Rundfunk
- Band 23 Thomas Zwick
Die Modellierung von richtungsaufgelösten Mehrwegegebäudefunkkanälen durch markierte Poisson-Prozesse
- Band 24 Dirk Didascalou
Ray-Optical Wave Propagation Modelling in Arbitrarily Shaped Tunnels
- Band 25 Hans Rudolf
Increase of Information by Polarimetric Radar Systems
- Band 26 Martin Döttling
Strahlenoptisches Wellenausbreitungsmodell und Systemstudien für den Satellitenmobilfunk
- Band 27 Jens Haala
Analyse von Mikrowellenheizprozessen mittels selbstkonsistenter finiter Integrationsverfahren
- Band 28 Eberhard Gschwendtner
Breitbandige Multifunktionsantennen für den konformen Einbau in Kraftfahrzeuge
- Band 29 Dietmar Löffler
Breitbandige, zylinderkonforme Streifenleitungsantennen für den Einsatz in Kommunikation und Sensorik
- Band 30 Xuemin Huang
Automatic Cell Planning for Mobile Network Design: Optimization Models and Algorithms
- Band 31 Martin Fritzsche
Anwendung von Verfahren der Mustererkennung zur Detektion von Landminen mit Georadaren
- Band 32 Siegfried Ginter
Selbstkonsistente Modellierung der Erhitzung von biologischem Gewebe durch hochintensiven Ultraschall
- Band 33 Young Jin Park
Applications of Photonic Bandgap Structures with Arbitrary Surface Impedance to Luneburg Lenses for Automotive Radar

**Forschungsberichte aus dem
Institut für Höchstfrequenztechnik und Elektronik
der Universität Karlsruhe (TH)**

- Band 34 Alexander Herschlein
Entwicklung numerischer Verfahren zur Feldberechnung konformer Antennen auf Oberflächen höherer Ordnung
- Band 35 Ralph Schertlen
Mikrowellenprozessierung nanotechnologischer Strukturen am Beispiel von Zeolithen
- Band 36 Jürgen von Hagen
Numerical Algorithms for the Solution of Linear Systems of Equations Arising in Computational Electromagnetics
- Band 37 Ying Zhang
Artificial Perfect Magnetic Conductor and its Application to Antennas
- Band 38 Thomas M. Schäfer
Experimentelle und simulative Analyse der Funkwellenausbreitung in Kliniken
- Band 39 Christian Fischer
Multistatisches Radar zur Lokalisierung von Objekten im Boden
- Band 40 Yan C. Venot
Entwicklung und Integration eines Nahbereichsradarsensorsystems bei 76,5 GHz
- Band 41 Christian Waldschmidt
Systemtheoretische und experimentelle Charakterisierung integrierbarer Antennenarrays
- Band 42 Marwan Younis
Digital Beam-Forming for high Resolution Wide Swath Real and Synthetic Aperture Radar

In Memoriam meinem Großvater Prof. Dr. med. Theodor Burckhart

Digital Beam-Forming for High Resolution Wide Swath Real and Synthetic Aperture Radar

Zur Erlangung des akademischen Grades eines

DOKTOR-INGENIEURS

von der Fakultät für
Elektrotechnik und Informationstechnik
der Universität Fridericiana Karlsruhe (TH)

genehmigte

DISSERTATION

von

Dipl.-Ing. Marwan Younis
aus Las Cruces

Tag der mündlichen Prüfung:

22. Juli 2004

Hauptreferent:

Prof. Dr.-Ing. Werner Wiesbeck

Korreferent:

Prof. Dr.-Ing. Alberto Moreira

Vorwort

Die vorliegende Dissertation entstand während meiner Tätigkeit als wissenschaftlicher Mitarbeiter am Institut für Höchstfrequenztechnik und Elektronik der Universität Fridericiana Karlsruhe. Mein Dank gilt besonders Herrn Prof. Dr.-Ing. Werner Wiesbeck, dem Leiter des Instituts, dessen Engagement und Unterstützung wesentlich für das Gelingen meiner Arbeit war. Ferner gilt mein Dank Herrn Prof. Dr.-Ing. Alberto Moreira vom Deutschen Zentrum für Luft- und Raumfahrt für die Übernahme des Korreferats als auch für die fachliche Unterstützung und seinen konstruktiven Vorschlägen. Besonders verbunden bin ich Herrn Dr.-Ing. Christian Fischer und Dr.-Ing. Alexander Herschlein, die trotz ihrer geschäftlichen Verpflichtungen, immer die Zeit für eine kritische Durchsicht meiner Manuskripte fanden. Ohne deren Unterstützung wäre es sicher nicht möglich gewesen die Arbeit in ihrer heutigen Form zu publizieren. Ein herzliches Dankeschön geht auch an die Studenten, die im Rahmen von Studien- und Diplomarbeiten an den Aufgabenstellungen mitgearbeitet haben.

Nicht vergessen möchte ich meine Kollegen Dipl.-Ing. Werner Sörgel, M.Sc. Jung Hyo Kim und Dr.-Ing. Christian Fischer, die zum angenehmen Arbeitsklima im Büro 3.28 beigetragen haben und mit denen ich viele anregende Diskussionen führte. Auch den anderen Kollegen, den Sekretärinnen, den Mitarbeitern in der Technik und unserer Werkstatt bin ich zu Dank verpflichtet, denn durch die freundschaftliche Atmosphäre wird meine Zeit am IHE stets in angenehmer Erinnerung bleiben. Es freut mich, dass ich bei meiner Arbeit am IHE nicht nur von Kollegen, sondern auch von Freunden sprechen kann.

Schließlich will ich es nicht versäumen, meine Eltern und Schwester für ihre jahrelange Unterstützung in meinen Dank miteinzubeziehen.

Karlsruhe, im Juli 2004

Marwan Younis

Contents

Acronyms and Symbols	v
1 Introduction	1
1.1 Imaging Radar in Remote Sensing	1
1.2 State-of-the-Art and Task Formulation	4
1.3 Objectives and Scope of the Work	8
2 Principles of Digital Beam-Forming Radar	11
2.1 Digital Beam-Forming System Concept	11
2.2 Formulation of the Imaging Geometry	14
2.3 The Radar Equation for Extended Targets	15
2.3.1 Noise Contributions	16
2.4 Analytical Raw Data Signal Model	18
2.5 Radar Image Focusing	19
2.6 Range Compression	19
2.6.1 Similar Chirps (Auto-Correlation)	21
2.6.2 Different Chirps (Cross-Correlation)	23
3 Synthetic Aperture Radar with Multiple Receivers	27
3.1 System and Performance Parameters	28
3.1.1 Antenna Dimensions	29
3.1.2 Maximum Length of Receive Subarray	32
3.1.3 Cross-Range Sampling Distance	34
3.1.4 Minimum Pulse Repetition Frequency	37
3.1.5 Data Rate	38
3.1.6 Resolution	40
3.1.7 Azimuth (Along-Track) Coverage	40
3.2 Summary on the Performance Parameters	41

3.3	Fundamental Constraints on the System Performance	42
3.3.1	Signal-to-Noise Ratio of Processed Image	43
3.3.2	Noise Equivalent Sigma Zero	45
3.3.3	Trade-off between Resolution and Swath Width	45
3.4	Pulse Coded Chirp Waveforms in Imaging Radar	48
3.4.1	Principle of Operation	49
3.4.2	Quality Criterion for the Comparison of Correlation Functions	51
3.5	Performance of an Example System	53
4	Processing of DBF SAR Data and Verification	55
4.1	SAR Signal Model	56
4.2	Algorithm for Azimuth Signal Compression	57
4.2.1	Bi-static to Mono-static Data Mapping	58
4.2.2	Phase Correction in the Spatial-Frequency Domain	61
4.2.3	Uniform Cross-Range Sampling	64
4.2.4	Concatenation	67
4.3	Image Reconstruction	72
4.4	Simulator for Digital Beam-Forming SAR	73
4.5	Verification	77
4.5.1	Point Spread Function	77
4.5.2	Comparison to Stripmap SAR	79
4.5.3	Pulse Coded Chirp Waveform SAR	81
5	Multi-Transmit/Receive Real Aperture Radar	83
5.1	Basic Geometry	84
5.2	Angular Compression	86
5.3	The Near Field Correction	89
5.3.1	Summary on Near Field Corrections	94
5.4	General Condition for the Occurrence of Angular Ambiguities	95
5.4.1	Azimuth Ambiguities	98
5.4.2	Application of Ambiguity Condition	101
5.5	Multi-Tx/Rx Radar with Pulse Coded Chirp Waveforms	103
5.6	Special Case of Linear Uniformly Spaced Arrays	103
5.6.1	Azimuth Compressed Signal	104
5.6.2	Azimuth Ambiguities	107

5.7	Simulator for Multi-Transmit/Receive Radar	111
5.8	Verification	113
5.8.1	Transmit/Receive Resolution	113
5.8.2	Transmit/Receive Ambiguities	115
5.8.3	Near Field Correction	117
5.8.4	Pulse Coded Chirp Waveforms	118
6	Digital Beam-Forming Radar Demonstrator	123
6.1	The Hardware System Configuration	124
6.2	The SIREV Geometry	125
6.3	The Active Antenna and Control Hardware	126
6.3.1	Modular Concept	127
6.3.2	Transmitting Subsystem	128
6.3.3	Receiving Subsystem	128
6.3.4	The Control and Power Unit	130
6.3.5	Central RF Switch	132
6.4	Integration into the Helicopter	133
6.5	Flight Campaigns and Image Data Analysis	133
6.6	Conclusion and Further Possible Applications	136
7	Conclusions	139
	Bibliography	143
A	Correlation of Chirp Waveforms	157
A.1	General Formulation	157
A.2	Cross-Correlation	159
A.3	Auto-Correlation	160
B	Relevant Orbital Geometry and Mechanics	163
B.1	Spacecraft Velocity for Circular Orbits	163
B.2	Slant-Range Distance for Curved Earth	163
C	Spatial Fourier Transform of Spherical Phase SAR Signals	165
C.1	Asymptotic Evaluation of Integrals	165
C.2	Determining the Slow Varying Term	168

Acronyms and Symbols

In this work identical notation for real and complex quantities is used.

List of Constants

c_0	speed of light $2.997\,925 \times 10^8$ m/s in vacuum
k	Boltzmann's constant 1.38×10^{-23} J/K
g_s	earth's surface gravity 9.81 m/s ²
R_{earth}	local earth radius (GEM6) $6\,378\,144$ m
T_0	norm (noise) temperature 290 K
ε_0	permittivity 8.854×10^{-12} AsV ⁻¹ m ⁻¹ of vacuum
μ_0	permeability $4\pi \times 10^{-7}$ VsA ⁻¹ m ⁻¹ of vacuum

Mathematical Notations and Symbols

j	imaginary unit $j = \sqrt{-1}$
\mathbf{A}^*	complex-conjugate of (scalar or vector) quantity
$ \mathbf{A} $	absolute value of scalar, magnitude of complex quantity, length of vector quantity
$\angle a$	angle (phase) of complex quantity a
(x, y, z)	Cartesian coordinates
(r, ϑ, ψ)	spherical coordinates
$\mathcal{F}_{(t)}\{\dots\}$	Fourier transform with respect to t
$\mathcal{F}_{(f)}^{-1}\{\dots\}$	inverse Fourier transform with respect to f
\sim	proportional to
\mathbb{Z}	set of integer numbers

Acronyms

Italic letters indicate that the acronym is also used as a variable.

1D	One-Dimensional
2D	Two-Dimensional
3D	Three-Dimensional
ADC	Analog-to-Digital Converter
BB	base-band
DBF	Digital Beam-Forming
DFT	Discrete Fourier Transform
FFT	Fast Fourier Transform
<i>GCD</i>	Greatest Common Divisor
HPBW	Half Power Beam Width
IFFT	Inverse Fast Fourier Transform
<i>IRAR</i>	Integrated Range Ambiguity Ratio
<i>LCM</i>	Least Common Multiple
MTI	moving-target indication
<i>NESZ</i>	Noise Equivalent Sigma Zero
<i>NF</i>	Noise Figure
<i>PRF</i>	Pulse Repetition Frequency
<i>PRI</i>	Pulse Repetition Interval
PSF	Point Spread Function
PSR	Point Scatterer Response
Radar	RAdio Detection And Ranging
<i>RAR</i>	Range Ambiguity Ratio
RCS	Radar Cross Section
RF	Radio Frequency
Rx	Receive
SAR	Synthetic Aperture Radar
SNIR	Signal-to-Noise-plus-Interference Ratio

SNR	Signal-to-Noise Ratio
STAP	Space-Time Adaptive Processing
T/R	Transmit/Receive (module)
Tx	Transmit

Lower Case Letters

$a_{az} = l_{rs}/l_{ts}$	ratio of receive to transmit antenna length
$e_{NF}(\dots)$	near field influence term
$f = \omega/2\pi$	(temporal) frequency variable
f_0	center (carrier) frequency
$f_{\text{frame,image}}$	frame (or image) rate
f_s	start frequency of chirp waveform
$f(\mathbf{x}) = \sigma_o(\mathbf{x})e^{-j\phi(\mathbf{x})}$	image (object) function
$f_{ac}(\dots)$	azimuth compressed signal
$f_{rc}(\dots)$	range compressed signal
h	antenna height
$h_t(t)$	transmitted (chirp) signal in the time domain
$k = 2\pi/\lambda$	wavenumber
k_u	cross-range spatial-frequency variable
k_e	chirp rate
l	antenna length
m_a	mass of spacecraft (satellite)
n_B	number of bits per I (or Q) sample
p	number of orthogonal signals
$s(\mathbf{x}_{ti}, \mathbf{x}_{rj}, \mathbf{x}_n, t)$	received raw signal at \mathbf{x}_{rj} due to a unit point scatterer at \mathbf{x}_n and a transmitter at \mathbf{x}_{ti}
t	time variable (fast time)
u	synthetic aperture domain (slow time)
$u(\mathbf{x}_{ti}, \mathbf{x}_{rj}, t)$	raw unfocused received signal at \mathbf{x}_{rj} when the transmitter is located at \mathbf{x}_{ti}
u_s	stationary (saddle) point
v_n	relative position of receive subarray n

$w(u)$	fast varying term used in the method of stationary phase
x	range domain
$\mathbf{x} = x\hat{\mathbf{e}}_x + y\hat{\mathbf{e}}_y + z\hat{\mathbf{e}}_z$	general Cartesian position vector
y	cross-range domain

Capital Letters

A	antenna area of element, subarray or total array
$A_{\text{bi}} = A_{\text{rx}} + A_{\text{ts}}$	total area of bi-static antenna
B_w	bandwidth
B_N	equivalent noise bandwidth of receiver
$C(\psi, \vartheta)$	antenna radiation pattern
D_R	data rate
G	antenna gain
H_{orbit}	orbit height above ground
$H_t(f)$	transmitted (chirp) signal in the frequency domain
K_{ac}	exponent of azimuth compression kernel
L	synthetic aperture length
L_{feed}	losses of feed network
M	total number of transmit subarrays
N	total number of receive subarrays
$N_{\text{pulse,proc}}$	number of pulse (or processing) samples
P_t	peak transmitted power
$R(\tau)$	temporal correlation function
$R_n(\dots)$	Taylor series remainder term of order n
$R_{\text{near,far}}$	near (far) slant-range to the imaged area
R_{orbit}	orbit radius
$R_{\text{Rx,Tx}}$	distance of receive (transmit) subarray to scatterer
R_s	slant-range
T_p	duration of chirp signal
$T_{\text{ant,sys}}$	antenna (or system) equivalent noise temperature
T_{radar}	physical temperature of radar

V	velocity of radar platform
W	cross-range extent of imaged area
$W(u)$	slow varying term used in the method of stationary phase
X_0	ground-range (swath width) of imaged area
X_c	(ground) range to center of imaged area
Y_0	cross-range extent of imaged area
Y_c	cross-range center of imaged area
Z_c	platform height above (flat) ground

Greek Symbols

α	scaling parameter giving the position of the equivalent mono-static antenna
γ	safety factor related to angular position of ambiguity
δx	ground-range resolution
δy	cross-range (azimuth) resolution
Δr	range approximation error
Δu	sample spacing in synthetic aperture domain
$\Delta x, \Delta y, \Delta z$	subarray spacing in x -, y -, and z -direction, respectively
ϑ_0	focused elevation angle
$\vartheta_{\text{amb},\nu}$	elevation angle of ν -order ambiguity
Θ	elevation half power beam width (HPBW)
λ	wavelength
ν	order of ambiguity
σ_o	radar cross section normalized to the area
τ	time shift
τ_n	time delay of target n
ψ_0	focused azimuth angle
$\psi_{\text{amb},\nu}$	azimuth angle of ν -order ambiguity
Ψ	azimuth half power beam width (HPBW)
Ω_{k_u}	spatial frequency support band

Superscripts and Subscripts

\sim	(tilde) estimation of the quantity
'	(prime) indicates a transformed quantity
dB	indicates that quantity is in decibels (dB)
ac	azimuth compressed
av	denotes an average quantity
az	denotes azimuth
b	denotes a bi-static signal
d1	down-chirp occupying frequency band 1
el	denotes elevation
m	denotes a mono-static signal
n	scatterer n
rc	range compressed
r	relates quantity to receiver or receive antenna
r_j	relates quantity to receive subarray j
rs	relates quantity to single receive subarray
rx	relates quantity to total receive array
strip	relates quantity to stripmap SAR
t	relates quantity to transmitter or transmit antenna
t_i	relates quantity to transmit subarray i
ts	relates quantity to single transmit subarray
tx	relates quantity to total transmit array
u1	up-chirp occupying frequency band 1

1 Introduction

The term RADAR stands for **RA**dio **D**etection **A**nd **R**anging, this acronym can immediately be related to the main objective of classical radar techniques, which is to detect objects and associate them with a certain direction and range. The basic principle behind microwave radar operation is to transmit known electromagnetic signals and use the received echo to characterize the area illuminated by the electromagnetic waves. In contrast to radiometric and optical techniques, microwave radar is an active technique which provides its own source of illumination. This offers a great flexibility and allows operation independent of day and night time. If in addition the radar is operated at wavelengths greater than ≈ 1 cm the resulting electromagnetic waves will penetrate through clouds, fog and even moderate rain with negligible attenuation and scattering. This results in weather independent operation of such radar systems.

1.1 Imaging Radar in Remote Sensing

The very first radio experiment was conducted by HERTZ who, in 1886, demonstrated the reflection of electromagnetic waves by metallic and dielectric objects. The first demonstration of radar was in 1904 by HÜLSMEYER who used a *Telemobiloscope* to detect ships on the Rhein river in Köln and registered his patent in the same year. The next person who recognized the importance of the radar effect was MARCONI who in 1922 prophesied radar in a fiery speech before the *Institute of Radio Engineers* in London. Nevertheless, it was nearly 40 years after the experiments of Hertz that the importance of radar became increasingly recognized. This was through the experiments of BREIT and TUVE in 1926 to measure the height of the ionosphere after which research work on radar became heavily promoted in many countries.

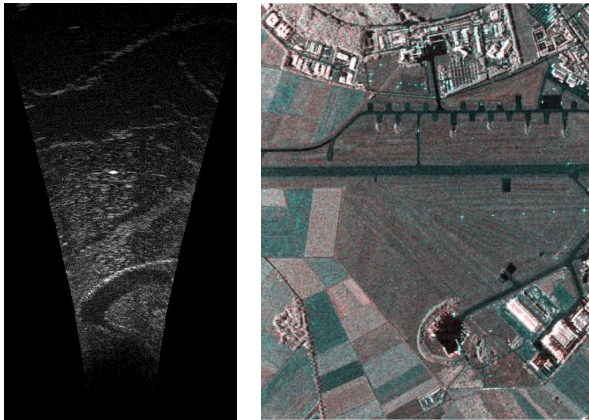
During the first decades the capabilities of radar systems were confined to the detection of *man-made* targets such as ships or airplanes. The resolution in range direction was given by the pulse duration, while the angular resolution was determined by the aperture of the radar's antenna. A good angular resolution was achieved through a narrow antenna beam and consequently a large aperture. This in conjunction with the space requirement for the equipment forced fixed ground installations for most radar systems.

Since then, the radar technology and associated signal processing has undergone rapid development, mainly pushed by the development in microwave components, electronic instruments and digital computers. It was the introduction of modulated pulses on transmit and the complementary pulse compression on receive, that allowed simultaneous long pulses and high range resolution. Thereby, the modulation determined the bandwidth and range resolution while the pulse length set the energy content and the signal-to-noise ratio at the receiver [88]. The angular resolution was then still limited by the *physical* size of the antenna. Furthermore a constant angular resolution means a reduced spatial resolution for increased range distance.

It was in the year 1954 and the patent of CARL WILEY [113] that the *synthetic aperture* was introduced for moving radar platforms to allow an improved lateral resolution in the direction of movement (also known as azimuth). The principle of synthetic aperture radar (SAR) relies on the coherent addition of recorded echos at successive positions during the movement of the radar. It turns out, that the azimuth resolution of a synthetic aperture radar depends on the distance during which a point in the imaged area is visible to the radar. This length is known as the synthetic aperture length and is proportional to the half power beam width of the radiation pattern associated with the radar's antenna. Increasing the synthetic aperture length gives a better azimuth resolution, and moreover resolution is independent of the range. But most importantly, in contrast to real aperture radar, a reduced antenna aperture gives a larger synthetic aperture and thus a better azimuth resolution.

The breakthrough in digital signal processing techniques in the eighties triggered an increased use of *imaging radar* for remote sensing applications. A radar image represents a spatial distribution of microwave reflectivity sufficient to characterize the object (e.g. terrain) illuminated by the radar [71]. The prerequisite for an imaging radar is that the resolution cell size is less than

the dimensions of the object to be imaged. The ratio of object dimensions to resolution cell size is crucial for the object identification and thus constitutes an important image quality parameter. However, the quality of a radar image should be judged by how faithfully it represents spatial reflectivities, rather than its similarity to an optical image. Imaging methods can be characterized into two major categories according to the process employed: in-place imaging (referred to as *real aperture radar* in this work), and motion imaging (represented through *synthetic aperture radar*). In the former method the object and observer are in a fixed attitude relative to each other; the resultant image is derived from and is uniquely associated with a particular object orientation. In the later method the imaging process requires a relative motion between the object and the imaging system. To illustrate the type of images obtained by each method, Fig. 1.1 shows an example image for each category obtained by different airborne radar sensors.



(a) “Lech”-River

(b) DLR/Oberpfaffenhofen

Figure 1.1: Example images obtained by real (a), and synthetic (b) aperture radars.

The last two decades witnessed and increased interest of the scientific, public, military and commercial sectors in radar remote sensing. The applications of real and synthetic aperture imaging radar span a wide range which include

agriculture, forestry, oceanography, land use, cartography, geology, ice monitoring, risk diagnostic (flood, earthquake, ice avalanche, volcano eruption), detection of ocean pollution, law enforcement, security, navigation, and anti personal mine detection. Although these application utilize imaging radar, the user (customer) requires information rather than images. The need for the development of high level operational information products with reliability and quality control is a key element for the future of radar remote sensing [75].

1.2 State-of-the-Art and Task Formulation

A conventional synthetic aperture radar (SAR) operates in the *stripmap* mode [33], as illustrated in Fig. 1.2. During its movement, the SAR images a strip of ground that has potentially unlimited extent in the direction of motion (referred to as the *azimuth* direction), but is limited in the orthogonal *range* direction. The ground-range extent of the imaged area is known as the *swath width*.

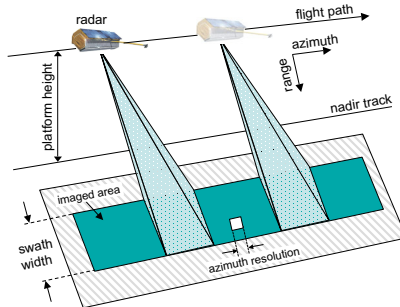


Figure 1.2: Synthetic aperture radar (SAR) operating in stripmap mode (also referred to as “conventional” SAR)

One of the major deficiency of state-of-the-art SAR systems is that their dimensioning is subject to two contradicting requirements, which are azimuth resolution and swath width [22]. Both quantities (illustrated in Fig. 1.2) represent fundamental constraints of these SAR systems [41]. Improving either one of these parameters (higher resolution or increased swath width) will lead to a degradation of the other or otherwise result in a sever impairment in the system performance. What makes the situation even worse is that for conventional

SAR these parameters are fixed through the hardware of the system (antenna size) and cannot be altered during the operation. This inflexibility has led to the development of current SAR systems such as ENVISAT/ASAR, PAMIR and TERRASAR-X [36, 84, 129] characterized through multiple operation modes [10, 20, 23, 62], which are basically specified by the (time dependent) shape of the radiation pattern of the phased array antenna. Several basic modes can be distinguished.

Stripmap SAR: Up to a few years ago the majority of the SAR systems would be operated in the stripmap mode. The radiation pattern of a stripmap SAR is time invariant and illuminates a spot on the ground which moves with the velocity of the radar. The resulting image is a continuous strip of medium resolution.

ScanSAR mode: The purpose of this operation mode, shown in Fig. 1.3(a), is to increase the swath width as compared to stripmap SAR. The phased array repeatedly illuminates subsequent sub-swaths in a cyclic manner. Each sub-swath is only illuminated during a small part of the synthetic aperture length, which inevitably results in a reduced azimuth resolution of the imaged area.

Spotlight mode: In this mode the azimuth resolution is increased with respect to stripmap SAR. This is achieved by steering the main antenna beam in azimuth direction such that the area of interest is illuminated for a long time (see Fig. 1.3(b)). This way the synthetic aperture length is artificially extended compared to the stripmap mode. However, the disadvantage is that it is no longer possible to image a continuous strip on the ground.

It is evident that the multi-operation modes have a number of disadvantages [31, 127]: the different operation modes are exclusive of each other, thus offering only a limited flexibility, since they still trade resolution against coverage; the required instrumentation introduces complex operational problems at mission planning level; the performances in the different modes are often not comparable leading to problems of inconsistent data sets. In addition these operation modes can only be realized by the use of so called transmit/receive modules, which are used to steer the main beam of the phased array antennas. Although

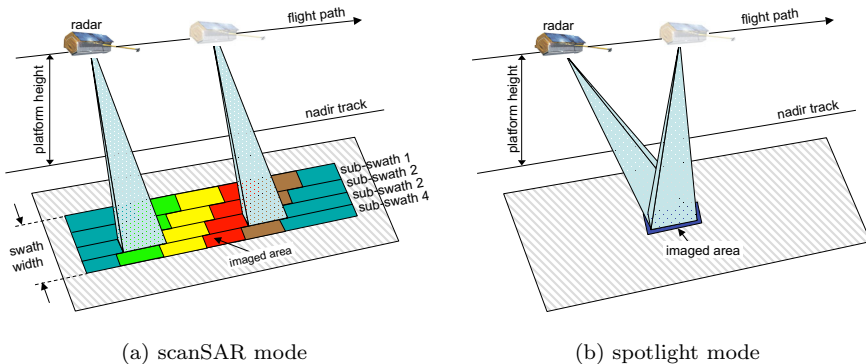


Figure 1.3: Synthetic aperture radar operation modes

digitally controlled, these T/R modules are based on analog RF technology for phase and amplitude setting [46, 66, 81]. It is this analog RF “thinking” still common in the radar community, which dictates the development of the current generation of radar systems.

Several alternative methods have been proposed for a SAR with simultaneous high resolution and wide swath. Most reported research into wide swath SAR has been directed toward sophisticated antenna systems to suppress range-ambiguous returns through the antenna pattern [23, 49, 107]. Zero steering of an 2×2 array is suggested in [17, 19] to null out range ambiguities. In [48, 101] multiple elevation receive apertures are used in combination with dedicated time varying phase shift in order to track the pulse in elevation¹. This approach is based on beam-steering in elevation and offers the possibility to increase the swath width without sacrificing azimuth resolution. Although quite promising, the approach requires a time dependent and frequency varying phase shift for chirped signals, which although realized digitally, i.e., after A/D conversion may be difficult to implement.

Progressive trends in radar originate from moving-target indication (MTI),

¹Although both [101] and [19] use multiple subarrays in elevation, the philosophy is rather different. In [101] the radar pulse is tracked while it traverses the imaged area. In [19] a null of the array factor is positioned at the presumed angle of the unwanted return.

a basic feature of ground-based surveillance radars, involving the detection of moving targets. Detection performance and estimation accuracy can be improved considerably by the use of pulsed signals (temporal domain) and an array of antennas (spatial domain) while adaptively adjusting the two-dimensional space-time filter response to maximize the signal-to-noise-plus-interference ratio (SNIR). This technique is known as space-time adaptive processing (STAP) [57, 70], which was first introduced to the airborne radar community by BRENNAN AND REED in 1973 [14]. The realization of STAP based radars in airborne platforms and spaceborne satellites was only possible through the advancement in digital signal processors. However, STAP is engaged with the detection of moving targets against ground clutter returns and jamming, while imaging radar inherently makes no provision for moving target detection. Depending on the target motion the corresponding image of the target may appear displaced or blurred [80]. Imaging with simultaneous detection of moving targets has been proposed in [28, 92] for conventional SAR, but can —more efficiently— be achieved by multi-channel SAR [34, 35], which basically means utilizing digital beam-forming.

Imaging radar applications include a wide range of sometimes conflicting requirements on coverage, spatial resolution, revisit and access times. For example, security applications typically require a very high resolution image of a small area to be available within a very short time in the order of hours [13]; on the other hand agricultural applications require a (relative) low resolution image of a large area within a periodically repeated cycle [100]. To meet these requirements, multi-purpose systems with adjustable resolution and coverage are crucial. The “ideal” remote sensing system would use a fixed hardware which can be reconfigured by software depending on the demand [112, 122, 127]. The work presented herein, is regarded as a step in the direction of reconfigurable radar sensors.

What we have today are highly sophisticated imaging radar systems, based mainly on analog RF technology. Two strategies are foreseeable to meet the future demands on remote sensing imaging radar [30]: either improve the current analog hardware systems, or move towards digital systems. The former will lead to even more complex systems operating at the critical limits of feasibility. The latter leads to systems different from current state of the art, which requires progressive thinking and establishing the basic system performance

criteria [123]. A glance towards the development in the closely related field of mobile communications, reveals a clear trend towards digital techniques. Procedures unforeseeable only a few years ago, currently exist and are operational at costs, tolerable for any private user. It is foreseeable that future 3rd generation mobile phone terminals will have processing capabilities of several GFLOPS (giga floating-point operations per second). For spaceborne SAR, the memory and processing rate requirement for real-time on-board processing are in the order of 1 – 15 Gbyte and 10 – 100 GFLOPS, respectively [32, 55]. The transfer of the recent advancement of high speed, high performance, digital signal processors to the radar technology is possible and mandatory to cope with the increasing demand on imaging radar.

The current work opens the way toward the second of the two approaches.

1.3 Objectives and Scope of the Work

The motivation for this work immediately results from the before mentioned deficiencies of state-of-the-art imaging radar systems and their difficulty to cope with the current requirements. This handicap of analog technology is overcome by suggesting an imaging radar system utilizing digital beam-forming (DBF). The idea of a digital radar is not new to the remote sensing community and can be found in open literature [9, 95, 97, 105, 127], and digital beam-forming is well known and already implemented in communication systems [106, 3, 60]. However the work presented herein establishes a novel foundation for the principal performance parameters of a digital beam-forming radar systems. It is shown that the step towards a digital radar opens the possibility for a totally new dimension in system performance.

The approach followed in this work is unique in the sense that it provides general design parameters and systems configurations for radar with digital beam-forming and relates these to critical system parameters. Within the scope of the work basic expressions relating the various system and performance parameters to each other are derived. When possible these expressions should be analytically solvable, such that the system designer can obtain an easy overview of the system complexity and associated performance. The results are analyzed and discussed on the basis of performance graphs and verified

by simulations. In addition dedicated processing algorithms for digital beam-forming radar will be derived, which can be embedded in existing state-of-the-art image reconstruction tools.

The work is organized as follows: Starting point is the system concept for a radar with digital beam-forming using multiple transmit and receive antennas. This is detailed in chapter 2 including possible hardware implementations. The geometry is stated and used to derive the radar equation and the signal model for a DBF radar based on the specialties of this system. Further, the general formulation of the radar focusing (imaging) algorithm is given and used to derive analytic expressions for the range compressed chirp signals. The treatment of range compression includes the derivation of rigorous expressions for the correlation function between different types of chirp waveforms. It is understood that this chapter sets the principles and develops the basic expressions for the digital beam-forming radar used in the later chapters.

Chapter 3 deals with digital beam-forming for *synthetic* aperture radar. Basic expression for the performance parameters and design restrictions are developed in this chapter. The performance is compared to a reference conventional stripmap SAR system. Later the fundamental constraints are redefined for the digital beam-forming SAR. An aspect for improving the system performance is waveform diversity; the chapter derives the quality criteria to show how this can be used to increase the swath width of a SAR system utilizing pulse coded chirp waveforms. In chapter 3 for the first time the interrelation between performance and system parameters for a DBF SAR is formulated using analytic expressions. The chapter concludes by an exemplary comparison of a potential DBF SAR to an in-orbit SAR system.

Determining the potential performance of a DBF SAR system is, however not sufficient. A processing procedure is needed which transforms the raw input data into the output image. Chapter 4 treats the DBF SAR image reconstruction. After pointing out the main differences to conventional SAR signals, a novel azimuth compression algorithm is developed which can be interlaced with existing well-established SAR processing tools. The idea behind this approach is to pre-process the data in such a way, that conventional processing can also be used on the data. To the author's knowledge the implementation is unique in the sense that it embeds the pre-processing within a modified fast Fourier transform (FFT) kernel. Within the chapter a simulator for DBF SAR is sug-

gested and implemented in MATLAB[®]. The performance of the algorithm is verified on simulated SAR signals, in addition the simulator is used to assess the results of chapter 3 and to compare them to the performance of a conventional SAR.

Synthetic aperture radar is not the only possible application for digital beam-forming. An interesting imaging radar treated in chapter 5 is known as *real* aperture radar and typically consists of a relative small number of transmit and receive antennas. The work in this chapter, for the first time, gives a comprehensive mathematical treatment for the angular compression using multiple transmit/receive antennas. This includes analyzing near field effects, angular ambiguities (ghost images) and the non-uniform antenna placement. In addition, the chapter also shows how pulse coded chirps can be successfully implemented in a real aperture radar to reduce the measurement time. Further, a multi-transmit/receive simulation tool is implemented and used to verify the mathematical expressions derived throughout the chapter.

Chapter 6 deals with an experimental radar system implemented to demonstrate the functionality and performance of digital beam-forming. The forward radar system known as **S**ector **I**maging **R**adar for **E**nhanced **V**ision (SIREV) is the first of its type implementing digital beam-forming. It consists of an active 56-antenna receive array and one transmitter all mounted on a helicopter. The emphasis of the chapter is on the RF and control hardware implementation of the active array. The processed images from measured data of two flight campaigns carried out with the SIREV system are presented. The chapter concludes by stating further possible applications of digital beam-forming radar.

Chapter 7 completes the work with a conclusion and a view on the benefits of digital beam-forming for future radar imaging systems.

2 Principles of Digital Beam-Forming Radar

This chapter explains the main system blocks and the operation of a digital beam-forming (DBF) radar. Starting from the system configuration described in section 2.1 the geometry of the DBF configuration is stated in section 2.2. In radar applications the received signals are contaminated by noise, this is described by the radar equation which is derived for the distributed scatterer bi-static configuration in section 2.3. Section 2.4 derives a raw data signal model, which is used in section 2.5 to give a general expression for focusing radar signals. The signal model and focusing expression are the base used later in chapters 4 and 5 for the azimuth (angular) compression. A common processing step both for synthetic and real aperture radar is the range compression, which is derived and analyzed in section 2.6, this includes an analysis of the correlation between chirp waveforms, which is used in later chapters to analyze waveform diversity radar.

2.1 Digital Beam-Forming System Concept

Figure 2.1 shows the system concept for digital beam-forming on-receive-only. The radar system is split up into a transmit (Tx) and a receive (Rx) subsystem respectively. In principle the two subsystems can be mounted on a single carrier or placed on separate platforms [68, 73, 58], however, in the context of this work one common platform will be assumed for both subsystems. Thus, the DBF configuration is a multi-static configuration consisting of several receive and transmit subarrays placed at arbitrary positions on a common carrier. In the general case an unequal number of transmitters and receivers is used and the spacing between the subarrays is nonuniform.

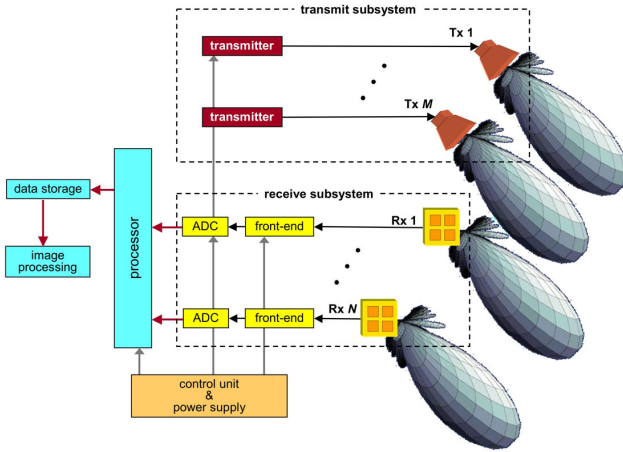


Figure 2.1: Digital beam-forming system concept.

Each of the M transmit antennas is fed by a high power amplifier. Each transmit antenna beam illuminates the complete area to be imaged. On receive the signals picked up from each of the N receive subarrays are amplified, down converted (front-end), digitized (ADC) and stored in mass memory for later image processing (see Fig. 2.1). The footprint of all receive subarrays are identical, thus each receive antenna covers the same spatial segment also referred to as the *imaged area*.

The digital beam-forming radar operates by coherently recording the echoed signals from each transmitted pulse. The echo of any Tx transmission is detected and stored by all N receivers simultaneously. The M transmitters are operated successively at subsequent time instances¹ and the data (temporal sequence) is collected for each pulse. Digital beam-forming is performed solely on the analog-to-digital converted receive subarray outputs, which means that there is no need for analog phase and amplitude control through transmit/receive (T/R) modules.

¹This assumption is true for synthetic aperture radar, for real aperture radar it is shown in section 5.5 that pulse coded chirp waveforms can be used to simultaneously operate two or more transmitters.

The two subsystems enable separate performance optimization for each of the transmit and receive subsystem. The complexity of the transmit subsystem is kept to a minimum, it consists of simple and robust hardware. A high efficiency high power amplifier such as travelling wave tubes (TWT) with 65 % efficiencies [12] can be used. The transmit antennas are simple lossless dishes or horns. On receive the analog RF components are minimized. Low noise amplifiers and microwave monolithic integrated circuits (MMIC) can be integrated into the receive subarrays [128].

The advantages of DBF radar configuration are:

- the system concept is in favor of higher efficiency and lower power consumption;
- the analog RF components of the system are reduced to a minimum (no T/R modules are needed);
- the requirements on the control systems and power supply units are relaxed due to the absence of the T/R modules;
- the system is reconfigurable by software and adaptable to different requirements [112];
- the multi-operating modes using analog beam steering disappear (see section 3.2);
- resolution and coverage are widely independent of each other (as detailed in section 3.1.6); and
- digital calibration is possible, since the phase and amplitude signal weighting is implemented in the digital domain, thus the complex calibration of the T/R modules becomes dispensable.

These advantages are paid for by an increased data rate (cf. section 3.1.5) and higher processing requirement (cf. section 4.4) as compared to current systems. In addition special care is needed when considering the power budget of the individual channels due to the reduced gain of the individual subarrays (cf. section 3.1).

2.2 Formulation of the Imaging Geometry

The general form for the imaging geometry applicable both to real and synthetic aperture radar is shown in Fig. 2.2. All M transmitters and N receivers are mounted on the radar platform, which moves with the velocity V along in the direction specified by the velocity vector. The position of transmitter $\text{Tx } i$ and receiver $\text{Rx } j$ with respect to the coordinate center is given by \mathbf{x}_{t_i} and \mathbf{x}_{r_j} , respectively. The radar images an area on the ground centered at (X_c, Y_c) . The position of point scatterer n within the imaged area is given by \mathbf{x}_n . The imaged surface consists of a distribution of scatterers which is described by the 2D complex image (reflectivity) function $f(\mathbf{x}) = f(x, y) = \sigma_o(x, y)e^{-j\phi(x, y)}$ (assuming all scatterers to be bounded to the xy -plane). The distances $R_{\text{Tx}i}$ and $R_{\text{Rx}j}$ are, respectively, the transmitter i and receiver j path lengths to the scatterer.

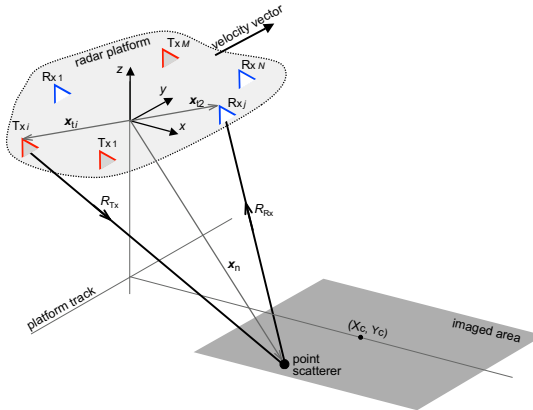


Figure 2.2: General geometric configuration of the Tx and Rx subarrays.

The round-trip path length $R_{\text{Tx}} + R_{\text{Rx}}$ is included in the phase of the received signal. Thus, varying the position of either the transmitter \mathbf{x}_t or the receiver \mathbf{x}_r will result in a different value for the phase of the received signal. Basically it is this path dependent phase shift which is used—in addition to range compression—for image formation. In the case of a *real* aperture radar the phase variation is achieved through the different (but fixed) positions of the transmit and receive antennas. For a *synthetic* aperture radar the radar

platform movement is used to vary the distances R_{T_x} and R_{R_x} which also yields a phase variation.

The SAR principle is commonly based on a side-looking geometry. This means that the SAR antenna is looking perpendicular to the flight direction and illuminates a swath on the ground located to either the left or right side of the flight path. Squinted SAR imaging is also possible using appropriate processing algorithms [76, 24] of multi-operation mode SAR systems. In this case the antenna beam is steered away from the direction perpendicular to the flight path by the *squint angle*. For large squint angles (e.g., $> 60^\circ$) the processing algorithm needs to accommodate a very large range cell migration, which results from the fact that the synthetic aperture becomes oriented perpendicular to the imaged area. For a forward-looking SAR, i.e. a squint angle of 90° , the lines of equal Doppler become parallel to the flight path, or stated differently, the synthetic aperture length reduces to the (physical) *real antenna* length. This basically means that the platform movement can no longer be used for resolution enhancement and the velocity might as well be set to $V = 0$. It can be concluded, that although synthetic aperture radar systems have proved as an indispensable tool in many remote sensing applications, they suffer from a system inherent visualization gap in the forward and downward directions of the flight path. The solution is to utilize the type of radar appropriate to the need, which is a synthetic aperture radar (chapter 3 and 4) for an imaged area to either side of the moving ($V \neq 0$) radar, and a real aperture radar (chapter 5) otherwise.

The above formulation of the imaging geometry is now used to derive the bi-static radar equation for distributed scatters (section 2.3) and the signal model (section 2.4) of the DBF configuration.

2.3 The Radar Equation for Extended Targets

The radar equation gives an expression relating the hardware, system and performance parameters to each other [33, 22, 88]. In this section a most general form of the radar equation for extended targets is stated.

In remote sensing the imaged area can be considered as an *extended scatterer*,

for which the radar cross section (RCS) is defined per unit geometrical area of the scene. The extended target radar equation serves the general purpose of expressing the influence of the antenna and receiver noise on the image quality. The quantity of interest is the received power of the signal echo from an area having an average specific RCS of $\sigma_0(\vartheta, \psi)$, which depends on the angular coordinates ϑ and ψ . All terrain elements contribute to the total received power. In terms of the signal-to-noise ratio (*SNR*) at the receiver the *mono-static* radar equation is [99, 109]:

$$SNR = \frac{P_t \lambda^2 G^2}{(4\pi)^3 k T_{\text{sys}} B_N L_{\text{feed}}} \int_{\text{area}} \frac{C^2(\vartheta, \psi) \sigma_0(\vartheta, \psi)}{r^4} dA \quad (2.1)$$

where P_t is the peak transmitted power; G is the antenna gain; r is the distance to the target point (polar coordinate); $kT_{\text{sys}}B_N$ is the total equivalent noise power at the receivers input; L_{feed} is the losses of the feed network; $C(\vartheta, \psi)$ is the antenna's radiation pattern; and the integration is over the area with differential element dA .

The radar equation is extended to the *slight* bi-static configuration typical for DBF radar by including the different transmit and receive antenna gains and radiation patterns, respectively:

$$SNR = \frac{P_t \lambda^2 G_{\text{ts}} G_{\text{rs}}}{(4\pi)^3 k T_{\text{sys}} B_N L_{\text{feed}}} \int \frac{C_{\text{ts}}(\vartheta, \psi) \sigma_0(\vartheta, \psi) C_{\text{rs}}(\vartheta, \psi)}{r^4} dA \quad (2.2)$$

where $C(\vartheta, \psi)$ and G are the radiation pattern and gain of the transmit (subscript ts) and the receive (subscript rs) antenna respectively. The distance r and the angles (ϑ, ψ) are assumed unchanged with respect to the mono-static configuration.

Throughout later chapters the radar equation will be reformulated to emphasize on its various parameters in addition the radar equation is used to establish a point of comparison between SAR systems.

2.3.1 Noise Contributions

In principle, two types of noise have to be distinguished in radar imaging. The first type, often simply summarized as “thermal noise”, is caused by the superposition of a large number of different effects, such as active component's and

antenna's noise, quantization errors in the A/D converters, refractive fluctuations, etc. This type of noise can be accounted for by an additive random noise model [99]. The second type of noise, namely speckle, is of fundamentally different nature [109]. It is caused by the interference of the different radar signals reflected within one resolution cell. In the processed images speckle noise manifests itself as a granular pattern, which systematically varies with a change in the viewing angle. Speckle can be modeled by a multiplicative random process [74].

The performance of the antenna and receiver hardware in terms of thermal noise is represented by the system noise temperature T_{sys} . This is the equivalent noise temperature of a matched termination applied at the input of the receiver that accounts for all noise contributions of the system [99]. Fig. 2.3 shows the system component contributing to T_{sys} , which are given by: the noise temperature T_{ant} as “seen” by the antenna [21, 121]; the noise added due to the losses L_{feed} of the feed network²; and the contribution of the receiver itself to the noise temperature $T_{\text{rec}} = (NF_{\text{rec}} - 1)T_o$, where NF_{rec} is the noise figure of the receiver [87, 16].

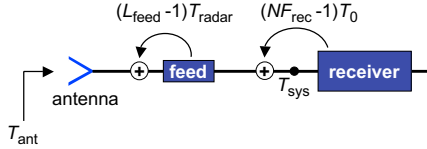


Figure 2.3: The contribution of the receiver stages to the system noise temperature.

The system noise temperature is then given by [121]:

$$T_{\text{sys}} = \frac{T_{\text{ant}}}{L_{\text{feed}}} + \left(1 - \frac{1}{L_{\text{feed}}}\right) T_{\text{radar}} + (NF_{\text{rec}} - 1)T_o \quad (2.3)$$

where T_{radar} is the “physical” temperature of the antenna and $T_o = 290$ K.

²A procedure for minimizing the noise contribution of the feed network is given in [26].

2.4 Analytical Raw Data Signal Model

Let the transmitted signal be a linear frequency modulated chirp given by

$$h_t(t) = e^{+j2\pi f_0 t + j2\pi k_e t^2} \text{rect} \left[\frac{t}{T_p} \right] \quad (2.4)$$

where the chirp duration is T_p ; while k_e is the *chirp rate*, which is related to the *chirp bandwidth* B_w by $k_e = B_w/(2T_p)$; and the first exponent gives the carrier frequency f_0 of the RF signal. The chirp is used in most radar primarily because of its ease of implementation and its Doppler tolerance.

With reference to the geometry of Fig. 2.2, the signal received by element j positioned at \mathbf{x}_{rj} due to a point scatterer of unit reflectivity ($\sigma_0 = 1$) positioned at \mathbf{x}_n and a chirp signal transmitted by subarray i positioned at \mathbf{x}_{ti} is

$$\begin{aligned} s(t, \mathbf{x}_{ti}, \mathbf{x}_{rj}, \mathbf{x}_n) &= h_t \left(t - \frac{R_{Txi} + R_{Rxj}}{c_0} \right) \\ &= e^{+j2\pi f_0 t - j \frac{2\pi}{\lambda} (R_{Txi} + R_{Rxj})} \cdot e^{+j2\pi k_e \left(t - \frac{R_{Txi} + R_{Rxj}}{c_0} \right)^2} \\ &\quad \text{rect} \left[\frac{t - (R_{Txi} + R_{Rxj})/c_0}{T_p} \right]. \end{aligned} \quad (2.5)$$

The distances R_{Txi} and R_{Rxj} are, respectively, the transmitter i and receiver j path lengths to the scatterer. The *fast* time is denoted by t , and c_0 is the velocity of light. The first exponential term in (2.5) describes the antenna-position dependent phase modulation; it is this phase term, which carries the information on the angular position of the scatterer. The second exponential term carries the range information. The rect-function limits the received signal to the pulse duration of the chirp signal. All amplitude terms (e.g., path attenuation and antenna patterns) are irrelevant for the mathematical description and are therefore omitted.

In practice, the imaged surface consists of a continuous distribution of scatterers described by the image function $f(\mathbf{x})$. The total received signal accounting for the complex sum of surface reflectivities is obtained by weighting the

signal in (2.5) by the image function, which gives [8]

$$\begin{aligned} s(t, \mathbf{x}_{ti}, \mathbf{x}_{rj}) &= \int s(t, \mathbf{x}_{ti}, \mathbf{x}_{rj}, \mathbf{x}) f(\mathbf{x}) d\mathbf{x} \\ &= \iint h_t \left(t - \frac{R_{Tx_i} + R_{Rx_j}}{c_0} \right) f(x, y) dx dy. \end{aligned} \quad (2.6)$$

2.5 Radar Image Focusing

The aim of radar signal processing also known as *focusing* is to determine the image function $f(x, y)$. The reconstruction involves determining $f(x, y)$ based on the measured signals.

In [7] the “optimum” focusing is given to be the 2D space-variant correlation of the received signal $s(t, \mathbf{x}_{ti}, \mathbf{x}_{rj})$ with the *point scatterer response* (PSR). For the case of discrete Tx/Rx subarrays’ positions, this is

$$\tilde{f}(\tau, \mathbf{x}_n) = \sum_{i=1}^M \sum_{j=1}^N \int_0^{\infty} h^*(t - \tau, \mathbf{x}_{ti}, \mathbf{x}_{rj}, \mathbf{x}_n) s(t, \mathbf{x}_{ti}, \mathbf{x}_{rj}) dt \quad (2.7)$$

in which case $h(\dots)$, the PSR, is the time–space variant signal predicted for a point scatterer located at \mathbf{x}_n .

The above correlation requires the integration and summations to be performed for each pixel in the image which is expensive from the computational point of view. A more efficient focusing algorithm may be derived if the received data is first compressed in range and then focused in azimuth. In addition to its efficiency, this method facilitates the addition of a range- and angle-dependent correction to be applied on the data, for example to compensate the distortion due to the radiation pattern. Next, an analytic expression for the range compressed signal will be derived, which is used in chapters 4 and 5 to formulate the azimuth focusing.

2.6 Range Compression

Range compression is equivalent to a 1D correlation between the transmitted chirp and the received signal. In general this correlation is referred to as cross-

correlation³, since it is assumed that the two signals are not identical. The range compressed signal f_{rc} is given by

$$f_{\text{rc}}(\tau, \mathbf{x}_{ti}, \mathbf{x}_{rj}, \mathbf{x}_n) = \int_{-\infty}^{+\infty} h_t^*(t) s(t + \tau, \mathbf{x}_{ti}, \mathbf{x}_{rj}, \mathbf{x}_n) dt \quad (2.8)$$

here $h_t^*(t)$ is the complex conjugate of the transmitted chirp of duration T_p as given by (2.4). In contrast to the space-variant correlation in (2.7) the above correlation is independent on the spatial coordinates. The correlation is equivalent to a matched filter [79, 74]. Since the correlation in (2.8) is time invariant it can efficiently be implemented in the frequency domain using the Fast Fourier Transform (FFT) and the fact that the correlation reduces to a multiplication in the frequency domain [38, 8]

$$\mathcal{F}_{(t)} \{f_{\text{rc}}(\tau, \mathbf{x}_{ti}, \mathbf{x}_{rj}, \mathbf{x}_n)\} = \mathcal{F}_{(t)} \{h_t^*(t)\} \cdot \mathcal{F}_{(t)} \{s(t, \mathbf{x}_{ti}, \mathbf{x}_{rj}, \mathbf{x}_n)\}. \quad (2.9)$$

An elegant analytic formulation for the range compression is possible if the signals and the respective correlation functions are expressed in the time domain, which is the approach followed in this work (In [53] filtering in the frequency domain is carried out instead to obtain the correlation function). The following correlation functions are of interest:

- For range compression, the auto-correlation between identical (i.e., same chirp rate and same frequency band) chirps is used to obtain a high range resolution in conjunction with long pulses. This is treated in section 2.6.1.
- In conjunction with the treatment of chirp pulse coding (see sections 3.4, 4.5.3 and 5.5) the cross-correlation properties between different chirps is crucial for the suppression of range ambiguities. In section 2.6.2 the necessary correlation functions are derived which serve as a foundation for the later treatment.

³In [98] the cross-correlation between two time dependent signals $f(t)$ and $g(t)$ is defined as $\int_{-\infty}^{+\infty} f^*(t)g(t + \tau)dt = \int_{-\infty}^{+\infty} f^*(t - \tau)g(t)dt$.

2.6.1 Similar Chirps (Auto-Correlation)

To evaluate the correlation, only the time dependent terms in (2.5) need to be considered; inserting into (2.8) gives

$$R(\tau) = \int_{-\infty}^{+\infty} e^{-j2\pi k_e t^2} \text{rect} \left[\frac{t}{T_p} \right] e^{+j2\pi k_e (t+\tau-\tau_n)^2} \text{rect} \left[\frac{t+\tau-\tau_n}{T_p} \right] dt \quad (2.10)$$

where both the received and reference chirp signal are assumed to be down converted before performing the correlation (mathematically this is equivalent to multiplying by $e^{-j2\pi f_0 t}$). In appendix A.3 the above integral is solved and the result expressed in a closed form given by

$$R(\tau) = \frac{\sin \left(2\pi k_e (T_p |\tau - \tau_n| - (\tau - \tau_n)^2) \right)}{2\pi k_e (\tau - \tau_n)} e^{+j2\pi k_e T_p (\tau - \tau_n)} \text{rect} \left[\frac{|\tau - \tau_n|}{T_p} \right]. \quad (2.11)$$

The resulting correlation function shows similarities to the $\sin x/x$ -function. The magnitude $R(\tau)$ has a peak at $\tau = \tau_n$ (where τ_n is the round-trip time delay), which after a change of variables $\tau_n = (R_{Tx} + R_{Rx})/c_0$ is directly proportional to the total path length $R_{Tx} + R_{Rx}$. For more than one point scatterer the range compressed signal is a sum of $\sin x/x$ -functions, the magnitude at each range gate (or delay value) being proportional to the complex sum of reflectivities for all scatterers of the same total path length.

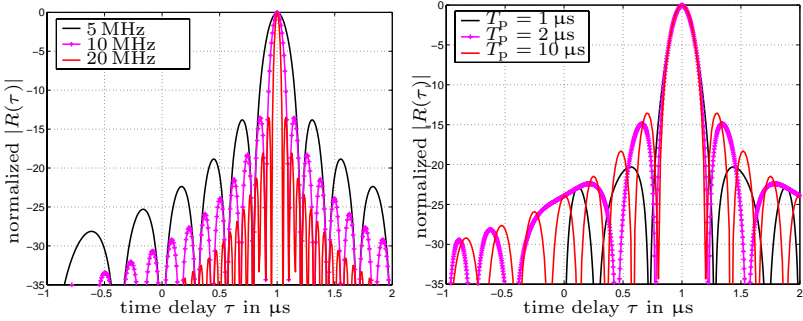
Three parameters influence the correlation function:

- The delay τ_n gives the total delay of the scattered signal; from (2.11) it is obvious that changing τ_n solemnly shifts the correlation function.
- Increasing the bandwidth B_w reduces the main lobe width of the correlation function $|R(\tau)|$, which is seen by substituting the chirp rate k_e in (2.11) by $B_w/(2T_p)$. Fig. 2.4(a) shows the effect of varying the bandwidth for a fixed chirp duration. A sharp correlation function (or equivalently a high range resolution) can *only* be achieved by increasing the chirp bandwidth.
- The chirp duration T_p has a minor influence on the shape of the normalized correlation function, as seen in Fig. 2.4(b) showing the effect of varying T_p for a fixed bandwidth. However, increasing T_p increases the

energy content of the chirp signal. Specifically, the maximum value of $|R(\tau)|$ is for $\tau \rightarrow \tau_n$, which (using l'Hospital [45]) is given by

$$\lim_{\tau \rightarrow \tau_n} |R(\tau)| = \lim_{\tau \rightarrow \tau_n} \frac{\frac{\partial}{\partial \tau} \sin(2\pi k_e(T_p|\tau - \tau_n| - (\tau - \tau_n)^2))}{\frac{\partial}{\partial \tau} 2\pi k_e|\tau - \tau_n|} = T_p. \quad (2.12)$$

Thus increasing the chirp duration will increase the signal-to-noise ratio at the receiver.



(a) fixed $T_p = 5 \mu\text{s}$; bandwidth $B_w = 5 \text{ MHz}$, 10 MHz , and 20 MHz

(b) fixed $B_w = 5 \text{ MHz}$; pulse duration $T_p = 1 \mu\text{s}$, $2 \mu\text{s}$, and $10 \mu\text{s}$

Figure 2.4: Correlation function $|R(\tau)|$ for a total path length $R_{T_x} + R_{R_x} = 300 \text{ m}$ when varying (a) the bandwidth B_w ; and (b) the pulse duration T_p .

The range compressed signal is given in (2.13) which is obtained from (2.11) after including the non-time dependent terms of (2.5)

$$f_{\text{rc}}(\tau, \mathbf{x}_t, \mathbf{x}_{rj}, \mathbf{x}_n) = e^{-j\frac{2\pi}{\lambda}(R_{T_x i} + R_{R_x j})} e^{+j2\pi k_e T_p (\tau - \tau_n)}. \frac{\sin(2\pi k_e(T_p|\tau - \tau_n| - (\tau - \tau_n)^2))}{2\pi k_e|\tau - \tau_n|} \text{rect}\left[\frac{|\tau - \tau_n|}{T_p}\right]. \quad (2.13)$$

This is understood as the result of solving the time-integral in (2.7) of the optimum focusing.

2.6.2 Different Chirps (Cross-Correlation)

In general, a chirp waveform is characterized by the start frequency f_s , the chirp rate $k_e = B_w/(2T_p)$, and the chirp duration T_p . In the following the subscripts ₁ and ₂ are added to relate the above quantities to one of two chirp waveforms. Neglecting amplitude and carrier frequency terms the chirp waveforms are

$$h_{t1}(t) = e^{+j2\pi f_{s1}t + j2\pi k_{e1}t^2} \cdot \text{rect} \left[\frac{t}{T_p} \right] \quad (2.14)$$

$$h_{t2}(t) = e^{+j2\pi f_{s2}t + j2\pi k_{e2}t^2} \cdot \text{rect} \left[\frac{t}{T_p} \right] \quad (2.15)$$

where a positive k_e corresponds to an up-chirp, i.e., the instantaneous frequency increases with time, while a negative k_e corresponds to a down-chirp.

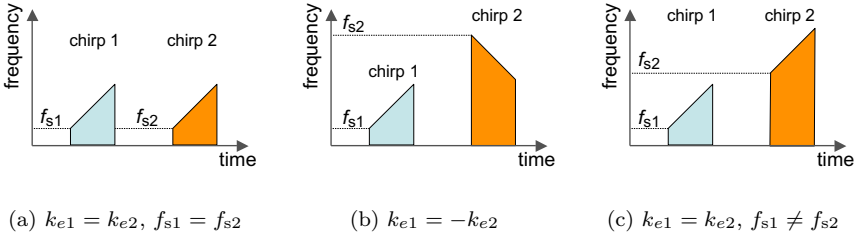


Figure 2.5: The different cases for the correlation between chirp waveforms.

In order to investigate the possibilities of processing pulse coded chirp waveforms an analytic expression for the correlation function $R(\tau)$ between the chirp waveforms is derived in appendix A. This expression is used to analyze the performance parameters of dual chirp systems. To specify the type of correlation function, the subscripts _u and _d are added to denote the type of the chirp waveform (i.e. up- or down-chirp), while the subscripts ₁ and ₂ are used to denote the occupied frequency band (depending on the start frequencies and the chirp rates). For example (with reference to the time-frequency plot in Fig. 2.5) $R_{u1u1}(\tau)$ is the correlation of two up-chirps occupying identical frequency bands (see Fig. 2.5(a)), while $R_{u1d2}(\tau)$ is the correlation of an up-chirp with a down-chirp occupying different frequency bands (see Fig. 2.5(b)) and

$R_{u1u2}(\tau)$ stands for the correlation between two up-chirps (having the same chirp rate) but occupying different frequency bands (see Fig. 2.5(c)).

Depending on the parameters of the chirp waveforms in (2.14) and (2.15), three different cases are distinguished:

1. Same chirp rate $k_{e1} = k_{e2} = k_e$ and same start frequency $f_{s1} = f_{s2} = f_s$. The time-frequency plot is shown in Fig. 2.5(a).

This is the auto-correlation function given in (2.11) for zero time delay $\tau_n = 0$, i.e.,

$$R_{uu}(\tau) = \frac{\sin(2\pi k_e \tau (T_p - |\tau|))}{2\pi k_e \tau} e^{+j2\pi(f_s + k_e T_p)\tau} \cdot \text{rect}\left[\frac{|\tau|}{T_p}\right]. \quad (2.16)$$

2. Inverse chirp rate $k_{e1} = -k_{e2}$ and arbitrary start frequencies. The time-frequency plot is shown in Fig. 2.5(b).

The correlation is derived in appendix A.1 and given by (A.9)

$$R_{u1d2}(\tau) = K(\tau, f_s, k_e) \left[C(\nu(t_2)) + jS(\nu(t_2)) - C(\nu(t_1)) - jS(\nu(t_1)) \right] \quad (2.17)$$

where the Fresnel integrals $C(\nu)$ and $S(\nu)$ are real valued functions [2], whereas $K(\tau, f_s, k_e)$ is a complex function, with an amplitude $|K(\tau, f_s, k_e)|$ that is independent of the variable τ .

3. Same chirp rate $k_{e1} = k_{e2} = k_e$ but different start frequencies $f_{s1} \neq f_{s2}$. The time-frequency plot is shown in Fig. 2.5(c).

In this case the correlation function is derived in appendix A.2 and given by (A.11)

$$R_{u1u2}(\tau) = \frac{\sin(\pi(f_{s2} - f_{s1} + 2k_e\tau)(T_p - |\tau|))}{\pi(f_{s2} - f_{s1} + 2k_e\tau)} e^{+j\pi((f_{s2} - f_{s1})T_p + (f_{s2} + f_{s1})\tau + 2k_e T_p \tau)} \cdot \text{rect}\left[\frac{|\tau|}{T_p}\right]. \quad (2.18)$$

Although the expressions derived in appendix A can be used to determine the correlation between any two chirp waveforms, it is anticipated that practical radar system will use chirp waveforms of equal length ($T_{p1} = T_{p2}$) with $|k_{e1}| =$

$|k_{e2}|$ to keep the image quality independent of the type of chirp used for the actual pulse. The form most relevant for pulse coded chirp radar is given by cases 2 and 3 (see Fig. 2.5(b-c)), due to the corresponding low correlation, whereas case 1 (see Fig. 2.5(a)) gives a high correlation which is necessary for chirp compression.

In practice it is crucial to relate the various correlation functions to the parameters of the chirps, because this gives an indication of the required RF hardware and antenna performance. In the following, this is accomplished for different combinations of chirp rates and occupied frequency bands.

The influence of the occupied frequency bands for the case of inverse chirps is shown in Fig. 2.6. It is obvious that $R_{u1d2}(\tau)$ shows a higher suppression than $R_{u1d1}(\tau)$, since in addition to a reduced maximum it falls off rapidly for $\tau \neq 0$. It is deduced, that using an adjacent frequency band for the inverse chirp (cf. Fig. 2.6(b)) offers an additional suppression of the cross-correlation component. However, this also means a higher total bandwidth required for the RF hardware of the SAR system.

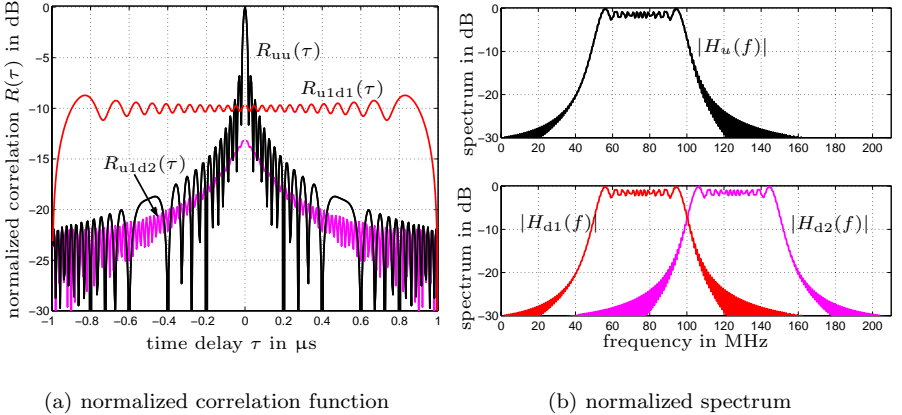


Figure 2.6: Correlation of two inverse chirps (i.e., $k_{e1} = -k_{e2}$) occupying identical $R_{u1d1}(\tau)$, and adjacent $R_{u1d2}(\tau)$ frequency bands, respectively. $B_w = 50$ MHz and $T_p = 1$ μs .

The influence of using similar or inverse chirps in adjacent frequency bands is shown in Fig. 2.7. Although the second chirp occupies the same frequency band in both cases (cf. Fig. 2.7(b)) the curve for the two correlation functions $R_{u_1u_2}(\tau)$ and $R_{u_1d_2}(\tau)$ is different. The inverse chirp $R_{u_1d_2}(\tau)$ shows a lower maximum as $R_{u_1u_2}(\tau)$, which makes it more suitable for the detection of point targets (cf. section 3.4).

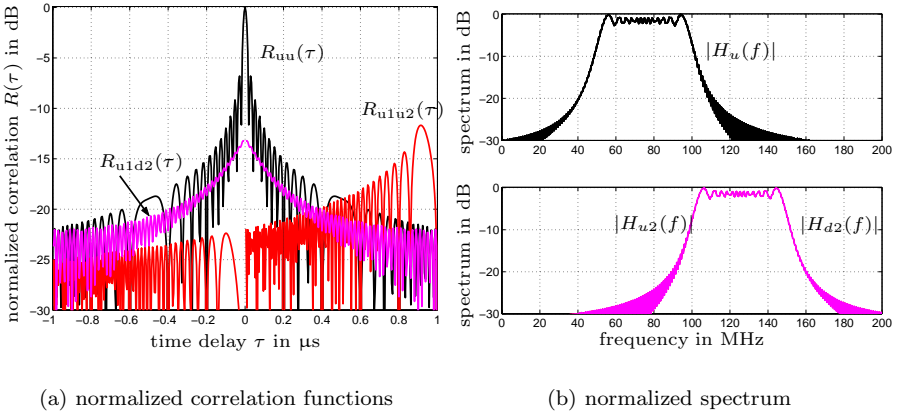


Figure 2.7: Cross-correlation of two chirps occupying adjacent frequency bands for different chirp rates $k_{e2} = \pm k_{e1}$ of the second chirp. $B_w = 50$ MHz and $T_p = 1$ μs for all chirps.

3 Synthetic Aperture Radar with Multiple Receivers

State-of-the-art synthetic aperture radar (SAR) systems operate in multiple modes. This is facilitated through electronically steered phased arrays using transmit/receive (T/R) modules, enabling analog beam-forming [66, 81, 46] by steering the main beam of the antenna. While offering the advantage of distributed power radiation, hardware redundancy and flexible operation modes, these systems suffer from high weight, low efficiency, high power consumption, limited coverage versus resolution, difficult calibration, and high cost (see chapter 2). However, one of the major disadvantages is the inherent loss of information through the analog beam-forming, since the total antenna footprint is reduced to a small fraction of the subarrays' footprints. Only the information on the small footprint can be extracted.

Overall, it can be stated that the price that was paid and is being paid for the advancement of technology is extremely high. Despite of this, the goal of wide coverage and high resolution is not reached, as stated in chapter 1. In spot mode operation the resolution is higher but the coverage is even lower compared to standard operation [20]. In scan mode operation a high coverage is achieved at the cost of a low resolution [23]. Hybrid, stripmap/spotlight techniques exist, which offer some compromise between high resolution and wide coverage [10, 62] but are still bound to the same basic constraints.

In this chapter a SAR system using digital beam-forming (DBF) with multiple receivers is considered. It will be shown how the DBF concept overcomes the above mentioned deficiencies of current systems. Basic expression for the performance parameters and design restrictions are developed in section 3.1. Section 3.2 summarizes the advantages of digital beam-forming with respect to conventional SAR. Later, in section 3.3 the fundamental constraints of the

DBF configuration are derived. In addition, the operation and the quality parameters of a SAR system using chirp coded waveforms (see section 2.6) is investigated in section 3.4. The chapter concludes by comparing the number values of a potential DBF SAR to those of an in-orbit SAR system.

3.1 System and Performance Parameters

In this section the system and performance parameters for the digital beam-forming on-receive-only configuration described in section 2.1 are derived. The SAR problem is formulated in a 2D ground plane geometry, thus, the radar and the imaged area lie on the xy -plane in the spatial domain. Fig. 3.1 shows the geometry which is a special case of the geometry described in section 2.2.

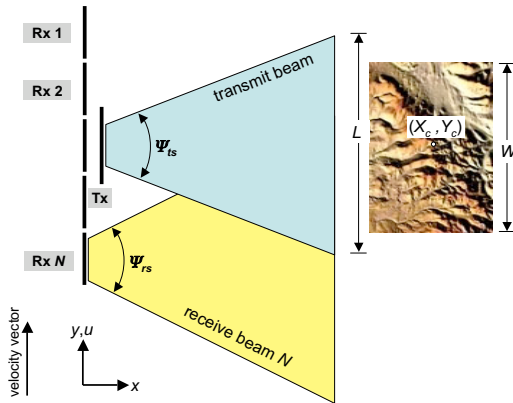


Figure 3.1: Digital beam-forming antenna setup and imaged area for a 2D ground plane geometry.

The 2D geometry is not a restriction to the generality of the problem, since the same principles apply to the 3D slant-plane geometry [90]. A total of N receive subarrays together with a single transmit antenna are moved along the y -direction ($x = 0$) in a side-looking, i.e., along the x -axis configuration. The receive array consists of *contiguous* subarrays, i.e., the spacing between the subarrays is equal to the subarray length. The synthetic aperture domain variable u is used to represent the positions of the subarray, while the position

of scatterers is described by the coordinates (x, y) . The imaged area of width W is within the cross-range interval $Y_c - W/2 < y < Y_c + W/2$ centered at Y_c . Each point within the imaged area is visible to the radar throughout the synthetic aperture length $L = \Psi_{ts} X_c$ where Ψ_{ts} is the HPBW of the transmit antenna and X_c is the range to the center of the imaged area.

In addition the “start-stop” approximation is adopted, i.e., no sensor movement between transmission and reception of a pulse. In the first order, the frequency dependency need not be considered, since the derived parameters are either normalized to the wavelength, or compared to the stripmap SAR.¹

The performance relative to a conventional stripmap SAR system is considered. The common parameter, when comparing both systems is the signal-to-noise ratio SNR , thus assuming similar RF-hardware for both systems. This is a conservative approach, since it takes no advantage of the separate sub-system optimization for the DBF configuration (cf. section 2.1) . Both DBF and stripmap systems shall cover the same swath, thus assuming equal beam widths in elevation.

3.1.1 Antenna Dimensions

In the following an expression for the antenna areas of the DBF configuration is derived, so as to yield an SNR equal to that of a conventional stripmap SAR.

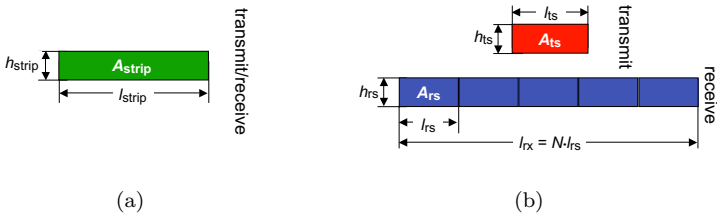


Figure 3.2: Antenna dimensions for (a) single-transmit/single-receive stripmap SAR system, and (b) single-transmit/multi-receive DBF SAR system.

¹Frequency dependent hardware performance, such as noise figure is not considered.

Starting point is the radar equation for extended targets stated in section 2.3. From (2.1) it is evident that the received power and thus the SNR is proportional to the antenna gain which in turn is proportional to the effective antenna area. Thus, for the mono-static stripmap SAR the SNR is proportional to the square of the effective Tx/Rx antenna area A_{strip} shown in Fig. 3.2(a). In the case of the bi-static DBF configuration of Fig. 3.2(b) the SNR is proportional to the product of the effective transmit A_{ts} and total effective receive A_{rx} antenna areas, where the receive antenna consists of N subarrays each of area A_{rs} .

Requiring equal SNR for the stripmap SAR and DBF-systems results in:

$$\begin{aligned} SNR_{\text{strip}} &\stackrel{!}{=} SNR_{\text{DBF}} \\ \Rightarrow A_{\text{strip}}^2 &\stackrel{!}{=} A_{\text{rx}} \cdot A_{\text{ts}}. \end{aligned} \quad (3.1)$$

Since both stripmap SAR and DBF systems cover identical swath widths, thus all antennas have equal heights $h_{\text{strip}} = h_{\text{rs}} = h_{\text{ts}} = h$. Writing the antenna area as the product of length and height $A = l \cdot h$, results in the following expression:

$$A_{\text{strip}}^2 = l_{\text{strip}}^2 h^2 = N l_{\text{rs}} l_{\text{ts}} h^2 \quad (3.2)$$

where $N l_{\text{rs}}$ is the total length of the N receive subarrays. The expression relates the lengths l_{strip} , l_{rs} , and l_{ts} of the stripmap SAR, single receive and single transmit subarray antennas, respectively.

In order to avoid azimuth ambiguities the receive subarray length l_{rs} should be less than the transmit antenna length l_{ts} as detailed in section 3.1.2. At this time it is sufficient to consider the lengths ratio to be known and given by

$$a_{\text{az}} = \frac{l_{\text{rs}}}{l_{\text{ts}}} \quad , \quad a_{\text{az}} \leq 1. \quad (3.3)$$

Substituting (3.3) into (3.2) gives an expression for the transmit and receive antenna areas

$$A_{\text{ts}} = h l_{\text{ts}} = \frac{A_{\text{strip}}}{\sqrt{N a_{\text{az}}}} \quad (3.4)$$

$$A_{\text{rs}} = h l_{\text{rs}} = A_{\text{strip}} \sqrt{\frac{a_{\text{az}}}{N}} \quad (3.5)$$

which when written in terms of the antenna lengths this gives

$$l_{ts} = \frac{l_{\text{strip}}}{\sqrt{N} a_{az}} \quad (3.6)$$

$$l_{rs} = l_{\text{strip}} \sqrt{\frac{a_{az}}{N}}. \quad (3.7)$$

The total antenna area of the bi-static configuration is

$$A_{\text{bi}} = A_{\text{ts}} + A_{\text{rx}} = A_{\text{ts}} + N A_{\text{rs}} \quad (3.8)$$

and by substituting (3.4) and (3.5) into the above equation results in (3.9), which is useful when comparing the areas of the DBF and stripmap antennas

$$A_{\text{bi}} = A_{\text{ts}} + A_{\text{rx}} = A_{\text{strip}} \left(\frac{1}{\sqrt{N} a_{az}} + \sqrt{N a_{az}} \right). \quad (3.9)$$

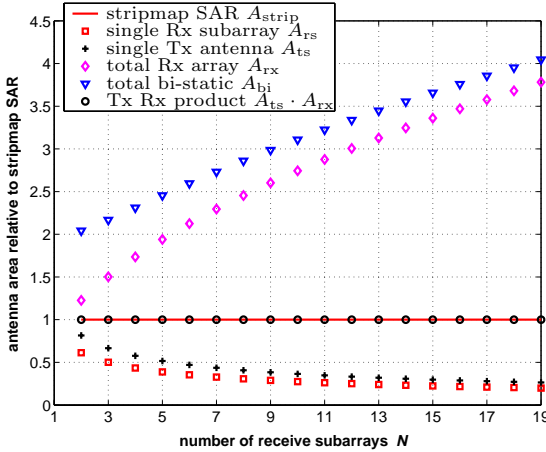


Figure 3.3: Comparison of stripmap SAR and DBF SAR antenna areas. All areas are normalized to the area of the stripmap SAR antenna A_{strip} .

The above expressions gives a DBF antenna length which results in a total received power, and thus SNR , equal to that of a conventional stripmap SAR system. Fig. 3.3 shows the respective antenna areas normalized to A_{strip} as a function of the number N of receive subarrays. The ratio of receive subarray to

transmit antenna area is given by $a_{az} = 0.752$. It is deduced that both, transmit antenna and single subarray of the DBF configuration are smaller than the SAR antenna, while the total area of the receive array, i.e., $A_{rx} = NA_{rs}$, is larger. The product of transmit and receive antenna areas is equal to unity, which validates the condition for equal SNR .

3.1.2 Maximum Length of Receive Subarray

The footprint of the transmit antenna in the DBF configuration illuminates the complete area to be imaged. The footprint of each receive subarray is to illuminates at least this area. Since the beam width (and thus footprint) of an antenna is inversely proportional to its length [67], the upper boundary for the receive subarray length is $l_{rs} \leq l_{ts}$. However, an additional and more strict requirement is that the spacing between the subarrays is such as to avoid azimuth ambiguities. In the following a mathematical expression is derived relating the receive subarray length to the transmit half power beam width (HPBW).

The data of the received array is focused within the angular segment covered by the transmit antenna. Using antenna terminology the beam of the receive array (length l_{rx}) is steered², within the angular segment Ψ_{ts} covered by the transmit antenna. The maximum steer angle $\psi_{o,max}$ being

$$|\psi_{o,max}| = \Psi_{ts}/2. \quad (3.10)$$

Azimuth ambiguities occur at angles ψ_{amb} given by³ [88]

$$\sin(\psi_{amb,\nu}) = \frac{\nu\lambda}{l_{rs}} + \sin(\psi_o) \quad , \quad \nu \in \mathbb{Z} \quad (3.11)$$

where $|\nu| \geq 1$ gives the order of the ambiguity. The spacing l_{rs} should be chosen such that the azimuth ambiguities occur outside the angular segment covered by the transmit antenna. Requiring the angle of the first order ambiguity to be *outside* the HPBW of the transmit antenna gives

$$\psi_{amb,\nu=\pm 1} \notin \left[-\gamma \frac{\Psi_{ts}}{2}; +\gamma \frac{\Psi_{ts}}{2}\right] \quad , \quad \gamma \geq 1 \quad (3.12)$$

²The term *steer* should be used with caution to avoid misunderstanding, since the data processing (see chapter 4) does not involve a *beam steering* as know from phased arrays.

³A detailed and more general treatment of this expression is given in section 5.6.2.

where γ is a *safety factor* which specifies how far outside the main beam the ambiguity can occur. For $\gamma = 1$ the first order ambiguity will be just at the edge, i.e., the -3 dB angle, of the main beam. Inserting the above conditions into (3.11) and solving for the first order ambiguity $\nu = 1$ and maximum steering angle (3.10), gives an expression for the maximum allowable spacing between the receive subarrays

$$l_{rs} \leq \frac{\lambda}{\sin(\Psi_{ts}/2) + \sin(\gamma\Psi_{ts}/2)}. \quad (3.13)$$

Since the HPBW of an antenna is inversely proportional to its length, the above condition really relates the transmit and receive antenna lengths. For all practical purposes (3.13) results in $l_{rs} < l_{ts}$.

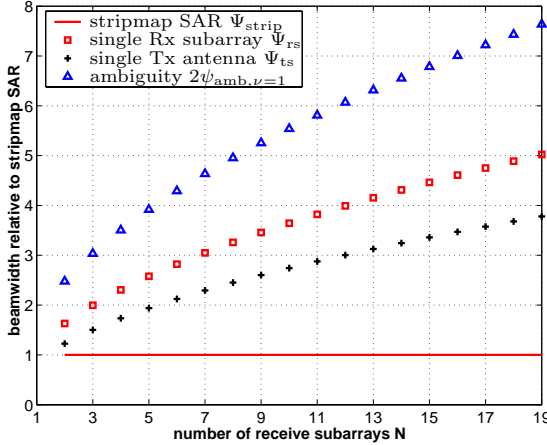


Figure 3.4: Azimuth HPBWs of DBF antennas relative to stripmap SAR antenna.

For a given stripmap antenna area the dimensions of the DBF antennas are obtained through (3.4) and (3.5), while satisfying (3.13). The resultant half power beam width as a function of the number of receive aperture is shown in Fig. 3.4. As expected the HPBW of the single transmit/receive subarrays are larger than the HPBW of the stripmap antenna. The HPBW of the transmit antenna corresponds to the along-track coverage of the SAR. Fig. 3.4 also shows the angle of the first order ambiguities $\psi_{amb, \nu=\pm 1}$. It is seen that all ambiguities lie outside the HPBW illuminated by the transmit antenna.

For example, $N = 7$ receive subarrays are sufficient for the DBF system to illuminate more than two times the azimuth angular width of the stripmap system, without any ambiguities within the antenna beam. Figure 3.5 shows the calculated azimuth antenna patterns for this case and compares it to the pattern of the reference stripmap antenna ($l_{\text{strip}} = 120\lambda$). A second order Kaiser amplitude taper function [47] is applied on the subarrays and the maximum of the beam is steered to the -3 dB angle of the transmit beam. It is seen that the first order ambiguity at $\psi_{\text{amb},\nu=1} = -0.98^\circ$ is attenuated by 17.3 dB relative to the beam maximum at $\psi_0 = 0.45^\circ$. An arbitrary high ambiguity attenuation can be achieved by choosing a higher safety factor γ in (3.13). However, increasing the attenuation of the ambiguity is paid for by shorter receive subarray length and a shorter cross-range sampling distance as shown in the following section.

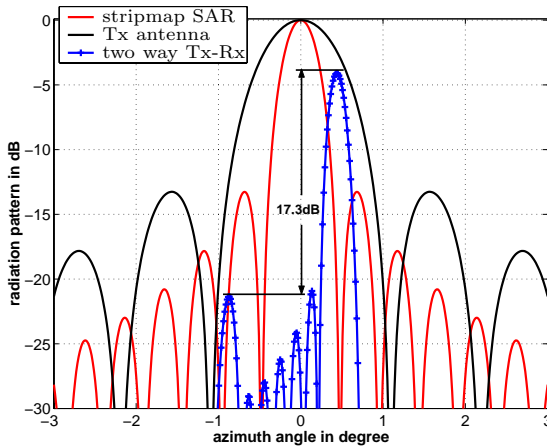


Figure 3.5: Calculated stripmap SAR and DBF transmit antenna patterns together with the two way Tx–Rx DBF antenna pattern for $N = 7$ subarrays.

3.1.3 Cross-Range Sampling Distance

The maximum sampling distance is determined by the cross-range spatial-frequency support of the signals. This is used to derive the cross-range sample spacing for the DBF configuration.

3.1.3.1 General Form of Nyquist Criteria

Since all scatterers within the imaged area contribute to the total support band of the received signal [92], the support band in the spatial-frequency domain is bounded to

$$k_u \in \left[2k \frac{Y_c - W/2}{X_c}, 2k \frac{Y_c + W/2}{X_c} \right] \quad (3.14)$$

where the extent and the center of the support band are given by

$$\Omega_{k_u} = \frac{2kW}{X_c} \quad (3.15)$$

$$k_{u,\text{center}} = \frac{2kY_c}{X_c}, \quad (3.16)$$

respectively. According to the Nyquist criteria the maximum sample spacing Δu_r is

$$\Delta u_r = \frac{2\pi}{\Omega_{k_u}} = \frac{\lambda X_c}{2W}. \quad (3.17)$$

For $W = L$ and approximating the HPBW of the transmit antenna by $\Psi_{ts} \approx \lambda/l_{ts}$, results in

$$\Delta u_r = l_{ts}/2. \quad (3.18)$$

which is the well known sampling requirement for stripmap SAR, stating that “The SAR must transmit at least two pulses as its physical antenna passes a stationary point in space” [99].

3.1.3.2 Sampling Requirement for DBF Configuration

In Fig. 3.6 the location of the Tx antenna at two instances is shown. In the following the maximum allowable distance Δu_t traveled by the radar between two successive transmitted pulses is derived.

In section 3.1.2 it was stated, that the length of the receive subarray l_{rs} is less than the length of the transmit antenna l_{ts} . Thus each receive subarray covers an angular segment larger than the transmit antenna. A conservative condition would relate the sample spacing to the receive subarray which dictates the spatial-frequency support band. The approach is conservative because in practice it can be assumed that all contributions to the support band origin from scatterers illuminated by the, smaller, beam width of the transmit antenna.

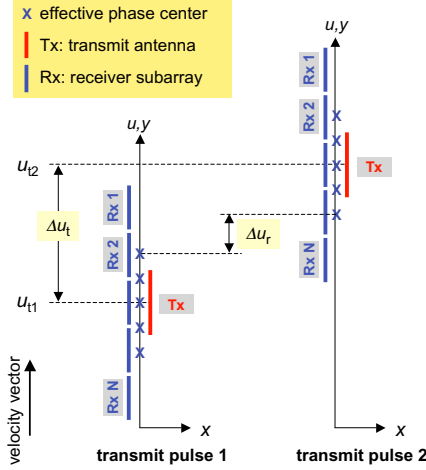


Figure 3.6: Position of subarrays and phase centers at two time instances corresponding to two transmitted pulses.

For a transmit antenna positioned at an arbitrary u_{t1} the receive subarrays' positions are $u_r = u_{t1} + nl_{rs}$, where n is an integer $n \in [-(N-1)/2, +(N-1)/2]$ for N odd. The effective phase center of a bi-static configuration is positioned midway between the transmit and receive aperture.⁴ Thus the signal is sampled at (cf. Fig. 3.6)

$$u = \frac{(u_{t1}) + (u_{t1} + nl_{rs})}{2} = u_{t1} + n \frac{l_{rs}}{2} \quad (3.19)$$

the samples are separated by $l_{rs}/2$ which satisfies the condition given by (3.18) for maximum possible Ω_{k_u} since $l_{rs} \leq l_{ts}$. The samples span a distance $(N-1)l_{rs}/2$. To ensure a continuous uniform sampling at $l_{rs}/2$ the next pulse should be transmitted when the array is positioned at u_{t2} such that

$$\left[u_{t2} - \left(\frac{N-1}{2} \right) \frac{l_{rs}}{2} \right] - \left[u_{t1} + \left(\frac{N-1}{2} \right) \frac{l_{rs}}{2} \right] \stackrel{!}{=} \frac{l_{rs}}{2} \quad (3.20)$$

which after simplification gives the value for the cross-range array sampling

⁴The phase center gives the *virtual* position of a mono-static (transmit/receive) antenna replacing the bi-static setup. This assumption about the position of the phase center will be relaxed and generalized in section 4.2.3.

distance

$$\Delta u_t = u_{t2} - u_{t1} = \frac{N}{2} l_{rs}. \quad (3.21)$$

For each transmitted pulse the receive signal is sampled every Δu_r , whereas the Tx separation between successive pulses is Δu_t . Each individual Rx under-samples the azimuth spectrum (sample spacing Δu_t) but evaluating the signals from all subarrays (sample spacing Δu_r) will result in an alias free spectrum.

Figure 3.7 shows the sample spacing resulting from (3.21) and (3.18), respectively. It is seen that increasing the number of subarrays (which also means an increased HPBW and synthetic aperture length L as seen from Fig. 3.4) results in a smaller sample spacing Δu_r , however increasing the number of subarrays N increases the distance Δu_t since more receive samples are taken for each transmitted pulse.

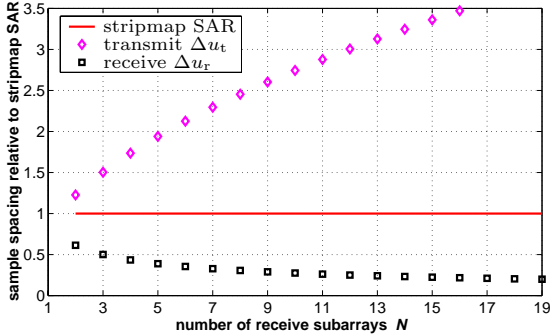


Figure 3.7: Maximum transmit Δu_t and receive Δu_r sample spacing of DBF configuration relative to stripmap SAR.

3.1.4 Minimum Pulse Repetition Frequency

The lower bound for the pulse repetition frequency PRF is given by the maximum allowable distance traveled by the radar platform between successive transmitted pulses. For DBF SAR the receive subarrays acquire N samples for each transmitted pulse and the PRF is directly related to the distance Δu_t through the platform velocity V . The maximum Δu_t is given by (3.21) and

the corresponding PRF is

$$PRF = \frac{V}{\Delta u_t} = \frac{2V}{Nl_{rs}}. \quad (3.22)$$

As shown in Fig. 3.8 the PRF decreases with respect to stripmap SAR. The fact that the minimum PRF is reduced for DBF SAR opens an attractive possibility to increase the swath width. The swath width of most spaceborne SAR systems is limited due to the minimum PRF limit. Reducing this limit leads to a possible increase in swath width (also see section 3.3.3).

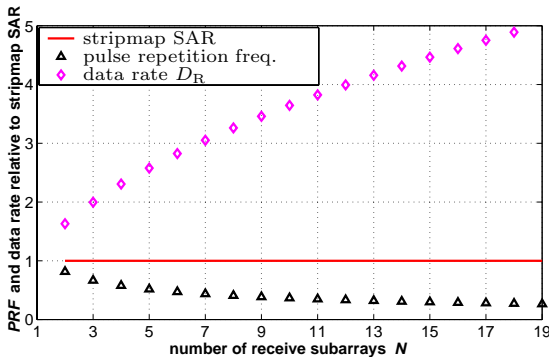


Figure 3.8: Minimum pulse repetition frequency PRF and data rate of DBF configuration relative to stripmap SAR.

3.1.5 Data Rate

Spaceborne and airborne synthetic aperture radar system generate a very large amount of raw data which, till now, is mostly processed on the ground. Specifically for satellite based SAR systems the data needs to be telemetered to the ground, which is subject to the possible data rate and availability of ground stations. For airborne or shuttle missions, the data needs to be locally stored for later processing. Although there are some trends towards on-board data compression [85, 53] and processing [103, 82, 102], which would greatly reduce the amount of data that needs to be stored or telemetered, it is anticipated that within the near future most data will still be processed on the ground, basically

because most often the processing is manually adapted and tuned depending on the requirements.

The data rate D_R in bit/s appropriate to a SAR system (assuming no over-sampling) is given by [23]

$$D_R = n_B \cdot N B_w \left(\frac{2}{c_0} (R_{\text{far}} - R_{\text{near}}) + T_p \right) \cdot PRF \quad (3.23)$$

where n_B is the number of bits per complex sample; B_w is the pulse bandwidth; R_{far} and R_{near} are the near and far ranges, respectively; and T_p is the pulse duration⁵. SAR raw data has a high data rate, e.g. 100 Mbit/s for ERS-1 and > 1 Gbit/s for future SAR systems [53].

The above expression is valid both for a DBF SAR with N subarrays (channels) and for a conventional stripmap SAR with $N = 1$ Tx/Rx antenna. It should, however, be noted that the data rate does not increase linearly with the number of channels, as (3.23) would suggest on the first look. The reason is that, as shown in the last section, the PRF is reduced when increasing N . To clarify this point, the relative increase in data rate as compared to a conventional stripmap SAR is investigated assuming otherwise identical parameters of both systems:

$$\frac{D_{R_{\text{DBF}}}}{D_{R_{\text{strip}}}} = \frac{N \cdot PRF_{\text{DBF}}}{PRF_{\text{strip}}}. \quad (3.24)$$

Substituting for the PRF and the associated sample spacing Δu gives:

$$\frac{D_{R_{\text{DBF}}}}{D_{R_{\text{strip}}}} = \sqrt{\frac{N}{a_{\text{az}}}} \quad (3.25)$$

which shows, that the data rate is proportional to \sqrt{N} (assuming a constant a_{az}). Fig. 3.8 shows the relative increase in data rate as a function of the number of subarrays for a DBF configuration.

However, the above still overestimate the data rate of the DBF system. As shown in [50] the number of bits n_B necessary for the DBF configuration can be reduced. The principal consideration is that the SNR of the single DBF channel is reduced in comparison to conventional SAR (due to the reduced

⁵The near and far slant-ranges $R_{\text{near},\text{far}}$ are introduced in section 3.3; at this point they are of no significance for the results and can be assumed constant.

single subarray's area, cf. section 3.1.1), hence the input power of the analog-to-digital converter (ADC) is largely determined by thermal noise. This leads to a reduced signal dynamic and thus a reduced number of bits n_B [22].

3.1.6 Resolution

The cross-range resolution for a scatterer at (x_n, y_n) is space variant and can be derived from the spatial-frequency support band of the scatterer. For a DBF SAR, all scatterers within $u \in [y_n - L/2, y_n + L/2]$ are observable to the radar. The spatial-frequency support band is bounded to

$$k_u \in \left[2k \frac{y_n - L/2}{x_n}, 2k \frac{y_n + L/2}{x_n} \right]. \quad (3.26)$$

and the extent of this band for scatterer n is

$$\Omega_{k_{un}} = \frac{2kL}{x_n} \quad (3.27)$$

which is independent of the cross-range position of the scatterer. The resolution is [92]

$$\delta y_n = \frac{2\pi}{\Omega_{k_{un}}} = \frac{\lambda x_n}{2L}. \quad (3.28)$$

Taking the resolution for the center of the imaged area (X_c, Y_c) gives

$$\delta y_{\text{DBF}} = \frac{\lambda X_c}{2L}. \quad (3.29)$$

Again $\delta y_{\text{DBF}} = l_{\text{ts}}/2$ for $\Psi_{\text{ts}} \approx \lambda/l_{\text{ts}}$. A plot of the relative resolution $\delta y_{\text{DBF}}/\delta y_{\text{strip}}$ is shown in Fig. 3.9. The resolution improves with the number of subarrays and is higher than for stripmap SAR. This is because the Tx antenna length can be made shorter while keeping a constant *SNR* with respect to the conventional SAR.

3.1.7 Azimuth (Along-Track) Coverage

Similar to stripmap SAR, the DBF SAR has a continuous coverage, since no analog beam-forming is performed, but in opposite to the former, the data from

the complete azimuth angular segment is preserved. Fig. 3.9 shows that the along-track coverage is higher than for stripmap SAR and that it increases with increasing number of subarrays. If required, the coverage can be reduced by partially combining the digital subarray signals prior to azimuth compression, which serves to reduce the data rate. However, unlike spot operation mode, a reduced coverage will not yield a higher resolution.

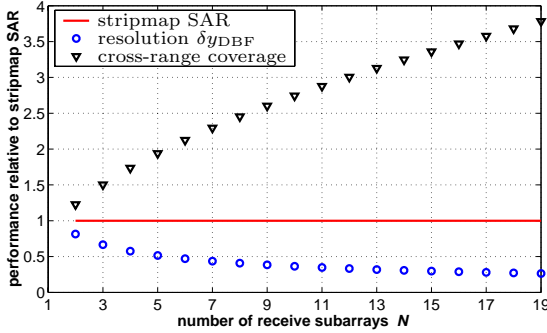


Figure 3.9: Resolution δy_{DBF} and azimuth (cross-range) coverage of the DBF configuration relative to stripmap SAR.

3.2 Summary on the Performance Parameters

The investigations of the previous section showed that: the receive sampling distance Δu_r decreases with respect to the stripmap SAR, because the covered cross-range angular segment is increased. Increasing the number of subarrays reduces Δu_r since the subarray length l_{TS} is reduced. However, the minimum transmit sampling distance Δu_t increases when increasing the number of subarrays. This distance is inversely proportional to the minimum PRF , which will decrease with increasing N and is smaller than for stripmap SAR. As a result of the lower minimum limit for the PRF the unambiguous range and swath width can be increased for a DBF SAR, which is a highly attractive “side effect” of using multiple receive subarrays. The azimuth resolution δy_{DBF} improves with respect to stripmap SAR. This is obvious, since the resolution depends primarily on the synthetic aperture length, which is increased for the

DBF SAR. But the data rate is also increased with respect to stripmap SAR. For each transmitted pulse the received signals from all N channels need to be digitized. Nevertheless, the investigation showed that, in the first order, the data rate is proportional to \sqrt{N} . Finally it should be noted that the resolution depends on the synthetic aperture length L , whereas the sample spacing in the synthetic aperture domain depend on the width W of the area to be imaged.

An important conclusion resulting from the investigation of the performance parameters is that digital beam-forming inherently implements an arbitrary number of *simultaneous* operation modes, since resolution and coverage are not contradicting requirements but instead, they are specified independently. Thus the various operation modes of state-of-the-art T/R module based systems turn out to be dispensable, when using a DBF SAR.

The expressions derived up to now are related to specific performance parameters. The next sections give a more general overview over system performance restrictions.

3.3 Fundamental Constraints on the System Performance

This section deals with conceptual performance, as opposed to technological implementation, and will concentrate on system solutions that exploit digital beam-forming. The fundamental restrictions imposed by various operating factors for a DBF SAR system will be stated and compared to conventional stripmap SAR.

In this section the 2D geometry assumed in section 3.1 will be dropped in favor of the 3D slant-plane imaging geometry shown in Fig. 3.10 that exists in practice. The radar path is assumed to be along the y -axis ($x = x_1$) at a height of $z = |z_n|$ above ground. The distance to the nearest and farthest point within the swath X_0 is given by R_{near} and R_{far} , respectively. The results derived earlier using the 2D geometry are still valid when introducing the *slant-range* R_s such that [90]:

$$R_s = \sqrt{(x_1 - x_n)^2 + z_n^2} \quad (3.30)$$

which replaces the (former) range variable x . The imaged area is on the $z = -z_n$ plane. For spaceborne systems the Earth's curvature should be taken into account, for this the relation between the local angle of incidence ϑ_i and the slant-range R_s is given in appendix B.2.

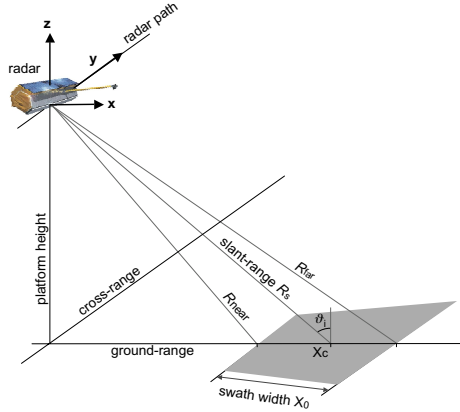


Figure 3.10: 3D slant-range SAR geometry.

3.3.1 Signal-to-Noise Ratio of Processed Image

Consider the bi-static radar equation (2.2) given in section 2.3 and suppose the main beam of the radar views a single terrain element of extent δx in ground-range and δy in cross-range (these are the SAR resolution). The extent of the area $\delta x \delta y$ is assumed small enough so that the variation of the radiation patterns $C_{ts,rs}$ and r are negligible when integrating over the resolution cell⁶. Using (2.2) the SNR for this terrain element with mean backscatter σ_0 and slant-range position R_s is:

$$SNR = \frac{P_t \lambda^2 G_{ts} G_{rs} \sigma_0 \delta x \delta y}{(4\pi)^3 R_s^4 \cdot k T_{sys} B_N L_{feed}}. \quad (3.31)$$

Within the length of the synthetic aperture L the terrain element is in view of the moving radar, during this period several echo signals are recorded and

⁶Stated differently, the angles ϑ , ψ and the slant-range $r = R_s$ can be assumed constant.

processed. For the image formation, a total number of N_{proc} data samples are processed coherently to produce a single image resolution cell. The thermal noise samples can be taken as independent from sample to sample within each pulse, and from pulse to pulse. As a result of coherent processing of the input samples, the SNR_{image} at the output of the processing improves by a factor N_{proc} , i.e.,

$$SNR_{\text{image}} = SNR \cdot N_{\text{proc}} = SNR \cdot N_{\text{pulse}} N_{\text{az}} N \quad (3.32)$$

where N_{pulse} (time) samples per pulse, and N_{az} samples within the synthetic aperture length L are acquired by each of the N receive subarrays. The number $N_{\text{proc}} = N_{\text{pulse}} N_{\text{az}} N$ is equal to the dimension of the compression filter used for SAR image formation⁷. It remains to express N_{pulse} and N_{az} in terms of factors in (3.31). The return pulse of length T_p second is sampled at a rate of B_w Hertz, to produce

$$N_{\text{pulse}} = T_p B_w \approx T_p B_N \quad (3.33)$$

samples per pulse, where B_w is the bandwidth of the chirp signal. From section 3.1.3 it is known, that the azimuth sample spacing is Δu_t , thus

$$N_{\text{az}} = \frac{L}{\Delta u_t} = \frac{L}{V/PRF} \quad (3.34)$$

pulses are transmitted during the time the terrain element is in view of the radar. Substituting (3.34) into (3.32) and (3.29) into (3.31) yields a relation for the SNR after processing, which is further simplified by expressing the peak transmit power in terms of the average power $P_t = P_{\text{av}}/(T_p \cdot PRF)$. Finally:

$$SNR_{\text{image}} = \frac{P_{\text{av}} N G_{\text{ts}} G_{\text{rs}} \lambda^3 \sigma_0 \delta x}{2(4\pi R_s)^3 V \cdot kT_{\text{sys}} L_{\text{feed}}}. \quad (3.35)$$

This is the general SAR radar equation valid for the quasi bi-static DBF configuration where the same distance R_s to the —different— Tx and Rx antennas is assumed. It expresses the average signal-to-noise ratio of a SAR image resolution cell $\delta x \delta y$ of mean RCS σ_0 . Note that the azimuth resolution δy does not appear explicitly in form given above. The radar equation is valuable as an indicator of the role of various SAR system parameter in the SNR of the processed image. For conventional stripmap SAR (i.e., $N = 1$ and $G_{\text{ts}} = G_{\text{rs}}$)

⁷The dimensionality of the DBF SAR data space is treated in chapter 4, however the expression for N_{proc} already suggests three dimensions.

the above equation reduces to the results known for mono-static SAR found for example in [22].

3.3.2 Noise Equivalent Sigma Zero

A quantity directly related to the SAR radar equation is the noise equivalent sigma zero (*NESZ*). The *NESZ* is the mean radar cross section (backscatter coefficient) necessary to produce a SNR_{image} of unity. The *NESZ* can be interpreted as the smallest target cross section which is still detectable by the SAR system against thermal noise. Setting $SNR_{\text{image}} = 1$ in (3.35) gives

$$NESZ = \frac{2(4\pi R_s)^3 V \cdot kT_{\text{sys}} L_{\text{feed}}}{P_{\text{av}} N G_{\text{ts}} G_{\text{rs}} \lambda^3 \delta x}. \quad (3.36)$$

By rearranging the terms using $G_{\text{ts,rs}} = 4\pi A_{\text{ts,rs}}/\lambda^2$, the *NESZ* can be written in terms of the antenna areas

$$NESZ = \frac{8\pi R_s^3 V \lambda \cdot kT_{\text{sys}} L_{\text{feed}}}{P_{\text{av}} N A_{\text{rs}} A_{\text{ts}} \delta x}. \quad (3.37)$$

3.3.3 Trade-off between Resolution and Swath Width

One of the fundamental restrictions of SAR systems performance is given by the contradicting requirement for wide swath (range coverage) and high azimuth resolution. The principal reason leading to this contradiction can easily be understood when realizing that an increase in azimuth resolution requires an increase in azimuth beam width, which leads to a shorter antenna length and thus a higher *PRF* for adequate azimuth sampling. However, increasing the *PRF* will lead to range ambiguities, when pulses scattered from different points within the imaged area overlap. This requires a reduction of the elevation beam width and thus a reduced swath. Mathematically this contradiction is described in [22, 33, 41] by the *minimum antenna area constraint*. This constraint states that antennas used in SAR systems must have a certain minimum area for the design to be viable. It applies for the case of best possible resolution and widest possible swath. SAR system operation with antennas smaller than the

minimum size is possible if either resolution or swath width is sacrificed [41]. In the following, the minimum antenna area constraint is derived for the DBF SAR configuration.

An upper limit for the PRF of a SAR is given by the need to avoid ambiguous scatterer returns in range. These ambiguities are due to radar returns from targets lying at ranges that correspond to a time-of-flight greater than the pulse repetition interval (PRI). Referring to Fig. 3.10 it means that

$$\frac{2R_{\text{far}}}{c_0} < \frac{2R_{\text{near}}}{c_0} + PRI \quad (3.38)$$

where the near and far slant-range R_{near} and R_{far} , respectively, are related to the swath width X_0 through the angle of incidence⁸

$$X_0 = \frac{R_{\text{far}} - R_{\text{near}}}{\sin \vartheta_i}. \quad (3.39)$$

Rearranging (3.38) to relate the swath width X_0 to the pulse repetition frequency $PRF = 1/PRI$ gives:

$$X_0 \leq \frac{c_0}{2PRF \cdot \sin \vartheta_i} \quad (3.40)$$

Combining (3.40) with (3.22) results in

$$\frac{2X_0 \sin \vartheta_i}{c_0} \leq \frac{1}{PRF} \leq \frac{Nl_{\text{rs}}}{2V} \quad (3.41)$$

which is a basic constraint for SAR systems. Next, the above expression is rearranged to emphasize on different aspects.

First, the swath width is written in terms of the HPBW of the transmit antenna Θ_{ts} and the slant-range to the center of the imaged area R_c

$$X_0 = \frac{\Theta_{\text{ts}} R_c}{\cos \vartheta_i} \approx \frac{\lambda R_c}{h \cos \vartheta_i}. \quad (3.42)$$

⁸The expression is not valid for very wide swath SAR where the incident angle ϑ_i varies significantly across the swath. However it is straight forward to generalist the equation for this case.

By inserting the above approximation into (3.41) the following restriction for the antenna area is obtained

$$hl_{rs} = A_{rs} \geq \frac{4V\lambda R_c \tan \vartheta_i}{c_0} \cdot \frac{1}{N}. \quad (3.43)$$

With the exception of the factor $1/N$ the above expression is identical to the minimum antenna area constraint as derived in [22, 41]. Clearly the minimum single subarray area of the DBF system is N -times smaller than the respective area of a conventional SAR. In practice this offers the SAR system designer a greater degree of freedom in choosing system parameters without violating the antenna area constraint.

Second, an expression relating the azimuth resolution and the swath width is found by substituting (3.29) together with (3.3), i.e.,

$$\delta y = \frac{\lambda R_c}{2L} \approx \frac{l_{ts}}{2} = \frac{l_{rs}}{2} \frac{1}{a_{az}} \quad (3.44)$$

into (3.41) and rearranging to point out the relationship between swath width and azimuth resolution

$$\frac{X_0}{\delta y} < \frac{c_0}{2V \sin \vartheta_i} (Na_{az}) \quad (3.45)$$

where $c_0/2V$ is nearly constant at 20 000 for low earth orbit satellites and typically in the range of 300 000–750 000 for airborne systems.

The *fundamental constraint* is actually given in (3.45), which places an upper limit on the ratio of the swath width versus azimuth resolution. It requires that the swath width X_0 decreases as the azimuth resolution δy improves (i.e., becomes smaller). In contrast to [22, 41] the relation not only depends on the platform velocity V and the angle of incidence ϑ_i but also on the number of receive subarrays. For DBF SAR the upper limit for the ratio is always higher than for conventional SAR, since $Na_{az} > 2$ is always satisfied.

3.4 Pulse Coded Chirp Waveforms in Imaging Radar

In the most general sense, the approach followed in this section is known as *pulse coding* (also referred to as *waveform diversity*). The use of pulse coding in imaging systems is considered an additional challenge, since the imaged area consists of *distributed scatterers* all of which contribute to the total received signal. Methods well suited for the detection of point targets turn out to be useless for imaging radar because the energy from scatterers outside the focused resolution cell cause a degradation of signal quality [53, 17]. In imaging radar the additional requirement is that the waveforms remain uncorrelated independently of their relative time (phase) shift.

Digital pulse coding is reported in [4, 53] for the reduction of range ambiguities. In [115] a design procedure for appropriate coded pulse radar waveforms is introduced (but no example codes or simulation results are given). An overview over coded waveforms can be found in [44], where the focus is on reverse-slope chirp waveforms (which is a special case of the approach followed here). Several of the ideas in [44] have been investigated in detail by [94]. In [18] some previously suggested techniques for extending the swath of SAR without loss of along-track resolution are investigated; basically the conclusion of [18] is that when using a simple, single feed antenna, the illumination of range-ambiguous regions always results in severe image degradation.

While in the previous section it was shown that both swath width and azimuth resolution can be increased by using multiple receive subapertures, this section investigates the use of pulse coded chirp waveforms to allow increasing the unambiguous range (swath width) while maintaining the same effective *PRF*.

Next, the operation of a SAR system using pulse coded chirps is introduced. This is closely related to the range compression and the chirp correlation functions derived in section 2.6. Further, a quality criterion for comparing the performance of different chirp waveforms is derived in section 3.4.2. This quality criterion, suited for imaging radar, is then used to investigate the influence of various chirp parameters. Simulation results for a SAR system utilizing coded chirp waveforms will be presented later in section 4.5.3.

3.4.1 Principle of Operation

The simplified SAR geometry shown in Fig. 3.11 contains two point scatterers positioned in two different range zones within the imaged area. The response of a single pulse shows one echo corresponding to each scatterer with no ambiguities as seen from Fig. 3.12 (top). In the case of repeated transmitted pulses the received echos are also repeated by the pulse repetition interval PRI . The multiple echos can no longer be uniquely associated to the scatterers and range ambiguities will occur as illustrated in Fig. 3.12 (middle). The idea behind the use of coded pulse waveforms is to allow the echos received from subsequent pulses to fall within one range zone, but the transmitted pulses are *marked* as shown in Fig. 3.12 (bottom). The response is then correlated with each of the transmitted waveforms to suppress the unwanted (ambiguous) signal as shown in Fig. 3.13. Note that the returns from A and B are clearly distinguishable if the peak of the auto-correlation function (similar waveforms) is high with respect to the cross-correlation function (different waveforms). For perfectly uncorrelated waveforms, the unwanted signal would be completely suppressed.

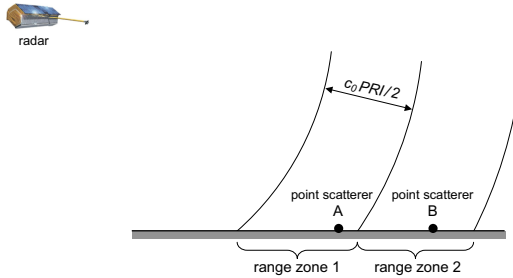


Figure 3.11: Geometry and position of point scatterers in different range zones.

At this point it should be noted, that when using p pulse coded waveforms the pulse repetition interval PRI between the pulses can be reduced by the factor p , without causing an overlap of similar pulses⁹. Extending the results of (3.40) to this case gives

$$\frac{PRI}{p} \leq \frac{c_0}{2X_0 \cdot \sin \vartheta_i} \tag{3.46}$$

⁹The PRI is understood as the minimum time interval between any two pulses.

which means that, either the *PRF* can be increased by the factor p for example in conjunction with a shorter antenna to yield an increased azimuth resolution; or the swath width X_0 increased by the factor p while keeping the *PRF* unchanged. Nevertheless, the minimum sampling constraint is unchanged when using pulse coded waveforms.

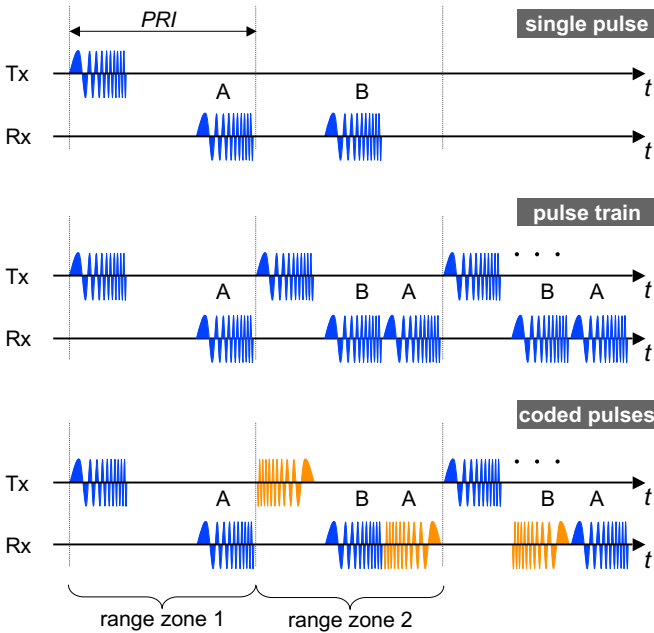
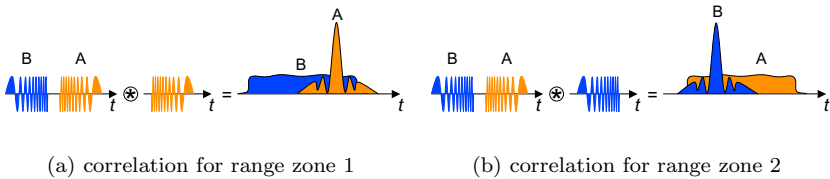


Figure 3.12: Response for single pulse (top), pulse train (middle), and coded pulse train (bottom).



(a) correlation for range zone 1

(b) correlation for range zone 2

Figure 3.13: Concept of coded pulses to suppress range ambiguities.

3.4.2 Quality Criterion for the Comparison of Correlation Functions

For radar systems using pulse coding a quantity of interest is the relative level between the correlation of identical (wanted) chirp waveforms to the correlation of different (unwanted) chirp waveforms. This quantity is given by the *range ambiguity ratio* (RAR) which is defined as¹⁰

$$RAR_{u1d2}(\tau) = \frac{R_{uu}(\tau = 0)}{|R_{u1d2}(\tau)|} = \frac{T_p}{|R_{u1d2}(\tau)|} \quad \forall \quad -T_p < \tau < T_p \quad (3.47)$$

where the same subscript convention as in section 2.6.2 is used to indicate the type of chirp and occupied frequency band. Referring to Figs. 2.6 and 2.7 of the same section, the RAR is the *difference* between $\max\{R_{uu}(\tau)\}$ and the respective correlation functions. A high value $RAR(\tau)$ indicates a good suppression of the unwanted cross-correlation component.

In imaging applications such as SAR a continuous distribution of scatterers contribute to the total received signal. This also means that the echoed signals from all scatterers (each echo is delayed by τ_n) within the imaged area contribute to the cross-correlation component. The contribution from all scatterers is accounted for by a coherent addition of the individual echos. The worst case (considering the RAR) would be that all echoed cross-correlation components add up in-phase, which is represented by a sum of amplitudes. The *integrated range ambiguity ratio* ($IRAR$) is then given by the integral

$$IRAR_{u1d2} = \int_{-T_p}^{T_p} \frac{R_{uu}(\tau)}{|R_{u1d2}(\tau - \tau_n)|} \Big|_{\tau=0} d\tau_n = \int_{-T_p}^{T_p} \frac{T_p}{|R_{u1d2}(-\tau)|} d\tau \quad (3.48)$$

which when written in terms of the $RAR(\tau)$ gives

$$IRAR_{u1d2} = \int_{-T_p}^{T_p} RAR_{u1d2}(\tau) d\tau. \quad (3.49)$$

The integrated range ambiguity ratio for different chirp types versus the chirp bandwidth and duration is compared in Fig. 3.14(a) and Fig. 3.14(b),

¹⁰In (2.12) section 2.6 it is shown that $R_{uu}(\tau = 0) = T_p$.

respectively. As expected the $IRAR$ is reduced when the two chirps occupy different frequency bands, as seen by comparing $IRAR_{u1d1}$ to $IRAR_{u1u2}$ and $IRAR_{u1d2}$. Increasing the bandwidth or the duration of the chirps result in approximately the same decrease of integrated range ambiguity ratio, thus both parameters are interchangeable when considering the $IRAR$. In addition, Fig. 3.14 shows that $IRAR_{u1u2} < IRAR_{u1d2} < IRAR_{u1d1}$, hence the most preferable configuration is two chirps with identical chirp rates $k_{e1} = k_{e2}$ but occupying different frequency bands $f_{s1} \neq f_{s2}$.

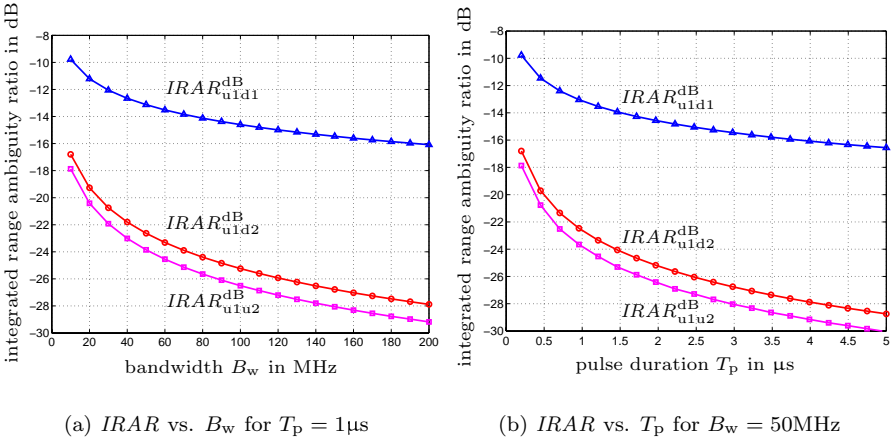


Figure 3.14: Influence of chirp bandwidth B_w and pulse duration T_p on the integrated range ambiguity ratio $IRAR^{dB}$.

The results show that the frequency band, and not the chirp type (i.e., up or down-chirp) is the most important factor determining the $IRAR$ level. A major consequence of this is that it is possible to use an arbitrary high number of chirps all having good cross-correlation level, provided the chirps occupy non-overlapping frequency bands. For p chirps, each of bandwidth B_w the total required bandwidth is $\geq pB_w$. From a practical point of view, the system bandwidth will always be the limiting factor determining the maximum number of chirps. However, changing the frequency band from pulse to pulse may lead to decorrelation of pulses when imaging distributed scatterers. This decorrelation would manifest itself through azimuth defocusing of the image due to the incoherent azimuth compression (also see comments in section 4.5.3).

It is concluded that the integrated range ambiguity ratio $IRAR$ is the quality criterion to be used in imaging radar systems utilizing pulse coded chirp waveforms. The $IRAR$ gives the amount of suppression of the ambiguous range returns. On the other hand, for a required range ambiguity suppression, the $IRAR$ can be used to determine the necessary chirp bandwidth and duration.

3.5 Performance of an Example System

To manifest the results of the last sections an example spaceborne SAR similar to the ASAR instrument on board of the ENVISAT system is considered [129, 37]. The SAR operates in C-band at a center frequency of 5.3 GHz. The geometric ground-range and azimuth resolution are set to $\delta x = 4$ m and $\delta y = 1.5$ m, respectively. A fixed orbit height of $H_{\text{orbit}} = 786$ km results in a platform velocity of 7463 m/s (appendix B.1 gives the relation between the orbit height and the resulting velocity). To calculate the system performance an overall antenna and feed loss of $L_{\text{feed}} = 3$ dB and a receiver noise figure of $NF_{\text{rec}} = 2$ dB are assumed. The mean RF output power of 600 W corresponds to two HPAs as used in RADARSAT-1. The chosen values reflect the very good performance feasible by the DBF hardware setup described in section 2.1. It is assumed that the signal bandwidth is adjusted for varying angle of incidence such that the ground-range resolution is constant across the swath. The system performance is represented by the radiometric resolution of the SAR image given by the $NESZ$ in (3.37) (the expression given in appendix B.2 are used to determine the slant-range R_s for a given local incident angle ϑ_i). The swath width is calculated from the antenna height and (3.42). One possible system design is characterized by the parameters given in Table 3.1.

It is worthwhile to compare the results to those of the ASAR instrument. When operating in the Image Mode and for the angle of incidence given in Table 3.1 the swath of the ASAR instrument ranges from 88–105 km and the $NESZ$ is approximately -20 dB [37]. However the ASAR instrument has a total antenna size of 10×1.4 m with 320 subarrays each connected to a T/R module. The results clearly show that a comparable performance to current in-orbit systems is possible, however with only a small number of Rx subarrays, no T/R modules, and a total antenna size not larger than that of current systems.

Parameter		Value
mean HPA RF output power	P_{av}	600 W
number of receive subarrays	N	4
transmit/receive antenna height	h	0.58 m
transmit antenna length	l_{ts}	3.0 m
receive subarray length	l_{rs}	2.26 m
total receive array length	l_{rx}	9.04 m
angle of incidence	ϑ_i	15°
swath width	X_0	85 km
radiometric resolution	$NESZ$	-22.0 dB
angle of incidence	ϑ_i	25°
swath width	X_0	90 km
radiometric resolution	$NESZ$	-21.2 dB
angle of incidence	ϑ_i	35°
swath width	X_0	100 km
radiometric resolution	$NESZ$	-20.1 dB

Table 3.1: System, hardware and performance parameters of the example DBF SAR system.

4 Processing of Digital Beam-Forming SAR Data and Verification

This chapter describes the processing (reconstruction) for a SAR system having a digital beam-forming (DBF) configuration as described in chapter 2. The analysis of this chapter is based on the general signal model for DBF radar derived earlier, which is brought into the common form known for SAR signal processing [92] in section 4.1. While utilizing the basic reconstruction techniques known from literature [33, 92, 7, 74, 39], the emphasis is on the specialties and the additional processing steps needed for the DBF SAR; this involves the azimuth compression, which is treated in detail in section 4.2. Further, a reconstruction procedure is described in section 4.3 and implemented later in a simulation tool for DBF SAR described in section 4.4. This simulation tool is then used to assess the performance of the reconstruction algorithm (section 4.5.1), for a comparison between DBF and conventional stripmap SAR (section 4.5.2), and to simulate a SAR using pulse coded chirp waveforms in section 4.5.3.

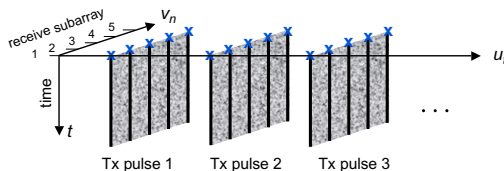


Figure 4.1: Data space of a DBF SAR configuration.

When comparing conventional SAR systems to that of a DBF configuration it is noticed that the dimension of the data space is increased. For conventional SAR the data can be written into a 2D matrix such that each column

corresponds to the temporal samples of the received waveform (the time dependence is given by t) for each position of the radar in the synthetic aperture domain (given by the variable u), successive columns represent successive radar positions. The 3D data space¹ of a DBF SAR is shown in Fig. 4.1, in addition to the data space of the conventional SAR it involves a third dimension (v_n domain) necessary for storing the waveforms of each of the N receive subarrays.

The approach of this chapter is to convert the 3D DBF signal space into an equivalent form such that conventional stripmap processing techniques can be utilized, while at the same time maintaining all the advantages of the DBF configuration. This procedure involves the following steps:

1. a phase shift applied on the received signals which accounts for the phase difference between the mono-static and bi-static configuration;
2. correction for the general case of non-uniform azimuth sampling;
3. mapping the 3D data space into a 2D array to yield a signal equivalent to the uniformly sampled mono-static signal known from stripmap SAR.

4.1 SAR Signal Model

The 2D imaging system in the (x, y) spatial and (k_x, k_y) spatial-frequency domain described earlier in section 3.1 is considered. The x - and y -coordinate are used to identify the range and cross-range domains, respectively. The terrain to be imaged is given by the image function $f(x, y)$ (cf. section 2.2) and its Fourier transform $F(k_x, k_y)$ in the spatial-frequency domain. Without restriction of generality it can be assumed that the radar moves along the y -axis. For a given coordinate of the radar, the imaged area, centered at (X_c, Y_c) is illuminated by the radiation pattern corresponding to the transmit antenna. The echoed signal is simultaneously picked up by N receive subarrays. The synthetic aperture domain (slow-time) variable u is introduced [92] to represent the position of the (moving) radar platform. Thus, the transmit antenna is positioned at $(0, u_t)$ and the position of the receive subarrays, separated by

¹The data space should not be confused with the sensor *geometry* used for data acquisition.

l_{rs} , is given by $(0, u_r)$, where²

$$\begin{aligned} u_r &= u_t + v_n && \text{with} \\ v_n &= n l_{rs} && n = -(N-1)/2, \dots, (N-1)/2 \quad \text{and} \quad n \in \mathbb{Z}. \end{aligned} \quad (4.1)$$

In the following both u and u_t are used to represent the position of the Tx antenna, this is equivalent to setting $u = u_t$. Using the above to express the received signal given in (2.6) section 2.4 in terms of the slow- and fast-time variables u and t , respectively, gives

$$\begin{aligned} s(t, u) &= \int s(t, \mathbf{x}_{ti}, \mathbf{x}_{rj}, \mathbf{x}) f(\mathbf{x}) d\mathbf{x} \\ &= \iint h_t \left(t - \frac{R_{Tx} + R_{Rx}}{c_0} \right) f(x, y) dx dy \end{aligned} \quad (4.2)$$

where the path lengths transmitter–scatterer and scatterer–receiver, respectively, are:

$$R_{Tx} = \sqrt{x^2 + (y - u)^2} \quad (4.3)$$

$$R_{Rx} = \sqrt{x^2 + (y - u - v_n)^2}. \quad (4.4)$$

The analysis starts with the Fourier transformed receive data from (4.2) given by

$$s(f, u) = \mathcal{F}_{(t)}\{s(t, u)\} = H_t(f) \iint f(x, y) \cdot e^{-jk(R_{Tx} + R_{Rx})} dx dy \quad (4.5)$$

where k is the wavenumber $k = 2\pi/\lambda$.

4.2 Algorithm for Azimuth Signal Compression

In the SAR signal domain, the raw data is spread out in the azimuth direction and must be coherently compressed to exploit the full-resolution potential of

²Throughout this chapter it will be assumed that N is an odd integer. All results are also valid for an even number of subarrays. However, a better understanding of the described methods is ensured by the resulting simpler form of the mathematical expressions.

the instrument. Azimuth (cross-range) compression consists of coherently correlating the received signal with the azimuth replica function. The DBF SAR cross-range signal compression involves dealing with the bi-static configuration inherent to DBF systems. In this section an expression is derived for mapping the bi-static signal into an equivalent mono-static form. This way the returns from the DBF configuration “mimic” what would have been obtained by a conventional SAR. Azimuth compression can then proceed as normal [92, 20, 39].

4.2.1 Bi-static to Mono-static Data Mapping

Figure 4.2 shows the geometry both for the bi-static (Tx at $y = u$ and Rx at $y = u + v_n$) and the equivalent mono-static (both Tx and Rx at $y = u + \alpha v_n$) configuration. The aim is to relate the received signal from each of the N subarrays of the bi-static DBF configuration Fig. 4.2(a) to that of an equivalent mono-static configuration Fig. 4.2(b) using appropriate phase correction factors. The conversion is efficiently implemented if these correction factors depend solely on known quantities.

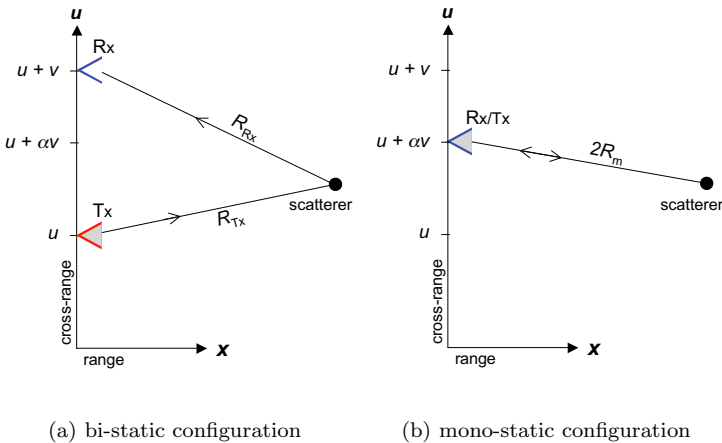


Figure 4.2: Geometry used to map the bi-static (one Tx and one Rx antenna) into an equivalent mono-static (one Tx/Rx antenna) configuration.

The path length R_{Rx} in (4.4) is expanded into a Taylor series [45] around $v_n = 0$ giving

$$\begin{aligned}
 R_{\text{Rx}} = & \sqrt{x^2 + (y - u)^2} - \frac{y - u}{(x^2 + (y - u)^2)^{\frac{1}{2}}} v_n + \frac{x^2}{2(x^2 + (y - u)^2)^{\frac{3}{2}}} v_n^2 \\
 & + \frac{(y - u)x^2}{2(x^2 + (y - u)^2)^{\frac{5}{2}}} v_n^3 + R_4(v_n)
 \end{aligned} \tag{4.6}$$

where $R_4(v_n)$ is the fourth-order remainder term.

The round-trip path length for a mono-static configuration, where both Tx/Rx are positioned at $u + \alpha v_n$ with $0 < \alpha \leq 0.5$ is $2R_m$. It should be mentioned, that the “virtual” position of the mono-static antenna is set through the parameter α , which gives the mono-static configuration an additional degree of freedom³. In contrast to [23, 101] where the position of the phase center and thereby the equivalent mono-static antenna is fixed at $\alpha = 0.5$ the approach used here will set the parameter α so as to yield a uniform azimuth sample separation (see section 4.2.3). Expanding $2R_m$ into a Taylor series around $v_n = 0$ gives:

$$\begin{aligned}
 2R_m = & 2\sqrt{x^2 + (y - u - \alpha v_n)^2} \\
 = & 2\sqrt{x^2 + (y - u)^2} - 2\frac{y - u}{(x^2 + (y - u)^2)^{\frac{1}{2}}} \alpha v_n + \frac{x^2}{(x^2 + (y - u)^2)^{\frac{3}{2}}} (\alpha v_n)^2 \\
 & + \frac{(y - u)x^2}{(x^2 + (y - u)^2)^{\frac{5}{2}}} (\alpha v_n)^3 + R_4(v_n).
 \end{aligned} \tag{4.7}$$

Noting that the first square root term in (4.6) and (4.7) is equal to R_{Tx} as given in (4.3) results in the following approximation for the difference between the mono-static and bi-static round-trip path length

$$\begin{aligned}
 \Delta R = & R_{\text{Tx}} + R_{\text{Rx}} - 2R_m \\
 \approx & -\frac{(y - u)(1 - 2\alpha)}{(x^2 + (y - u)^2)^{\frac{1}{2}}} v_n + \frac{x^2(1 - 2\alpha^2)}{2(x^2 + (y - u)^2)^{\frac{3}{2}}} v_n^2 + \frac{(y - u)x^2(1 - 2\alpha^3)}{2(x^2 + (y - u)^2)^{\frac{5}{2}}} v_n^3.
 \end{aligned} \tag{4.8}$$

³Actually α could be made equal to any real value as long as $\alpha > 0$, but values larger than 0.5 correspond to an under-sampling and will result in an aliased spatial-frequency spectrum.

The above expression is used to replace the bi-static path length in (4.5), i.e., $R_{Tx} + R_{Rx} = 2R_m + \Delta R$, which gives⁴ (the subscript _b is added to denote the *bi-static* case)

$$\begin{aligned}
 s_b(f, u) &= H_t(f) \iint f(x, y) \cdot e^{-jk(2R_m + \Delta R)} dx dy \\
 &= H_t(f) \iint f(x, y) \cdot e^{-j2k\sqrt{x^2 + (y-u-\alpha v_n)^2}} \cdot \\
 &\quad e^{+jk \frac{(y-u)(1-2\alpha)}{(x^2 + (y-u)^2)^{\frac{1}{2}}} v_n} e^{-jk \frac{x^2(1-2\alpha^2)}{2(x^2 + (y-u)^2)^{\frac{3}{2}}} v_n^2} dx dy. \tag{4.9}
 \end{aligned}$$

The first exponential term is the spherical wave common to mono-static SAR systems [91, 92]. The other exponential terms appear due to the bi-static configuration. The second exponential term disappears for $\alpha = 0.5$, i.e., when the phase center is midway between the Tx and Rx antennas. The third exponential term accounts for the phase difference between the mono-static and bi-static configuration, it is non-vanishing, since $\alpha \leq 0.5$. It is straight forward to show that the largest contribution to the phase difference is from the second term. This clearly indicates that $\alpha = 0.5$ is the optimum case resulting in the least phase difference between the mono-static and bi-static configurations.

In [23] a procedure, derived in the spatial domain, is used to arrive at an approximation for the phase correction term, which is a constant independent of the spatial coordinates of the scatterer. This, however, is in contradiction to the expression in (4.9), where both bi-static phase terms depend on the point scatterer's coordinates given by x and y , which makes a bi- to mono-static mapping unfeasible, since the point scatterer's position is a priori unknown and thus cannot be corrected for. A point scatterer dependent phase correction (spatial domain) is derived in [89]; using several approximations, this phase correction is then expressed in the spatial-frequency domain, where it is independent of the point scatterer's position. In the next section, a more efficient (spatial-frequency) mapping procedure is described to for the phase correction.

⁴Only the first and second order terms of v_n are considered here, however it is straight forward to include additional terms.

4.2.2 Phase Correction in the Spatial-Frequency Domain

In the following a procedure is described that maps the bi-static data to an equivalent mono-static form using a phase correction factor which is a function of the measured signals and the known subarrays' positions, instead of the unknown scatterers distribution.

The solution is found when expressing the received signal in the spatial-frequency domain, thus decomposing the spherical phase function in (4.9) into plane waves. Taking the Fourier transform of (4.9) with respect to the variable u within the synthetic aperture length L gives

$$\begin{aligned}
 S_b(f, k_u) &= \mathcal{F}_{(u)}\{s_b(f, u)\} = \int_{-L/2}^{L/2} s_b(f, u) e^{-jk_u u} du \\
 &= H_t(f) \iint f(x, y) \cdot \left[\int_{-L/2}^{L/2} e^{-j2k\sqrt{x^2+(y-u-\alpha v_n)^2}} \right. \\
 &\quad \left. e^{+jk\frac{(y-u)(1-2\alpha)}{(x^2+(y-u)^2)^{\frac{3}{2}}} v_n - jk\frac{x^2(1-2\alpha^2)}{2(x^2+(y-u)^2)^{\frac{3}{2}}} v_n^2} e^{-jk_u u} du \right] dx dy. \quad (4.10)
 \end{aligned}$$

The integral within the brackets can be solved using the method of stationary phase as described in appendix C.1. Neglecting all amplitude and constant terms the resultant expression is:

$$S_b(f, k_u) = H_t(f) \iint f(x, y) \cdot W(u_s) \cdot e^{-j\sqrt{4k^2-k_u^2}x - jk_u(y-\alpha v_n)} dx dy \quad (4.11)$$

furthermore a total of N bi-static signals $S_b(f, k_u)$ are generated, i.e., one for each value of the discrete variable v_n . The expression in (4.11) is identical to what would have been obtained from mono-static SAR, except for the term⁵ $W(u_s)$. In appendix C.2 it is shown that $W(u_s)$ can be approximated by

$$W(u_s) = e^{+jk_u\frac{(1-2\alpha)v}{2}} \cdot e^{-jk\frac{(1-2\alpha^2)v^2}{16x} \left(\frac{4k^2-k_u^2}{k^2}\right)^{\frac{3}{2}}} \quad (4.12)$$

where the dependency on the point scatterer's range x can be neglected in comparison to the other terms. Thus, $W(u_s)$ can be taken out of the integral.

⁵Known from the stationary phase method as the slow varying term.

The bi-static and mono-static signals become

$$S_b(f, k_u) = W(u_s) \cdot H_t(f) \iint f(x, y) \cdot e^{-j\sqrt{4k^2 - k_u^2}x - jk_u(y - \alpha v_n)} dx dy \quad (4.13)$$

$$S_m(f, k_u) = H_t(f) \iint f(x, y) \cdot e^{-j\sqrt{4k^2 - k_u^2}x - jk_u(y - \alpha v_n)} dx dy, \quad (4.14)$$

respectively. The rule for mapping the bi-static configuration into a mono-static configuration becomes obvious, when comparing (4.13) to (4.14), i.e.,

$$S_m(f, k_u) = \frac{S_b(f, k_u)}{W(u_s)}. \quad (4.15)$$

Substituting for $W(u_s)$ (see appendix C.2) gives

$$S_m(f, k_u) = S_b(f, k_u) e^{-jk_u \frac{1}{2}(1-2\alpha)v_n} \cdot e^{+jk_u \frac{1}{16\delta x_c} \left(\frac{4k^2 - k_u^2}{k^2} \right)^{\frac{3}{2}} (1-2\alpha^2)v_n^2}. \quad (4.16)$$

The above expression relates the mono-static and bi-static signals via two *phase correction factors* which are independent of the spatial coordinates of the scatterers. The first phase correction term accounts for the non-uniform azimuth sampling of the DBF signal and vanishes for $\alpha = 0.5$ (similar to the phase term in (4.9)). The second complex exponential term corrects the additional phase deviation, due to the bi-static configuration, this correction term is frequency dependent through the wavenumber k . Both the correction factors and the signals are represented in the spatial-frequency k_u -domain and thus require a Fourier transformation of the signal from each subarray.

The effect of the phase correction for an X-band DBF SAR system with $N = 5$ subarrays is shown in Fig. 4.3. The plot shows the difference between the phase of the bi-static signal and the ideal mono-static signal for four of the five subarrays; no correction is applied to the signal received from the center subarray, since it operates in the mono-static mode. The geometry is such that the first phase correction term is dominant as compared to the second. It is evident that, within the spatial-frequency support band of the point scatterer, the phase difference vanishes after the correction. The relevance of the phase correction is concluded from the fact, that the uncorrected signal's

phase slope is different for each subarray. This is equivalent to stating that the phase correction term depends on the subarray's position. Neglecting the phase correction would result in a distorted spectrum, since the signals from all subarrays, each one having a different phase deviation, contribute to the final signal spectrum.

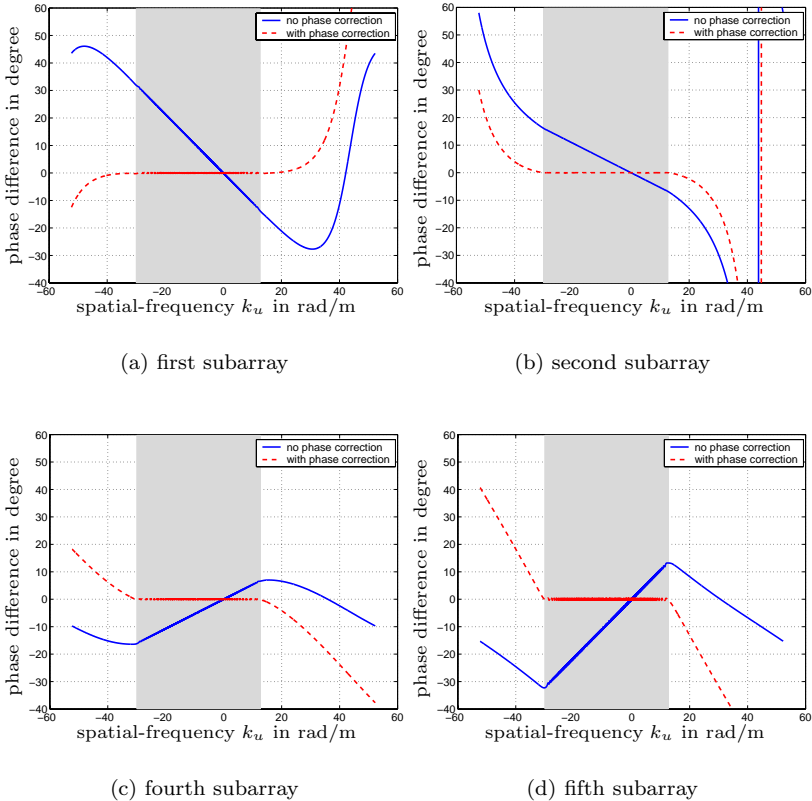


Figure 4.3: Phase correction of bi-static signal for a DBF SAR with 5 subarrays and $\alpha = 0.36$. The $200 \times 200 \text{ m}^2$ imaged area contains one point scatterer at $(x_n, y_n) = (80 \text{ m}, -90 \text{ m})$. The spatial-frequency support band of the point scatterer is shaded.

4.2.3 Uniform Cross-Range Sampling

In DBF SAR configurations two cross-range sample spacings exist (see Fig. 4.4). The first, Δu_r is fixed and given by the length of the receive subarrays; for each transmitted pulse, N spatial samples separated by $\Delta u_r = l_{rs}/2$ are acquired. The second, Δu_t is given by the ratio of the platform velocity V and the *PRF*; the separation between each group of N samples is given by Δu_t . In general the resultant sampling of the interleaved dataset is non-uniform (unless the condition (3.22) in section 3.1.3 is fulfilled). For a real airborne or spaceborne SAR system it is unrealistic to assume, that the *PRF* and velocity are adjustable so as to permanently give the exact value required for Δu_t to yield a uniform sampling. As a consequence difficulties are encountered when using mathematical operations, such as the fast Fourier transform to process the data. In the following, a procedure is described, which adapts the phase correction factor derived in the previous section so as to yield an effective uniform sampling.

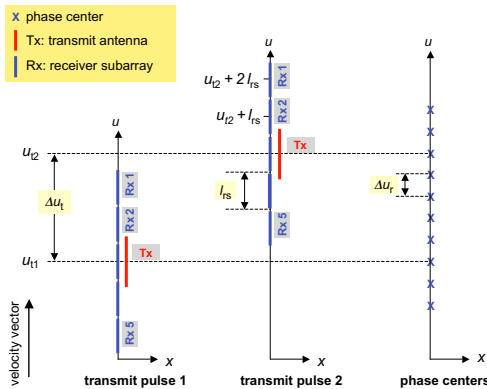


Figure 4.4: The two sampling separations and the positions of phase centers for uniform sampling.

The relation between the bi-static and mono-static signals given in (4.16) includes the parameter α , where $u + \alpha v_n$ is the position of the equivalent mono-static antenna (phase center). This parameter can be adjusted to yield a uniform spacing of the phase centers in the synthetic aperture domain. For the bi-static configuration shown in Fig. 4.4 the transmit antenna is positioned at

u_t while the receive subarrays are located at discrete positions given by $u_t + v_n$ where v_n is defined in (4.1). The separation Δu_t is related to the *PRF* and the platform velocity via (3.22)

$$\Delta u_t = \frac{V}{PRF}. \quad (4.17)$$

For two successive pulses transmitted at u_{t1} and u_{t2} , respectively, a total of $N + 1$ samples exist within the interval $[u_{t1}, u_{t2}]$. A uniform sampling requires equal separation between any two neighboring phase centers. This separation is then given by

$$\Delta u_r = \frac{\Delta u_t}{N}. \quad (4.18)$$

Requiring the above to be true for the phase centers of two arbitrary neighboring subarrays $n + 1$ and n , i.e.,

$$\Delta u_r = (u_t + \alpha v_{n+1}) - (u_t + \alpha v_n) = (n + 1)\alpha l_{rs} - (n)\alpha l_{rs} \stackrel{!}{=} \frac{\Delta u_t}{N} \quad (4.19)$$

results in

$$\alpha = \frac{\Delta u_t}{N l_{rs}} = \frac{V}{N l_{rs} \cdot PRF} \quad (4.20)$$

which reduces to the expression given in (3.21) for $\alpha = 0.5$. The above expression is used to obtain the value of α when the ratio V/PRF is not equal to that given by (3.22).

It is interesting to note that the optimum value of α (i.e., $\alpha = 0.5$ see discussion in section 4.2.1) can be ensured for different ratios of V/PRF by changing the number of *active* subarrays. This gives the opportunity to adapt the processing to a changing carrier velocity or *PRF*. To show this, assume that $\alpha_N = 0.5$ for N active subarrays⁶ when $PRF = PRF_0$ and $V = V_0$. Then (4.20) is written as

$$\alpha_N = \frac{1}{2} \frac{PRF_0}{V_0} \cdot \frac{V}{PRF}. \quad (4.21)$$

Similarly the value of α_{N-2} , i.e., when the data of the two outermost subarrays is disregarded can be written as

$$\alpha_{N-2} = \frac{1}{2} \frac{PRF_0}{V_0} \cdot \frac{V}{PRF} \frac{N}{N-2}. \quad (4.22)$$

⁶The subscript N was added to relate the parameter α to the number of active (i.e., used) subarrays.

Setting $\alpha_{N-2} = 0.5$ in the above expression and inserting the resultant V/PRF into (4.21) gives the value of α_N at the transition point, i.e., when changing from N to $N - 2$ subarrays:

$$\alpha_N \Big|_{\alpha_{N-2}=0.5} = \frac{1}{2} \frac{N-2}{N} \quad (4.23)$$

the above equation gives the minimum value of α for N active subarrays.

Reducing the number of active subarrays is an attractive way to compensate for an increasing PRF or a reduced platform velocity V , while keeping the parameter α as close as possible to the optimum value $\alpha = 0.5$. Fig. 4.5 shows the variation of α_{opt} as a function of the ratio $(V/PRF)/(V_0/PRF_0)$ when the number of subarrays is set, so as to minimize the difference $|0.5 - \alpha|$, while keeping $\alpha \leq 0.5$ to avoid an aliased spatial-frequency spectrum. In accordance with (4.23) the plot of α_{opt} shows that a large number of subarrays is preferable, since this ensures that α_{opt} is closer to 0.5.

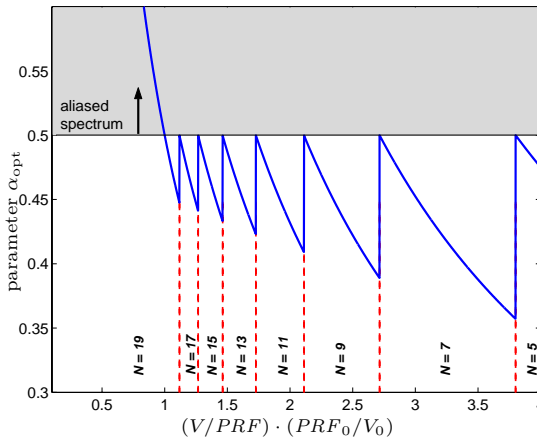


Figure 4.5: The value of α_{opt} as a function of V/PRF normalized to V_0/PRF_0 . The vertical lines indicate transition points where the number of active subarrays N is changed, the maximum number of subarrays is $N = 19$.

4.2.4 Concatenation

In order to use conventional stripmap reconstruction algorithms on the DBF SAR data, it is required to map the bi-static 3D data space into an equivalent 2D mono-static data space. This involves two steps:

- correcting the phase of the bi-static data;
- appropriate concatenation (i.e., interleaving) of the bi-static data.

Using the expression in (4.16) would just account for correcting the phase difference between the mono-static and bi-static data, but gives no information on the procedure to be used for the concatenation. An intuitive approach, indicated in Fig. 4.6, concatenates by ordering the azimuth samples such that $u = u_t + v_n/2$ is strictly monotonic increasing. Thus, for each position of the transmitter the data is ordered with increasing subarray position. This section describes a method, which combines the above two steps of phase correction and concatenation.

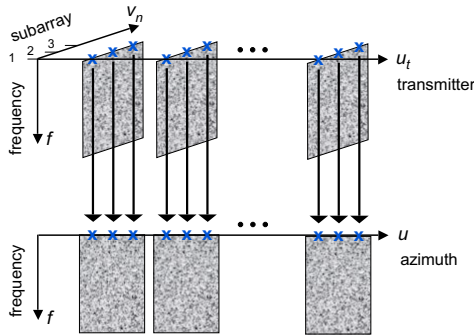


Figure 4.6: 3D to 2D data concatenation.

4.2.4.1 Conventional FFT Kernel

When mapping the bi-static data, it needs to be taken into account that the phase correction has to be performed in the spatial-frequency k_u -domain, while the concatenation is in the spatial u -domain. A straight forward algorithm is

shown in Fig. 4.7, where $\text{FFT}_{(u)}$ and $\text{IFFT}_{(k_u)}$ represent the Fourier transform and inverse Fourier transform with respect to the variables u and k_u , respectively. The azimuth samples from each subarray are transformed into the k_u -domain, then the phase correction according to (4.16) is applied. The IFFT operations are necessary to transform the phase corrected data back into the u -domain for concatenation. The final FFT is necessary to proceed processing with the *mono-static* (i.e., conventional stripmap) equivalent data.

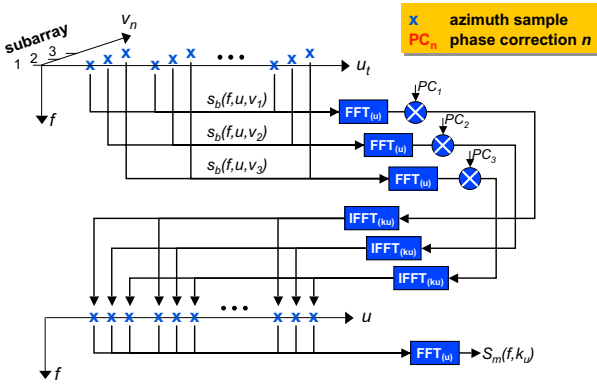


Figure 4.7: Phase correction and concatenation of the DBF SAR Data with $N = 3$ using conventional FFT.

The above mentioned approach has the following disadvantages:

1. Since the azimuth pulse-to-pulse separation of each subarray is Δu_t (see section 3.1.3.2) the azimuth spectrum after the $\text{FFT}_{(u)}$ on the individual subarrays will be aliased and any phase correction (computed in the k_u -domain) will contain aliasing errors.
2. The phase correction and subsequent concatenation are at a relatively high computational cost. A total of $2N$ FFTs each of length N_{az} and one additional FFT on the concatenated data of length $N \cdot N_{\text{az}}$ are required for the calculations.

4.2.4.2 Modified FFT Kernel

An elegant algorithm overcoming the before mentioned disadvantages is obtained by combining the phase correction and concatenation within the kernel of the discrete Fourier transform (DFT) [77]. This is achieved by changing the DFT kernel such that each DFT is computed as a superposition of lower order DFTs, where each DFT corresponds to the sampled signals from each receiving subarray. This approach is stated in [15] for reducing the memory and time requirements necessary for FFT and IFFT operations⁷. A similar interpretation of the modified kernel is used in [40] to process SAR data. However, both in [15] and [40] the dimension of the original data has to be increased in order to apply the method, i.e., a 1D DFT code is converted into a 2D DFT code, whereas for the DBF SAR case it is a useful method which can be applied directly on the 3D data.

In the following the modification of the FFT kernel will be derived. Starting point is a general expression of the 1D Fourier transform of the function $s(f, u)$ defined as [38]

$$S(f, k_u) = \mathcal{F}_{(u)}\{s(f, u)\} = \int_{-\infty}^{\infty} s(f, u) e^{-jk_u u} du. \quad (4.24)$$

The frequency variable f is not considered further, since the Fourier transform is with respect to the variable u . Also the subscript u is dropped here to avoid confusion. The equivalent discrete form of the above Fourier transform applied on a discrete dataset $s(p)$ with $p = 0, 1, \dots, P-1$ is defined by

$$S(n) = \sum_{p=0}^{P-1} s(p) e^{-j \frac{2\pi}{P} pn} \quad (4.25)$$

where $S(n)$ is the discrete equivalent of the continuous signal $S(k_u)$. If FFT codes are to be used for implementing the DFT, then it is preferable to have the same number of samples for $s(p)$ and $S(n)$, which requires $n = 0, 1, \dots, P-1$.

Now factor P into two integers, such that $P = N_{az} \cdot N$ and split the input

⁷Although the definition of the DFT is used for deriving the modified kernel, however it is assumed that the implementation involves the more efficient FFT.

and output vectors into 2D arrays:

$$s(p) \rightarrow s(q, l) \quad , \quad p = N \cdot l + q$$

with $l = 0, 1, \dots, N_{\text{az}} - 1$; $q = 0, 1, \dots, N - 1$ (4.26)

and

$$S(n) \rightarrow S(m, i) \quad , \quad n = N_{\text{az}} \cdot m + i$$

with $m = 0, 1, \dots, N - 1$; $i = 0, 1, \dots, N_{\text{az}} - 1$ (4.27)

substituting (4.26) and (4.27) into (4.25) and rearranging

$$S(N_{\text{az}} \cdot m + i) = \sum_{q=0}^{N-1} e^{-j \frac{2\pi}{N \cdot N_{\text{az}}} (N_{\text{az}} \cdot qm + qi)} \sum_{l=0}^{N_{\text{az}}-1} s(q, l) e^{-j \frac{2\pi}{N_{\text{az}}} (N_{\text{az}} \cdot lm + li)} \quad (4.28)$$

knowing that $\exp(-j2\pi lm) \equiv 1$ simplifies the above to

$$S(N_{\text{az}} \cdot m + i) = \sum_{q=0}^{N-1} e^{-j \frac{2\pi}{N} qm} \left[e^{-j \frac{2\pi}{N \cdot N_{\text{az}}} qi} \sum_{l=0}^{N_{\text{az}}-1} s(q, l) e^{-j \frac{2\pi}{N_{\text{az}}} li} \right]. \quad (4.29)$$

The inner summation is immediately recognized as an N_{az} -point DFT of $s(q, l)$ with respect to l . The exponential term within the brackets corresponds to a phase shift, and the outer summation is the N -point DFT of the term inside the brackets with respect to the variable q . Because the phase shift depends upon i it may only be applied after the N_{az} -point DFT; because it depends on q it may only be applied before the N -point DFT.

To interpret (4.29) in terms of the DBF SAR signal it is rewritten in terms of a low-order DFT:

$$S_q(i) = e^{-j \frac{2\pi}{N \cdot N_{\text{az}}} qi} \underbrace{\sum_{l=0}^{N_{\text{az}}-1} s(N \cdot l + q) e^{-j \frac{2\pi}{N_{\text{az}}} li}}_{\text{DFT}_{(l)}\{s(q, l)\}} \quad (4.30)$$

and a high-order DFT:

$$S(n) = S(N_{\text{az}} \cdot m + i) = \underbrace{\sum_{q=0}^{N-1} S_q(i) e^{-j \frac{2\pi}{N} qm}}_{\text{DFT}_{(q)}\{S_q(i)\}}. \quad (4.31)$$

The discrete variables q and l are now understood as representing the Rx subarray and Tx antenna positions v_n and u_t , respectively. This way $s(q, l)$ can be considered as discrete samples of subarray q when the array is positioned at l . The variable u is bounded by the length of the synthetic aperture, i.e., $-L/2 \leq u \leq L/2$ within this interval N_{az} samples are taken by each subarray. For each transmitted pulse the received signal is sampled by N subarrays, which gives a total of $N \cdot N_{\text{az}}$ spatial samples (cf. section 3.3.1). The N_{az} samples of each of the N subarray are combined through the DFTs into a 1D vector $S(n)$ equivalent to the signal $S(f, k_u)$ as given by (4.13).

For a fixed q the vector $s(n \cdot l + q)$ represents the samples of one subarray along the synthetic aperture domain l . Thus the DFT in (4.30) is equivalent to the Fourier integral in (4.10) where the subarray's position is considered as a fixed parameter v_n . From (4.16) it is evident that the phase correction factor, which, similar to the phase shift in (4.30) has the subarray v_n as a parameter, needs to be applied after the low-order $\text{DFT}_{(l)}$. The high-order $\text{DFT}_{(q)}$ in (4.31) combines the individual low-order DFTs into the final vector which is the discrete form of the continuous Fourier transformation with respect to u . Since the high-order $\text{DFT}_{(q)}$ is with respect to the subarray parameter q , the phase correction has to be applied before this DFT.

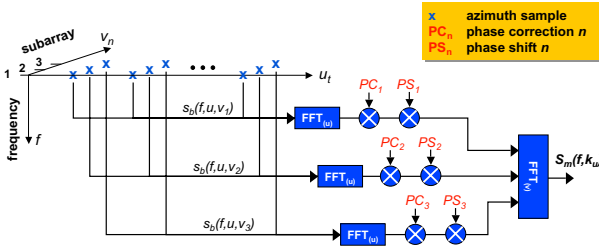


Figure 4.8: Phase correction and concatenation of the DBF SAR Data with $N = 3$ using modified FFT.

Figure 4.8 shows the procedure for computing the DFT according to (4.29). The Fast Fourier Transform (FFT) is used to compute the individual DFTs. Compared to the former method, which uses a conventional FFT kernel this algorithm has the following advantages:

1. The phase correction and the concatenation are combined within the FFT kernel. This Fourier transformation is inherent to SAR image formation, thus nearly no additional processing power is required.
2. The computational cost and memory requirement are reduced. A total of N FFTs each of length N_{az} and N_{az} FFTs each of length N are required.
3. The sample separation of the data for the $\text{FFT}_{(l)}$ and $\text{FFT}_{(v)}$ are Δu_t and Δu_r , respectively. In both cases the data is uniformly sampled.

4.3 Image Reconstruction

The aim of SAR image reconstruction is to determine the image function $f(x, y)$ based on the measured signals. At this point the available signal is the phase corrected, concatenated, mono-static equivalent signal in the spatial-frequency domain given by (4.14) and (4.15). With the following substitutions

$$k_x = \sqrt{4k^2 - k_u^2} \tag{4.32}$$

$$k_y = k_u \tag{4.33}$$

the signal is rewritten as

$$S_m(f, k_u) = H_t(f) \iint f(x, y) e^{-jk_x x - jk_y y'} dx dy' \tag{4.34}$$

where $y' = y - \alpha v_n$ and $dy' = dy$. The above integral is immediately recognized as the Fourier integral of $f(x, y)$ with respect to the spatial variables x and y' , thus

$$S_m(f, k_u) = H_t(f) \cdot F(k_x, k_y) \tag{4.35}$$

with

$$F(k_x, k_y) = \mathcal{F}_{(x,y)}\{f(x, y)\}. \tag{4.36}$$

Several procedures exist for obtaining the image function from the measured SAR data. The method implemented here is the 2D Fourier matched filtering and spatial-frequency interpolation detailed in [92]. The image reconstruction mainly involves a baseband conversion via the slow-time reference function $S_o(k_x) = \exp(jk_x X_c)$ and interpolation in the spatial-frequency domain

(k_x, k_y) , followed by a 2D inverse Fourier transform:

$$f(x, y) = \mathcal{F}_{(x,y)}^{-1}\{S_o^*(k_x) \cdot H_t(f)F(k_x, k_y)\}. \quad (4.37)$$

Since the emphasis is on evaluating the principal performance of the suggested DBF SAR processing techniques and to compare these with conventional SAR systems, it is not desirable to include procedures such as secondary range compression, chirp scaling or motion compensation [20, 56, 74, 92] in the following reconstruction.

4.4 Simulator for Digital Beam-Forming SAR

Figure 4.9 shows a block diagram for the processing of DBF SAR data. The signal received from each subarray (see [1] in Fig. 4.9) is converted into the base-band (BB) and then range compressed in the frequency domain [2]. The range compression (see section 2.6) is identical to the stripmap SAR, except, that for the DBF case a parallel N -channel range compression is performed, i.e., one channel for each subarray. In [3] the low-order FFT and the phase correction are implemented, thus transforming the bi-static DBF data into the equivalent mono-static form; the resultant signal corresponds to $S_q(i)$ in (4.30). The 3D data is then mapped into a 2D data array by the high-order FFT in [4]. The output of this FFT, given by $S(n)$ in (4.31), is in the 2D form common to stripmap SAR. After the mapping a single, high data rate channel remains. Finally, azimuth compression involving matched filtering and interpolation in the spatial-frequency domain is performed and SAR image is obtained after a 2D inverse-FFT [5].

The following differences are noted when comparing DBF SAR to conventional stripmap processing:

1. Multi-channel processing is required since the received signal from each subarray is range compressed;
2. Two additional processing blocks are added for phase correction and 3D to 2D data space mapping; and
3. The spatial domain interpolation and azimuth compression is identical to the respective stripmap case, but the data rate in the DBF case is higher.

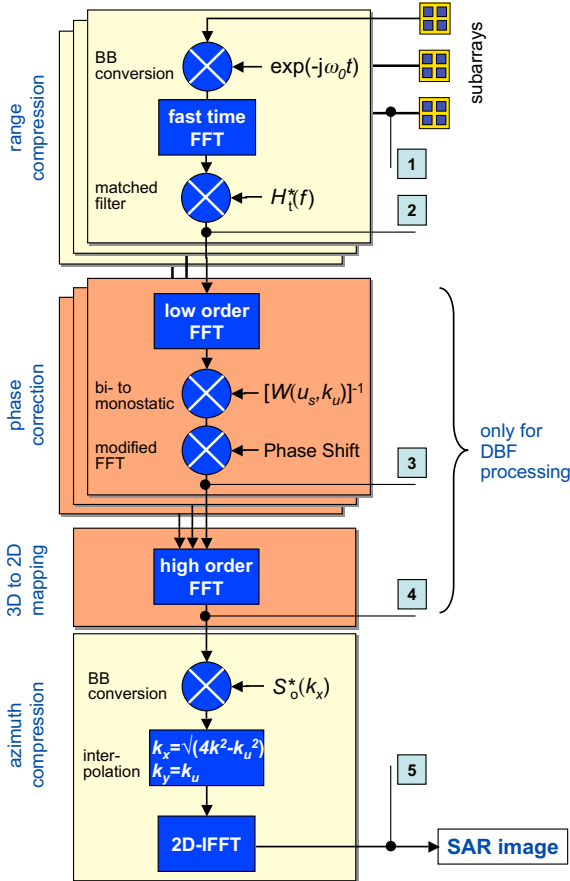


Figure 4.9: Block diagram of the DBF SAR image reconstruction simulator.

The procedure is illustrated for an exemplary system. It operates at 9.6 GHz and uses $N = 5$ subarrays to image an area of $84 \times 84 \text{ m}^2$ at a range of $X_c = 4 \text{ km}$ with 8 point scatterers positioned on the ground. Simulated output signals at the positions indicated by the numbers within the boxes in Fig. 4.9 are shown separately in Figs. 4.10 to 4.12. Figures 4.10(a) and 4.10(b) show the raw SAR input signal, and the signal after range compression, respectively, for one of

the parallel channels. The magnitude of the signals are nearly identical for all channels, however the bi-static configuration results in different phases of the signals.

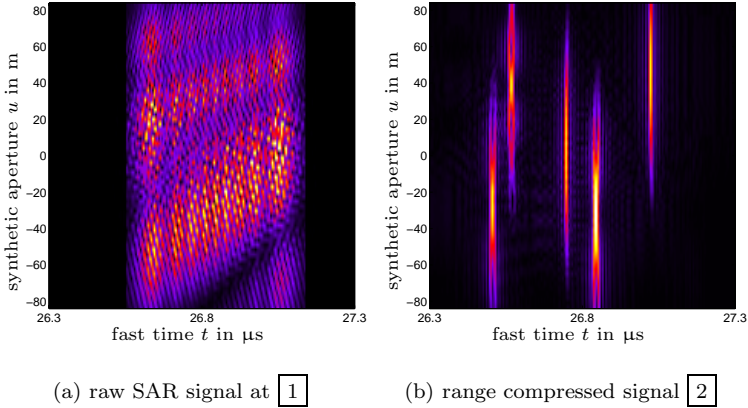


Figure 4.10: Simulated SAR signal of one of the DBF channels.

Figure 4.11 illustrates the processing steps exclusive to DBF SAR. As expected the signal in Fig. 4.11(a) obtained after the low-order FFT is aliased as seen by the extent of the azimuth spectrum along the k_u axis. This is due to the fact that the signals obtained by each subarray represent an undersampled azimuth spectrum. It is only when the signals from all subarrays, i.e., channels are combined through the high-order FFT that the resulting azimuth spectrum will not be aliased. This resultant spectrum is shown in Fig. 4.11(b).

The reconstructed SAR image after the interpolation and the 2D IFFT is shown in Fig. 4.12(a) together with the original scatterer distribution in the imaged area Fig. 4.12(b). It should be noted that the two point scatterers in the lower right quadrant are separated by the azimuth distance δy_{DBF} corresponding to the theoretical azimuth resolution of the DBF configuration (see section 3.1.6).

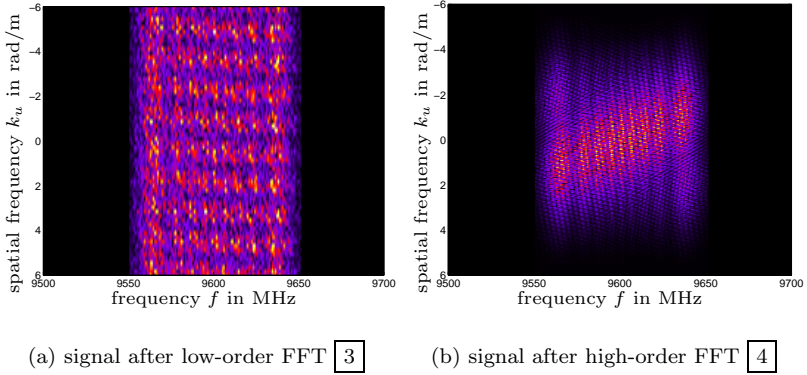


Figure 4.11: Simulated DBF SAR signal before and after concatenation.

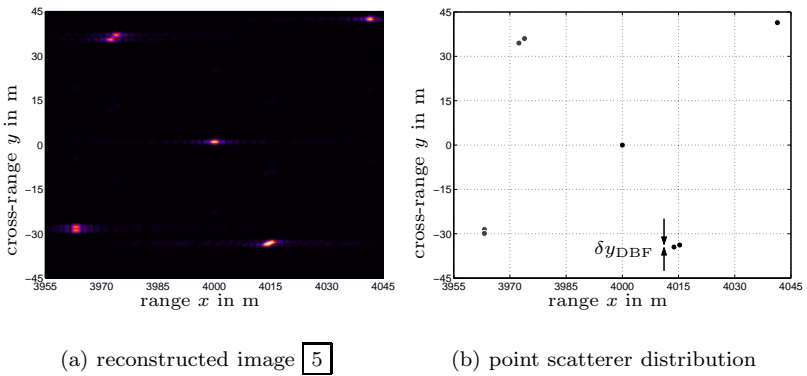


Figure 4.12: Reconstructed DBF SAR image and the original positions of the point scatterers.

4.5 Verification

This section uses the simulation tool described in the previous section to verify the DBF SAR processing algorithm. In addition the simulator is used to confirm the results derived in chapter 3 by comparing a DBF to a conventional stripmap SAR system. Further, imaging by using pulse coded chirp waveform is demonstrated.

4.5.1 Point Spread Function

A common function used to characterize the performance of SAR systems is the point spread function (PSF). Several image quality parameters such as azimuth and range resolution or side-lobe level can be extracted from the PSF. The PSF is the 2D processed image of a normalized, i.e., $\sigma_0 = 1 \text{ m}^2$, point scatterer [74]. The simulated PSF exclude any noise contribution. In addition, no weighting is introduced on the reference function, since the prime intention at this point is to compare the PSF for various DBF system parameters settings. Weighting or windowing functions are used in practice to reduce the side-lobe level while sacrificing resolution. Various windowing functions are given in [47].

Figure 4.13 shows the simulated PSFs for different numbers of subarrays and values of the parameter α of an X-band SAR. The point target is located at the center of the imaged area $(x_n, y_n) = (0, 0)$. The chirp bandwidth is fixed at $B_w = 120 \text{ MHz}$, which results in identical range profile for all PSFs. Comparing Fig. 4.13(a) to Fig. 4.13(b) shows the effect of increasing the number of subarrays. The main effect is an increased azimuth resolution from $\delta y = 0.49 \text{ m}$ to $\delta y = 0.41 \text{ m}$, manifested through a decreased main peak width. The reason is that increasing N results in subarrays of smaller length and thus an increased synthetic aperture length L as detailed in section 3.1.6. The influence of the parameter α can be seen by comparing Fig. 4.13(b) to Fig. 4.13(d), which shows an increase in the side-lobe level. Basically the phase correction is represented by the exponential terms in (4.9), however the implementation is in the spatial-frequency domain including all the approximations inherent to the calculation of spatial-frequency phase correction factor (4.16), which is the reason for the increased side-lobe level. Increasing the number of subarrays while keeping α constant and $\alpha \neq 0.5$ will also result in an increased cross-

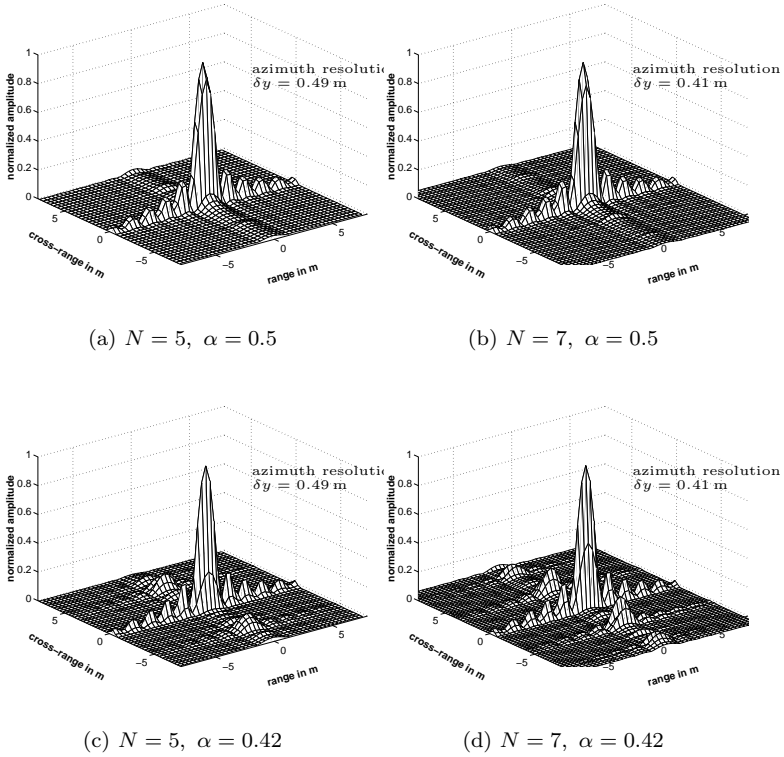


Figure 4.13: Point spread function (PSF) of X-band DBF SAR system imaging an area of $16 \times 16 \text{ m}^2$ at a range of $X_c = 500 \text{ m}$. The bandwidth is fixed at $B_w = 120 \text{ MHz}$.

range side-lobe level. This effect can be seen when comparing Fig. 4.13(c) to Fig. 4.13(d). In addition to the reasons mentioned above, this increase is justified by the fact that increasing N will result in larger receive arrays, i.e., higher values of v_n and consequently larger error due to the finite Taylor series expansion in (4.6) and (4.7).

4.5.2 Comparison to Stripmap SAR

In this section the performance of the DBF SAR system is compared to that of a conventional stripmap SAR. The dimension of the antennas of both systems are chosen such that the size of the imaged area is the same. In addition an identical distribution of point scatterers is used in both simulations, thus both systems “view” identical ground segments. The parameters used in the simulation are given in Table 4.1, which shows that the bandwidth is fixed for both system. Both DBF SAR and stripmap SAR images are obtained through the same basic reconstruction algorithm described earlier, with the additional steps included for the DBF SAR.

Parameter		Value
Common Parameters:		
center frequency	f_c	9.6 GHz
bandwidth	B_w	100 MHz
Tx/Rx antenna heights	h	0.58 m
imaged area	$X_0 \times Y_0$	$84 \times 84 \text{ m}^2$
center range	X_c	3 km
Stripmap SAR System:		
antenna length	l_{strip}	6.00 m
DBF SAR System:		
sampling parameter	α	0.45
number of Rx subarrays	N	5
Tx antenna length	l_{ts}	3.0 m
Rx subarray length	l_{rs}	2.26 m

Table 4.1: Simulation parameters of the DBF and stripmap SAR systems.

The reconstructed images of the DBF and stripmap SAR systems are shown in Fig. 4.14 and Fig. 4.15, respectively. The DBF system shows a higher azimuth (cross-range) resolution. As a result, distinct point scatterer constellations falling within the same range gate but separated in cross-range can still be distinguished in the DBF image, while being smeared in the stripmap image. Since both systems operate at the same bandwidth the resultant range resolution is identical in both images.

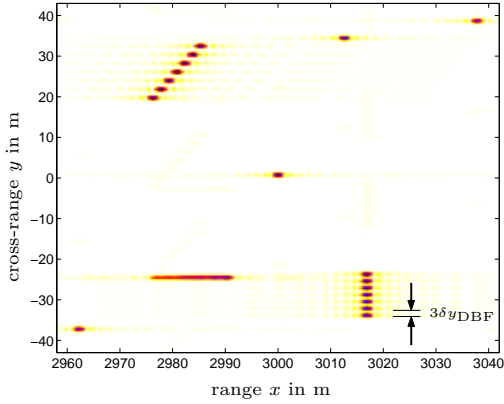


Figure 4.14: Reconstructed image for the DBF SAR system of Table 4.1.

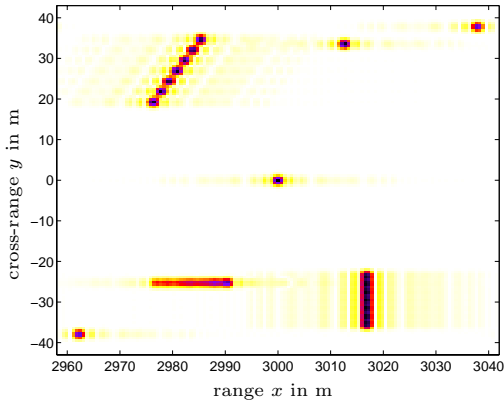


Figure 4.15: Reconstructed image for the stripmap SAR system of Table 4.1.

4.5.3 Pulse Coded Chirp Waveform SAR

Pulse coded chirp waveform techniques allow a substantial increase in the performance of synthetic aperture radar as described in section 3.4. To demonstrate this, the SAR simulation tool is adapted to dual chirp operation [93] and used to process the example scenarios in Fig. 4.16(a). The radar operates at a center frequency of 9.6 GHz with a chirp bandwidth of 100 MHz. The imaged area of $100 \times 100 \text{ m}^2$ is centered at $X_c = 3000 \text{ m}$. The PRF is kept constant at 3 MHz for all simulations⁸.

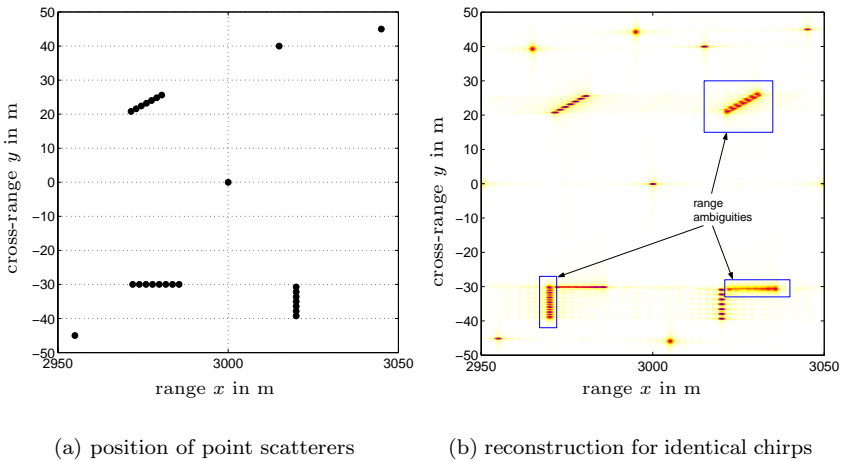


Figure 4.16: Simulation scenario and the resultant reconstructed image when using two up-chirps occupying the same bandwidth.

To manifest the effect of range ambiguities, first a single chirp SAR system is simulated. The processed image in Fig. 4.16(b) shows each point scatterer at two range positions. From the image it is not possible to distinguish the *real* (see Fig. 4.16(a)) from the ambiguous (ghost) point scatterers. The reason is that a PRF of 3 MHz results in an unambiguous range of 50 m, while the simulated swath width of 100 m is twice this value.

Next two inverse, i.e., up and down-chirps occupying the same bandwidth

⁸The extremely high PRF is possible due to the small extent of the imaged area

are used. The range compression matched filter is adapted to account for the inverse chirp rates. The resulting image in Fig. 4.17(a) shows that the range ambiguities are suppressed. However, a blurred spot appears at the previous positions of the ghost scatterers. This is basically due to the poor value of the cross-correlation, which appears smeared in range direction over the image.

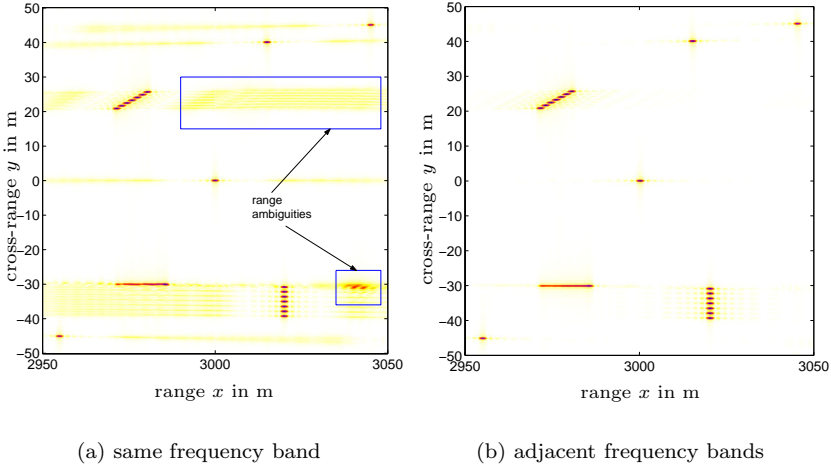


Figure 4.17: Reconstructed image when using inverse chirps to suppress range ambiguities.

An additional suppression of range ambiguities is possible by using two chirps occupying adjacent frequency bands. The chirp bandwidths and durations are unchanged with respect to the previous examples. In addition to handling two chirp rates, the processing algorithm must now be capable of handling the different frequency bands of the chirps. The reconstructed image in Fig. 4.17(b) shows a good suppression of the range ambiguities.

The above simulations confirm the theoretical results derived earlier for a distribution of point scatterers (permanent scatterers within a terrain). The effect of azimuth decorrelation due to the different frequency bands is not included in the simulation tool and needs to be further investigated by simulations with real SAR data.

5 Multi-Transmit/Receive Real Aperture Radar

For several imaging applications it is crucial to monitor the sectors in front and behind the radar platform. Examples are navigation, detection of illicit oil discharges and most military and law enforcement applications. As detailed in chapter 2 imaging radar exploiting a synthetic aperture is not suitable for such applications. In order to fill these visualization gaps and complete the existing imaging range of remote sensing radars, an antenna configuration is investigated which facilitates imaging either as top view (mapping mode) or as forward/backward view. To achieve a geometric resolution perpendicular to the flight path an antenna array, i.e., a *real* aperture is used. In principle a real aperture radar does not require a platform movement for imaging. To date, forward/backward imaging radars have been reported for example in [69, 63, 65, 96] for uniform arrays and a single transmit antenna; radars with two or more transmit antennas are given in [11, 54, 27, 1, 114]. A thorough spatial-frequency domain treatment of uniform multi-dimensional transmit/receive antenna arrays is found in [51]. In practice, the carrier platform (e.g., airplane) neither permits the placement of an arbitrary high number of elements (subarrays) nor can the positions of these subarrays be chosen freely. The processing algorithm developed in this work is adapted to handle an imposed number and position of subarrays. On the other hand, several performance parameters (e.g., resolution, coverage and unambiguous angular segment) need to be defined in order to use the available degrees of freedom most efficiently.

The radar is assumed to be operated in the digital beam-forming configuration explained earlier in section 2.1. The geometry investigated in section 5.1 is a special case derived from the general geometry of section 2.2. Starting point for the angular compression algorithm developed in section 5.2 is the

raw data signal (c.f. section 2.4) after range compression (c.f. section 2.6). This, for the first time, includes a comprehensive mathematical treatment for real aperture imaging radar using multiple transmit antennas. Depending on the antenna configuration and the imaged area an additional near field correction could become necessary, which is investigated in detail in section 5.3. In addition, the antenna placement should be such as to prevent angular ambiguities; section 5.4 gives a novel investigation of this issue for non-uniform element placement. The operation and advantage from utilizing pulse coded chirp waveforms is described in section 5.5. In order to understand the basic parameter dependencies, the special case of a uniform linear array is treated in section 5.6, which results in compact expressions for the compressed signal, where the influence of system parameters can directly be related to the performance. Finally a MATLAB[®] based simulator is presented in section 5.7 which implements the described reconstruction algorithm. Example scenarios are input to the simulation tool in order to verify the analytical results obtained in this chapter.

5.1 Basic Geometry

In the following the basic geometry is reviewed in order to obtain expressions for the path lengths used later when deriving the signal model. Figure 5.1 shows the antenna configuration, which consists of M transmit and N receive subarrays.

Consider the distance transmitter–scatterer and scatterer–receiver. Expressing the positions of the Tx and Rx subarrays in Cartesian coordinates by $\mathbf{x}_t = x_t \hat{\mathbf{e}}_x + y_t \hat{\mathbf{e}}_y + z_t \hat{\mathbf{e}}_z$ and $\mathbf{x}_r = x_r \hat{\mathbf{e}}_x + y_r \hat{\mathbf{e}}_y + z_r \hat{\mathbf{e}}_z$, respectively; and the point \mathbf{x}_n in spherical coordinates

$$\begin{aligned}x_n &= r_n \sin \vartheta_n \cos \psi_n \\y_n &= r_n \sin \vartheta_n \sin \psi_n \\z_n &= r_n \cos \vartheta_n.\end{aligned}\tag{5.1}$$

the round-trip path length to a point scatterer at (x_n, y_n, z_n) is given by the

sum of the distances

$$\begin{aligned}
 R_{Tx}^2 &= (x_n - x_t)^2 + (y_n - y_t)^2 + (z_n - z_t)^2 \\
 &= r_n^2 \sin^2 \vartheta_n \cos^2 \psi_n - 2x_t r_n \sin \vartheta_n \cos \psi_n + x_t^2 \\
 &\quad + r_n^2 \sin^2 \vartheta_n \sin^2 \psi_n - 2y_t r_n \sin \vartheta_n \sin \psi_n + y_t^2 \\
 &\quad + r_n^2 \cos^2 \vartheta_n - 2z_t r_n \cos \vartheta_n + z_t^2 \\
 &= r_n^2 - 2x_t r_n \sin \vartheta_n \cos \psi_n - 2y_t r_n \sin \vartheta_n \sin \psi_n - 2z_t r_n \cos \vartheta_n \\
 &\quad + x_t^2 + y_t^2 + z_t^2
 \end{aligned} \tag{5.2}$$

and

$$\begin{aligned}
 R_{Rx}^2 &= (x_n - x_r)^2 + (y_n - y_r)^2 + (z_n - z_r)^2 \\
 &= r_n^2 - 2x_r r_n \sin \vartheta_n \cos \psi_n - 2y_r r_n \sin \vartheta_n \sin \psi_n - 2z_r r_n \cos \vartheta_n \\
 &\quad + x_r^2 + y_r^2 + z_r^2
 \end{aligned} \tag{5.3}$$

respectively.

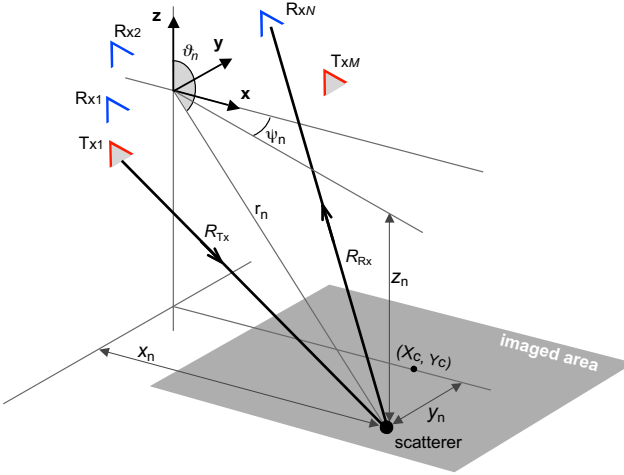


Figure 5.1: General geometric configuration of the Tx and Rx subarrays showing the path lengths R_{Tx} and R_{Rx} to a point scatterer at (x_n, y_n, z_n) .

Throughout this chapter the distance r_n will be assumed much larger than the spacing between the subarrays, i.e., $r_n \gg |\mathbf{x}_t|, |\mathbf{x}_r|$. The assumption is

justified when the Tx and Rx subarrays are mounted on a single platform with a maximum extension small compared to the distance to the imaged area. Using Newtons binomial series [45]

$$\sqrt{1-\nu} = \sum_{p=0}^{\infty} \binom{\frac{1}{2}}{p} (-\nu)^p = 1 - \frac{1}{2}\nu - \frac{1}{8}\nu^2 - \frac{1}{16}\nu^3 - \dots \quad \text{for } |\nu| \leq 1 \quad (5.4)$$

to approximate R_{Tx} from its square value in (5.2) gives

$$\begin{aligned} R_{\text{Tx}} \approx \tilde{R}_{\text{Tx}} &= r_n - x_t \sin \vartheta_n \cos \psi_n - y_t \sin \vartheta_n \sin \psi_n - z_t \cos \vartheta_n \\ &\quad + \frac{x_t^2 + y_t^2 + z_t^2}{2r_n}. \end{aligned} \quad (5.5)$$

Similarly, the receive path (5.3) is approximated to

$$\begin{aligned} R_{\text{Rx}} \approx \tilde{R}_{\text{Rx}} &= r_n - x_r \sin \vartheta_n \cos \psi_n - y_r \sin \vartheta_n \sin \psi_n - z_r \cos \vartheta_n \\ &\quad + \frac{x_r^2 + y_r^2 + z_r^2}{2r_n}. \end{aligned} \quad (5.6)$$

The total path $\tilde{R}_{\text{Tx}} + \tilde{R}_{\text{Rx}}$ then evaluates to

$$\begin{aligned} \tilde{R}_{\text{Tx}} + \tilde{R}_{\text{Rx}} &= 2r_n + (x_t^2 + x_r^2 + y_t^2 + y_r^2 + z_t^2 + z_r^2)/2r_n \\ &\quad - (x_t + x_r) \sin \vartheta_n \cos \psi_n - (y_t + y_r) \sin \vartheta_n \sin \psi_n \\ &\quad - (z_t + z_r) \cos \vartheta_n. \end{aligned} \quad (5.7)$$

The above approximation will be used throughout this chapter for determining the total path length transmitter–scatterer–receiver.

5.2 Angular Compression

After range compression (see section 2.6) the distance transmitter–scatterer–receiver is known for each scatterer and Tx/Rx combination. However, all scatterers with equal distances $R_{\text{Tx}i} + R_{\text{Rx}j}$ will appear within one range resolution cell, independently of their angular position. It is the purpose of the angular (i.e., azimuth and elevation) compression to separate the scatterers

according to their angular position. This is done by *focusing* the array on each angular position.

In the following, the range compressed received signal due to one unit point scatterer (i.e., $f(\mathbf{x}_n) = 1$) as given in section 2.6 will be considered. The respective expression (2.13) is repeated here for convenience

$$f_{\text{rc}}(\tau, \mathbf{x}_{\text{ti}}, \mathbf{x}_{\text{rj}}, \mathbf{x}_n) = e^{-j\frac{2\pi}{\lambda}(R_{\text{Tx}i} + R_{\text{Rx}j})} e^{+j2\pi k_e T_p(\tau - \tau_n)} \cdot \frac{\sin(2\pi k_e (T_p |\tau - \tau_n| - (\tau - \tau_n)^2))}{2\pi k_e |\tau - \tau_n|} \text{rect}\left[\frac{|\tau - \tau_n|}{T_p}\right]. \quad (5.8)$$

Assuming only a single point scatterer is no restriction to the generality of the developed mathematical models, since the received signal is a *linear weighted sum* over all point scatterers (see section 2.4). The angular compression (focusing) to certain direction is performed by multiplying each received signal by the complex conjugate of the predicted (calculated) signal from that direction and then summing up over all Tx/Rx combinations. This is equivalent to evaluating the double-summation of the optimum focusing given in section 2.5. Considering only the first exponential term in (5.8) which is the only term with a direct dependency on the angular position, the angular compressed signal $f'_{\text{ac}}(\cdot)$ focused to an arbitrary azimuth and elevation angle pair ψ_0 and ϑ_0 , respectively, is given by

$$f'_{\text{ac}}(\mathbf{x}_n) = \sum_{i=1}^M \sum_{j=1}^N e^{-j\frac{2\pi}{\lambda}(R_{\text{Tx}i} + R_{\text{Rx}j})} \left[e^{-j\frac{2\pi}{\lambda} K_{\text{ac}}(\psi_0, \vartheta_0)} \right]^*. \quad (5.9)$$

The second exponential term in the above expression is known as the *focusing kernel*. The exponent $K_{\text{ac}}(\psi_0, \vartheta_0)$ of the kernel is set by the focusing algorithm and, in general depends on \mathbf{x}_{t} and \mathbf{x}_{r} , the angles ψ_0 and ϑ_0 , as well as the distance r . To focus on a point at $(r_n, \vartheta_n, \psi_n)$ the value of $K_{\text{ac}}(\psi_0, \vartheta_0)$ should be an estimate of the distance $R_{\text{Tx}i} + R_{\text{Rx}j}$ to that point. If $K_{\text{ac}}(\psi_0, \vartheta_0) = R_{\text{Tx}i} + R_{\text{Rx}j}$ all the exponents within the summation cancel out and $f'_{\text{ac}}(\cdot)$ becomes equal to NM .

In practice, only an approximation of $R_{\text{Tx}i} + R_{\text{Rx}j}$ can be determined, its accuracy depending mainly on the range resolution. A compact expression for the angular compressed signal is found if the approximation (5.7) is used and

$K_{ac}(\psi_0, \vartheta_0)$ set equal to

$$\begin{aligned}
 K_{ac}(\psi_0, \vartheta_0) &= (x_t^2 + x_r^2 + y_t^2 + y_r^2 + z_t^2 + z_r^2)/2\tilde{r} \\
 &\quad - (x_t + x_r) \sin \vartheta_0 \cos \psi_0 - (y_t + y_r) \sin \vartheta_0 \sin \psi_0 \\
 &\quad - (z_t + z_r) \cos \vartheta_0.
 \end{aligned} \tag{5.10}$$

It should be noted, that the position of the Tx and Rx subarrays \mathbf{x}_t and \mathbf{x}_r are known. Using the above approximations the compressed signal focused to the angular coordinates ϑ_0 and ψ_0 is¹

$$\begin{aligned}
 f'_{ac}(\mathbf{x}_n) &\approx \sum_{i,j}^{M,N} e^{-j\frac{2\pi}{\lambda}(\tilde{R}_{Tx_i} + \tilde{R}_{Rx_j})} \left[e^{-j\frac{2\pi}{\lambda} K_{ac}(\psi_0, \vartheta_0)} \right]^* \\
 &\approx e^{-j\frac{2\pi}{\lambda} 2r_n} \sum_{i,j}^{M,N} \left[e^{-j\frac{2\pi}{\lambda} (|\mathbf{x}_{ti}|^2 + |\mathbf{x}_{rj}|^2) \left(\frac{1}{2r_n} - \frac{1}{2\tilde{r}} \right)} \right. \\
 &\quad e^{+j\frac{2\pi}{\lambda} (x_{ti} + x_{rj}) (\sin \vartheta_n \cos \psi_n - \sin \vartheta_0 \cos \psi_0)} \\
 &\quad e^{+j\frac{2\pi}{\lambda} (y_{ti} + y_{rj}) (\sin \vartheta_n \sin \psi_n - \sin \vartheta_0 \sin \psi_0)} \\
 &\quad \left. e^{+j\frac{2\pi}{\lambda} (z_{ti} + z_{rj}) (\cos \vartheta_n - \cos \vartheta_0)} \right].
 \end{aligned} \tag{5.11}$$

The distance r_n can be assumed constant within one range cell, thus the only contribution of the exponential term outside the summation is a constant phase, which is of no significance to the angular compression. The first exponential inside the summation $e^{-j\frac{2\pi}{\lambda} (|\mathbf{x}_{ti}|^2 + |\mathbf{x}_{rj}|^2) \left(\frac{1}{2r_n} - \frac{1}{2\tilde{r}} \right)}$ represents the near field influence term; section 5.3 deals with the influence and relevance of this term.

To summarize, the expression in (5.11) represents the angular focused signal for the echo received from one point scatterer. All terms related to \mathbf{x}_t and \mathbf{x}_r (e.g., M , N , or x_{ti}) are a priori known, since the subarrays' locations are known. All terms related to the angles ϑ_n and ψ_n are unknown, since they involve the unknown scatterer position. The scatterer's range r_n is approximately known after range compression. All terms related to the focusing kernel,

¹The expression for the first exponential is an approximation because the exact value of $\tilde{R}_{Tx_i} + \tilde{R}_{Rx_j}$ in (5.9) is replaced by the approximation $\tilde{R}_{Tx_i} + \tilde{R}_{Rx_j}$. The measured signals, however, are exact because physics does not involve any approximation.

i.e., the range \tilde{r} , and the angles ϑ_0 and ψ_0 are determined a priori through the focusing algorithm. They can be interpreted as the “looking direction” of the focusing algorithm.

5.3 The Near Field Correction

The expression (5.11) for the azimuth compressed signal includes the near field influence term. This term is not directly related to the azimuth compression (focusing), though it may need to be accounted for to avoid a defocusing of the image. The near field term results from including the quadratic terms of the binomial series expansion in (5.5). This section deals with two questions:

- What is the degradation in image quality due to the near field influence?
- When is it necessary to include a near field correction in the processing?

The near field influence term is given by the first exponential within the summation in (5.11). When focusing to a point \mathbf{x}_n , the angles ϑ_n and ψ_n are set equal to ϑ_0 and ψ_0 , respectively, thus reducing all focusing exponential terms in (5.11) to unity. The only term remaining is

$$e_{\text{NF}}(\mathbf{x}_{ti}, \mathbf{x}_{rj}) = \sum_{i,j}^{M,N} e^{-j\frac{2\pi}{\lambda}(|\mathbf{x}_{ti}|^2 + |\mathbf{x}_{rj}|^2)\frac{1}{2r_n}} \cdot e^{+j\frac{2\pi}{\lambda}(|\mathbf{x}_{ti}|^2 + |\mathbf{x}_{rj}|^2)\frac{1}{2\tilde{r}}}. \quad (5.12)$$

The complex valued near field influence term e_{NF} thus represents the deviation from the ideal value that would be obtained for a “perfectly” focused signal. The first exponential represents the *phase error* due to each Tx/Rx antenna position; the second exponential represents the *phase correction* set by the focusing algorithm to compensate the phase error. The phase error—and consequently also the phase correction—depends on the scatterers position through the a priori unknown range r_n . It should be noted that the influence term is a measure of the combined near field phase error from *all* Tx and Rx elements. In this sense the approach used here is different from other methods [96, 52], which use the maximum phase error for a single (worst case) receive–transmit combination as an evaluation criterion.

The near field correction term is a function of the (known) Tx and Rx elements positions \mathbf{x}_{ti} , \mathbf{x}_{rj} , the distance r_n , and the estimation of this distance \tilde{r} . It is for this distance approximation that the near field correction can't be evaluated exactly, since the estimation accuracy of \tilde{r} depends primarily on the range resolution². In the ideal case $\tilde{r} = r_n$ and the near field influence term is equal to MN , i.e., with no influence on the focusing. In practice $\tilde{r} \neq r_n$, and \tilde{r} is rather written as $\tilde{r} = r_n + \Delta r$ where Δr represents the deviation (error) from the exact range and is assumed independent of \mathbf{x}_{ti} and \mathbf{x}_{rj} . Inserting into (5.12) gives

$$e_{\text{NF}}(\mathbf{x}_{ti}, \mathbf{x}_{rj}) \approx \sum_i^M e^{-j \frac{2\pi}{\lambda} \frac{|\mathbf{x}_{ti}|^2 \Delta r}{r_n^2}} \sum_j^N e^{-j \frac{2\pi}{\lambda} \frac{|\mathbf{x}_{rj}|^2 \Delta r}{r_n^2}} \quad (5.13)$$

where some simplifications have been introduced assuming that \tilde{r} is a “good” estimate for r_n , i.e., $\Delta r \ll r_n$. In the above expression the contributions of the Tx and Rx arrays to the influence term have been separated through the two summations. Since the two summations are interchangeable it is sufficient to analyze only the first (transmit array) and later adopt the results to both summations. It should be noted that the expression for e_{NF} when no near field correction is performed is obtained by setting $1/2\tilde{r} = 0$ in (5.12) or equivalently in (5.13) through

$$\Delta r = \frac{r_n}{2}. \quad (5.14)$$

The summation of the exponentials in (5.13) can be represented by a vector sum of M *phasors* each of unit amplitude and a phase shift (direction) proportional to Δr and the square of the distance from the origin to the respective Tx element $|\mathbf{x}_{ti}|^2$. The phase shift represents the angle of the phase with respect to the horizontal. Two extreme cases are recognized:

No near field influence (best case): all phasors have the same phase (direction), then the phase of the sum vector will still be the same but its length equal to M (see Fig. 5.2(a)). This is the case if all transmitters are placed on a circle of radius $|\mathbf{x}_t| = |\mathbf{x}_{ti}|$ centered at the origin (see Fig. 5.2(b)). The only effect of the near field influence term would be to

²It is obvious that the measured distance $R_{\text{Tx}i} + R_{\text{Rx},j}$ is, in general, not equal to the distance r_n to the center of the coordinate system. It is rather necessary to calculate \tilde{r} by triangulation using the known positions of the antenna elements.

shift the phase of the focused signal, which does not result in any image degradation.

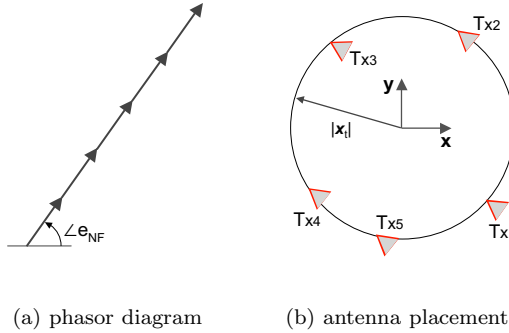


Figure 5.2: Phasor diagram and antenna location for *best case*.

Maximum near field influence (worst case): the phase (direction) of the phasors is such that the length of the sum vector is equal to zero (see Fig. 5.3(a)). This requires the transmitters to be positioned at different distances from the origin (see Fig. 5.3(b)). In this case the resultant signal is completely unfocused and its energy spread throughout the image.

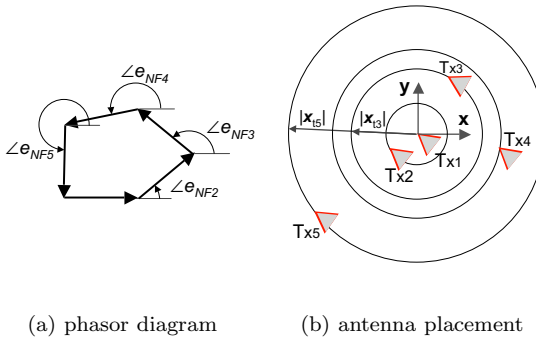


Figure 5.3: Phasor diagram and antenna location for *worst case*.

From the above two cases it is concluded that the total resultant phase $\angle e_{\text{NF}}$ does not result in any defocusing of the image, however it is crucial to consider the amplitude $|e_{\text{NF}}|$ which depends on the individual phases $\angle e_{\text{NF}i}$. The amount of defocusing depends on the location of the Tx antenna elements. As mentioned earlier, the identical argumentation is also true for the Rx array.

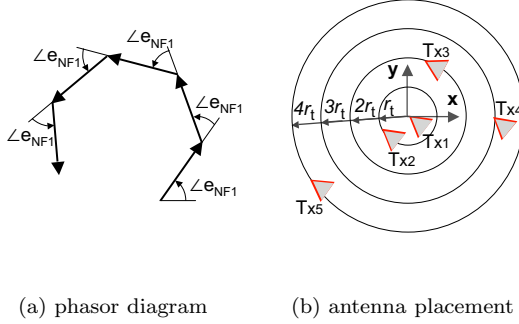


Figure 5.4: Phasor diagram and antenna location for transmitters located on concentric circles centered at the origin.

A pessimistic (and realistic) measure for the amount of defocusing can be obtained if a progressive but constant phase shift is assumed for each phasor as shown in Fig. 5.4(a). This corresponds to transmitters and receivers located on concentric spheres about the origin such that the radii of the spheres are

$$|\mathbf{x}_{t_i}| = i r_t \quad , \quad i = 1, \dots, M \quad (5.15)$$

$$|\mathbf{x}_{r_j}| = j r_r \quad , \quad j = 1, \dots, N \quad (5.16)$$

where r_t and r_r are positive constants (see Fig. 5.4(b)). When inserting the above into (5.13) the near field influence can be expressed in a closed form:

$$e_{\text{NF}}(r_t, r_r) = \frac{\sin\left(\frac{M\pi}{\lambda} \frac{r_t^2 \Delta r}{r_n^2}\right) \sin\left(\frac{N\pi}{\lambda} \frac{r_r^2 \Delta r}{r_n^2}\right)}{\sin\left(\frac{\pi}{\lambda} \frac{r_t^2 \Delta r}{r_n^2}\right) \sin\left(\frac{\pi}{\lambda} \frac{r_r^2 \Delta r}{r_n^2}\right)} e^{-j\frac{\pi}{\lambda} \frac{(M+1)r_t^2 \Delta r}{r_n^2} - j\frac{\pi}{\lambda} \frac{(N+1)r_r^2 \Delta r}{r_n^2}} \quad (5.17)$$

As mentioned earlier only the amplitude of the above near field influence term is relevant for the defocusing. Ideally $|e_{\text{NF}}(r_t, r_r)| = \max\{|e_{\text{NF}}(r_t, r_r)|\} = MN$

which is equivalent to no defocusing (best case). For a required lower bound on $|e_{\text{NF}}(r_t, r_r)|$ it is possible to solve (5.17) numerically. A closed form for the maximum allowed extent of the Tx and Rx arrays can, however, be obtained by requiring that

$$Mr_t = \max\{|\mathbf{x}_t|\} \leq R_{\text{near}} \sqrt{\frac{\gamma M \lambda}{|\Delta r|}} \quad (5.18)$$

$$Nr_r = \max\{|\mathbf{x}_r|\} \leq R_{\text{near}} \sqrt{\frac{\gamma N \lambda}{|\Delta r|}} \quad (5.19)$$

where the value of $\gamma \ll 1$ determines the maximum error, and Mr_t and Nr_r are the radii of the spheres containing the Tx and Rx arrays, respectively. Worst case has been assumed by setting $r_n = \min\{|r_n|\} = R_{\text{near}}$. For example, a total defocusing of less than 1 % requires a value of $\gamma \leq 0.055$.

The corresponding expression for the allowed upper array extent without near field correction is obtained by inserting (5.14) into (5.18) and (5.19) giving

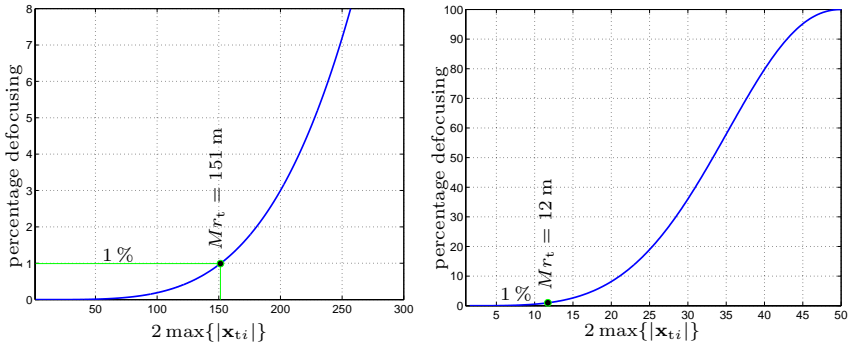
$$Mr_t = \max\{|\mathbf{x}_t|\} \leq \sqrt{2R_{\text{near}}\gamma M \lambda} \quad (5.20)$$

$$Nr_r = \max\{|\mathbf{x}_r|\} \leq \sqrt{2R_{\text{near}}\gamma N \lambda} \quad (5.21)$$

As an example, the percentage defocusing $(MN - |e_{\text{NF}}|)/MN \cdot 100\%$ is calculated as a function of the array extent $2Mr_r$ for identical transmit and receive arrays $|\mathbf{x}_{ti}| = |\mathbf{x}_{rj}|$, $\forall i, j$. The example system operates at 9.6 GHz and uses $M = N = 10$ Tx and Rx antenna elements to image a point scatterer at $r_n = R_{\text{near}} = 1$ km. Two cases are distinguished:

With near field correction: as shown in Fig. 5.5(a) the percentage defocusing increases when increasing the extent of the arrays, although the near field correction is included in the processing. For $\Delta r = 3$ m, the 1 % error bound is obtained by substituting the value of $\gamma = 0.055$ into (5.18) which results in $2Mr_t = 151$ m as marked on the curve.

Without near field correction: the percentage defocusing without near field correction is plotted in Fig. 5.5(b). A 100 % defocusing corresponds to the *worst case* detailed earlier in this section. In general, it is obvious that for this example system, the defocusing is significantly higher for the case of no near field correction than with correction.

(a) with near field correction and $\Delta r = 3$ m

(b) without near field correction

Figure 5.5: Percentage defocusing due to the near field influence as a function of the maximum array extent, for $\lambda = 3.1$ cm, $M = N = 10$, and $R_{\text{near}} = 1$ km, assuming identical transmit/receive arrays $|\mathbf{x}_{ti}| = |\mathbf{x}_{rj}|$, $\forall i, j$.

5.3.1 Summary on Near Field Corrections

To summarize, it is concluded that the near field correction substantially reduces the defocusing of the image. For *reasonable* values of the range deviation Δr the maximum allowable array extent for a given defocusing is always higher for the case of near field correction. The near field influence leads to contradicting requirements on the array extent, since large element spacing and thus large array extent is favorable for a high resolution but on the other hand produces a larger near field influence. However, for imaged areas that are far away from the radar, i.e., large R_{near} , the defocusing can get insignificant even without near field correction. It should be noted that for the case of no near field correction the defocusing becomes independent of the range accuracy Δr , which is the critical parameter for the accuracy of the correction. In section 5.8.3 simulation examples will be given to validate the results obtained in this section.

5.4 General Condition for the Occurrence of Angular Ambiguities

In the general case, the Tx and Rx antennas of a real aperture radar can't be placed along a line with constant spacings. But instead, their positions will be dictated by the carrier platform. Since the performance of the imaging system is mostly determined by the antennas' positions, it is necessary to consider the antenna placement in detail. Due to the *real aperture* imaging it is known that a larger element spacing improves the angular resolution. However, on the other hand spacings greater than $\lambda/2$ can result in angular ambiguities [88, 67]. In this section the condition for the occurrence of angular ambiguities for non-uniform multi-Tx/Rx antennas of arbitrary radiation pattern will be derived. The condition will then be simplified to obtain a closed expression for the position of angular ambiguities as a function of the antenna configuration.

An ambiguity occurs if-and-only-if two (or more) plane waves impinging on the array from different directions result in identical signals for *all* receive elements. For a multi-Tx/Rx antenna system this condition must be true independent of the Tx antenna being the source of the scattered wave. In the case of a radar detecting point targets, ambiguities mean that it is not possible to uniquely determine the direction of the target. For an imaging radar ambiguities, on the other hand, mean that certain structures within the imaged area will appear at multiple positions within the image or even that structures from outside the imaged area may be mapped into the image [96]. In all cases angular ambiguities are not desirable and should be avoided.

Starting point is the range compressed echoed signal for the Rx element j at \mathbf{x}_{rj} due to a transmitted signal by transmitter i at \mathbf{x}_{ti} as given by (5.8). All terms related to the time delay variable τ can be neglected since they have no influence on the angular ambiguities. Rewriting the expression while additionally including the weighting introduced through the radiation patterns gives

$$f_{rc}(\mathbf{x}_{ti}, \mathbf{x}_{rj}, \mathbf{x}_n) = C_{Tx_i}(\psi'_n, \vartheta'_n) C_{Rx_j}(\psi'_n, \vartheta'_n) \cdot e^{-j \frac{2\pi}{\lambda} (R_{Tx_i} + R_{Rx_j})}. \quad (5.22)$$

where $C_{Tx_i}(\psi'_n, \vartheta'_n)$ and $C_{Rx_j}(\psi'_n, \vartheta'_n)$ are the radiation patterns associated with the transmit and receive antennas respectively. The angular focusing kernel

(cf. section 5.2) is not included in the above expression, since the occurrence of an ambiguity is independent of the focusing angles³ (ψ_0, ϑ_0) . Equivalently, the ambiguities can be understood as *grating lobes* known from antenna array technique [6, 67, 126], in this case (5.22) represents the signal of one element of the array and the grating lobes are identified through the *array factor*. This involves a weighting vector applied on the elements to *steer* the array to the angles (ψ_n, ϑ_n) .

Using the approximation (5.7) for the distance terms and neglecting the near field and constant phase terms gives

$$f_{\text{rc}}(\mathbf{x}_{ti}, \mathbf{x}_{rj}, \mathbf{x}_n) = C_{\text{Tx}i}(\psi'_n, \vartheta'_n) C_{\text{Rx}j}(\psi'_n, \vartheta'_n) \cdot e^{+j\frac{2\pi}{\lambda}(x_{ti}+x_{rj}) \sin \vartheta_n \cos \psi_n} \cdot e^{+j\frac{2\pi}{\lambda}(y_{ti}+y_{rj}) \sin \vartheta_n \sin \psi_n} \cdot e^{j\frac{2\pi}{\lambda}(z_{ti}+z_{rj}) \cos \vartheta_n}. \quad (5.23)$$

It is seen that in the above expression the coordinates of the transmitter and receiver always appear as a sum in the phase term, whereas the radiation patterns appear as a product in the amplitude term. Without restriction of generality the following substitution can now be introduced

$$\mathbf{x}_l = \mathbf{x}_{ti} + \mathbf{x}_{rj} \quad (5.24)$$

$$C_l(\psi_n, \vartheta_n) = C_{\text{Tx}i}(\psi'_n, \vartheta'_n) \cdot C_{\text{Rx}j}(\psi'_n, \vartheta'_n) \quad (5.25)$$

$$f_l = f_{\text{rc}}(\mathbf{x}_{ti}, \mathbf{x}_{rj}, \mathbf{x}_n) \quad (5.26)$$

where $l = 1, \dots, MN$.

The substitution can be interpreted as a replacement of the *real* Tx/Rx antennas by a single isotropic transmitter positioned at the center of the coordinate system and a total of NM *virtual* receivers positioned at $\mathbf{x}_{ti} + \mathbf{x}_{rj}$. A detailed treatment of the concept of virtual receivers and their mathematical description is given in [52]. Note that after the substitution the point scatterer position \mathbf{x}_n is no longer explicitly included in the expression of the receive signal. Substitution (5.24) to (5.26) into (5.23) gives

$$f_l = C_l(\psi_n, \vartheta_n) \cdot e^{+j\frac{2\pi}{\lambda}x_l \sin \vartheta_n \cos \psi_n} \cdot e^{+j\frac{2\pi}{\lambda}y_l \sin \vartheta_n \sin \psi_n} \cdot e^{j\frac{2\pi}{\lambda}z_l \cos \vartheta_n}. \quad (5.27)$$

Now consider a second point scatterer within the same range gate but positioned at $\mathbf{x}_{n,\text{amb}} = (r_n, \psi_{\text{amb}}, \vartheta_{\text{amb}})$. Proceeding through the same steps as

³This is true because an imaging radar focuses to each point within the imaged area. The occurrence of angular ambiguities is thus related to the total extent of this area.

before gives

$$\begin{aligned}
 f_{l,\text{amb}} = & C_l(\psi_{\text{amb}}, \vartheta_{\text{amb}}) \cdot e^{+j\frac{2\pi}{\lambda} x_l \sin \vartheta_{\text{amb}} \cos \psi_{\text{amb}}} \cdot \\
 & e^{+j\frac{2\pi}{\lambda} y_l \sin \vartheta_{\text{amb}} \sin \psi_{\text{amb}}} \cdot e^{j\frac{2\pi}{\lambda} z_l \cos \vartheta_{\text{amb}}}.
 \end{aligned} \tag{5.28}$$

The aim is to determine the existence and values of ambiguous angles $(\psi_{\text{amb}}, \vartheta_{\text{amb}})$. The conditions for the existence of an ambiguity can be stated as follows

1. Phase Condition: the phase differences between any two antennas are identical, modulo an integer multiple of 2π

$$\begin{aligned}
 \angle f_l - \angle f_{l+1} & \stackrel{!}{=} \angle f_{l,\text{amb}} - \angle f_{l+1,\text{amb}} + m_l \cdot 2\pi \\
 \text{where } m_l & \in \mathbb{Z}; \quad l = 1, \dots, MN - 1.
 \end{aligned} \tag{5.29}$$

2. Amplitude Condition: the amplitude of the received signals should be identical for both point scatterers, excluding a constant factor which is due to a possible difference in distance and independent of the receive element

$$\begin{aligned}
 \frac{|f_l|}{|f_{l+1}|} & \stackrel{!}{=} \frac{|f_{l,\text{amb}}|}{|f_{l+1,\text{amb}}|} \\
 \text{where } |f_l|, |f_{l,\text{amb}}| & \neq 0 \quad \forall \quad l = 2, \dots, MN - 1.
 \end{aligned} \tag{5.30}$$

The phase condition is related to the exponential terms and thus to the angle of incidence. The amplitude condition is related to the —angle dependent— weighting imposed by the radiation pattern of the individual antenna elements. Combining conditions 1. and 2. is equivalent to the requirement of equal complex ratios of the received signals

$$\frac{f_l}{f_{l+1}} \stackrel{!}{=} \frac{f_{l,\text{amb}}}{f_{l+1,\text{amb}}}. \tag{5.31}$$

The above gives a general condition for the occurrence of an ambiguity, i.e., the angles $\psi_n \neq \psi_{\text{amb}}$ and $\vartheta_n \neq \vartheta_{\text{amb}}$ are ambiguous if for a given array configuration the receive signals satisfy (5.31). It should be noted that the azimuth ambiguity condition is *not* a function of range r_n , which can easily

be verified by inserting (5.27) and (5.28) into (5.31). For an array of isotropic elements a front-back ambiguity exists, i.e., $\psi_{\text{amb}} = 180^\circ - \psi_n$, $\forall \psi_n$ which is independent of the array configuration.

5.4.1 Azimuth Ambiguities

At this point the ambiguities relevant for a forward radar are investigated. The general condition derived in the previous section does not separate azimuth angle from elevation angle ambiguities. Actually, satisfying (5.31) means that there exist two combination of angles (ψ_n, ϑ_n) and $(\psi_{\text{amb}}, \vartheta_{\text{amb}})$ such that two plane waves arriving from these directions can't be differentiated. For a forward radar the range r_n is known after chirp compression. In addition the elevation angle ϑ_n of a point scatterer is uniquely defined through the range r_n , the platform height⁴ $|z_n|$ and the azimuth angle ψ_n (see Fig. 5.1). For a flat earth the intersection of the plane $z = -z_n = \text{constant}$ with the constant range spheres results in circles which are uniquely defined for scatterers within the half space $x_n > 0$. This means, that the range is unique and the same is true for the elevation angle. As a consequence it is only necessary to consider azimuth ambiguities, i.e., with respect to the angle ψ and thus only the first two exponential terms in (5.27) and (5.28) need to be regarded. A further simplification results by solving the ambiguity condition for the x and y coordinates independently. This is not a restriction to the generality of the solution, since it is still necessary to simultaneously fulfill both conditions for an ambiguity to occur. In addition to enabling a simpler mathematical handling, this gives a worst case condition since the antenna configuration can be selected so as to avoid ambiguities along both $\hat{\mathbf{e}}_x$ and $\hat{\mathbf{e}}_y$ directions.

Inserting (5.27) and (5.28) into (5.31) and considering only azimuth ambiguities for the antenna elements along $\hat{\mathbf{e}}_y$ gives

$$\frac{C_l(\psi_n)}{C_{l+1}(\psi_n)} e^{+j\frac{2\pi}{\lambda}(y_l - y_{l+1}) \sin \vartheta_n \sin \psi_n} \stackrel{!}{=} \frac{C_l(\psi_{\text{amb}})}{C_{l+1}(\psi_{\text{amb}})} e^{+j\frac{2\pi}{\lambda}(y_l - y_{l+1}) \sin \vartheta_n \sin \psi_{\text{amb}}}. \quad (5.32)$$

An array consisting of single elements of different radiation patterns will

⁴For flat earth all scatterers are concentrated on the xy -plane and the platform height above ground is given by $|z_n|$.

have an unambiguous angular segment larger than the corresponding array of identical elements. According to (5.32) this is because in addition to the phase condition (given by the exponential terms) the amplitude condition has to be satisfied. A closed expression for the angular ambiguity can only be obtained assuming identical radiation patterns, i.e., $C_1(\psi) = C_2(\psi) = \dots = C_{NM}(\psi)$. Then (5.32) further simplifies to

$$e^{-j\frac{2\pi}{\lambda}\Delta y_l \sin \vartheta_n \sin \psi_n} = e^{-j\frac{2\pi}{\lambda}\Delta y_l \sin \vartheta_n \sin \psi_{\text{amb}}}, \quad l = 1, \dots, MN - 1$$

$$\Rightarrow \frac{\Delta y_l}{\lambda} (\sin \psi_n - \sin \psi_{\text{amb}}) \sin \vartheta_n = m_l, \quad m_l \in \mathbb{Z} \quad (5.33)$$

where the spacings between the antenna elements have been written as

$$\Delta y_l = y_{l+1} - y_l, \quad l = 1, \dots, MN - 1. \quad (5.34)$$

It should be noted that for a linear *uniform* array, i.e., $\Delta y_l = \Delta y$ the condition (5.33) simplifies to the well known form for the occurrence of grating lobes in phased arrays [88]⁵.

Considering only forward and no backward operation of the radar will limit the angular segment to $-\pi/2 \leq \psi_n \leq \pi/2$; in addition it will be required that $-\pi/2 \leq \psi_{\text{amb}} \leq \psi_n$. This way, the sin-function in (5.33) are monotone and the smallest values of the integers $|m_l|$ will determine the ambiguity angle ψ_{amb} nearest to the focusing angle ψ_n . An ambiguity is found by determining the integers m_1, \dots, m_{MN-1} which together with the spacings $\Delta y_1, \dots, \Delta y_{MN-1}$ result in the same value for ψ_{amb} .

The normalized spacing between the elements is written as the ratio of relative prime integer numbers

$$\frac{\Delta y_l}{\lambda} = \frac{a_l}{b_l}, \quad a_l, b_l \in \mathbb{Z}; \text{ relative prime}; \quad b_l \neq 0. \quad (5.35)$$

In addition

$$(\sin \psi_n - \sin \psi_{\text{amb}}) \sin \vartheta_n = \frac{c}{d}, \quad c, d \in \mathbb{Z}; \text{ relative prime}; \quad d \neq 0. \quad (5.36)$$

⁵However, the treatment of uniform arrays in section 5.6 is more general than in [88] since it allows the Tx element spacing to be different from the Rx element spacing.

Presuming rational integers does not impose any practical restriction on the quantities to the left of the equal sign in (5.35) and (5.36). Substituting into (5.33) and rearranging gives

$$\frac{c}{b_l} \cdot \frac{a_l}{d} = m_l \quad , \quad m_l \in \mathbb{Z}; \quad l = 1, \dots, MN - 1. \quad (5.37)$$

Since a_l/b_l and c/d are both relatively prime, each of the two fractions in the above expression must result in an integer to satisfy (5.37). The approach is to determine the smallest values for the two fractions.

First fraction:

$$\frac{c}{b_l} \stackrel{!}{\in} \mathbb{Z}; \quad l = 1, \dots, MN - 1 \quad (5.38)$$

It is obvious that c has to be a common multiple of b_1, \dots, b_{MN-1} . The smallest value for the fraction is given by the smallest possible c . Hence, c is the least common multiple (*LCM*) of b_1, \dots, b_{MN-1} .

Second fraction:

$$\frac{a_l}{d} \stackrel{!}{\in} \mathbb{Z}; \quad l = 1, \dots, MN - 1 \quad (5.39)$$

Here d should be a common divisor of a_1, \dots, a_{MN-1} . The smallest value for the fraction is given by the greatest value for d . Hence, d is the greatest common divisor (*GCD*) of a_1, \dots, a_{MN-1} .

Substituting for c and d into (5.36) results in the final expression for the ambiguous angle

$$\psi_{\text{amb}} = \arcsin \left(\sin \psi_n - \frac{LCM \{b_1, \dots, b_{MN-1}\}}{GCD \{a_1, \dots, a_{MN-1}\}} \frac{1}{\sin \vartheta_n} \right). \quad (5.40)$$

The above expression can be used to determine the dependencies of the azimuth ambiguity on the angles ψ_n and ϑ_n for a given array configuration. As would be expected, the ambiguity angle is a function of *all* the spacings between the elements and not just the smallest spacing between two elements in the array.

This is demonstrated in Fig. 5.6, which shows the azimuth angle of the first order ambiguity $\psi_{\text{amb}, \nu=1}$ for a non-uniform array of 6 elements. For a

fixed elevation angle ϑ_n it is seen that the ambiguity “follows” the azimuth angle ψ_n , and disappears (i.e., $\psi_{\text{amb},\nu=1} = -90^\circ$) for larger negative values of ψ_n . The plot also suggests that the *azimuth* ambiguity angle depends on the *elevation* angle. The area bounded by the azimuth and elevation angles for which $\psi_{\text{amb},\nu=1} = -90^\circ$ is free of azimuth ambiguities.

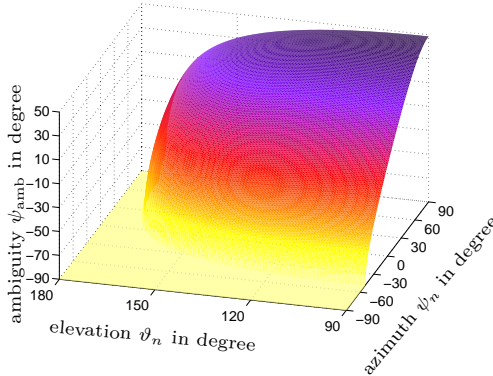


Figure 5.6: Angle of first order ambiguity $\psi_{\text{amb},\nu=1}$ as a function of azimuth and elevation angles ψ_n and ϑ_n , respectively. The spacings between the 6 elements of the linear array are given by $\Delta y_l = 4\lambda, 8\lambda, 8\lambda, 12\lambda, 16\lambda$.

5.4.2 Application of Ambiguity Condition

Expression (5.40) is used to calculate the ambiguous angle ψ_{amb} for a given non-uniform array. It should be noted that a set of values for Δy_l resulting in $\sin \psi_{\text{amb}} > 1$ corresponds to an ambiguous free antenna configuration. However, it turns out that such configurations most often result in high side-lobe levels and are thus of no practical use.

Consider a linear non-uniform array of $MN = 6$ elements positioned on the y -axis at $y_l = 0\lambda, 2\lambda, 4\lambda, 7\lambda, 10\lambda, 14\lambda$. The position of a point scatterer is given by $\psi_n = 20^\circ$ and $\vartheta_n = 90^\circ$. Using (5.40), the angle of the ambiguity is found to be at $\psi_{\text{amb}} = -41^\circ$ in accordance with the plot of the array factor in Fig. 5.7. Note that the smallest spacing $\min\{\Delta y_l\} = 2\lambda$ would result in an ambiguity at $\psi_{\text{amb}} = -9^\circ$, which as seen in Fig. 5.8(a) is much closer to ψ_n than for the non-uniform array. For comparison Fig. 5.8(b) shows the array factor of

a uniform array having the same number of elements $MN = 6$ and the same array span $y_{\max} - y_{\min} = 14\lambda$ as the non-uniform array. Both array factors have a main beam width (azimuth resolution) of 3.4° but the ambiguity of the uniform array is at $\psi_{\text{amb}} = -1^\circ$ which is considerably worse than for the non-uniform array.

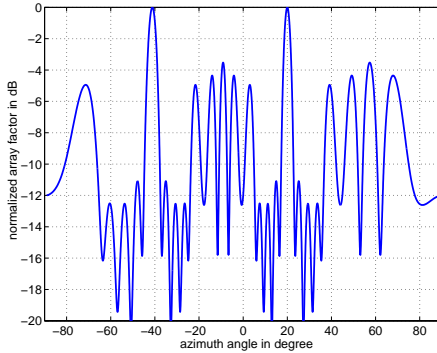
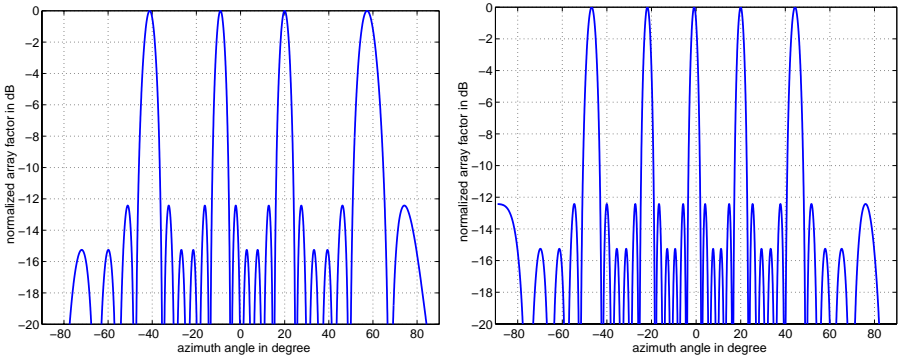


Figure 5.7: Array factor of a non-uniform array consisting of $MN = 6$ elements positioned at $y_l = 0\lambda, 2\lambda, 4\lambda, 7\lambda, 10\lambda, 14\lambda$. The array is scanned to $\psi_n = 20^\circ$.



(a) $\min\{\Delta y_l\} = 2\lambda, y_{\max} - y_{\min} = 10\lambda$

(b) $\min\{\Delta y_l\} = 2.8\lambda, y_{\max} - y_{\min} = 14\lambda$

Figure 5.8: Array factor of two uniform arrays consisting of $NM = 6$ elements, to be compared with the non-uniform configuration (cf. Fig. 5.7).

5.5 Multi-Tx/Rx Radar with Pulse Coded Chirp Waveforms

Pulse coded chirp operation is also possible when using real aperture radar. Using only one waveform would require a sequential operation of the transmitters, i.e., only one transmitter can be active at any time (see section 2.1). By using up and down-chirp waveforms at various start frequencies it is possible to simultaneously transmitting two (or more) uncorrelated chirps and hence increase the frame rate f_{frame} or equivalently reduce the measurement time. The received signals are still processed simultaneously as required by digital beam-forming; but now the echo due to two transmitted chirps is received simultaneously. It is only through the range compression (as detailed in section 2.6) that the two signals are separated. The basic principle for angular compression (see section 5.2) remains the same. If uncorrelated chirp waveforms are used, then processing for one specific waveform will suppress all other waveforms and, ideally the output is identical to that of a single chirp. Since the radar is an imaging radar, the quality criteria derived in section 3.4 can be used to determine the amount of suppression for different chirp waveforms. Digital beam-forming provides an additional advantage, since the data processing mainly involves adapting the focusing reference functions for the different transmit chirp parameters. In section 5.8.4 simulations will be used to demonstrate the performance of a coded chirp waveform radar.

5.6 Special Case of Linear Uniformly Spaced Arrays

In this section the special case of linear, uniformly spaced Tx/Rx subarrays will be investigated. Although this restricts the general formulation derived earlier, the simple analytic form of the results gives valuable insight, which is also applicable within the general form.

With reference to Fig. 5.9 all subarrays are placed on a line parallel to the y -axis. Without restriction of generality, it can be assumed that $x, y = 0$. In addition, the Tx and Rx subarrays are uniformly spaced and centered at y_{tc}

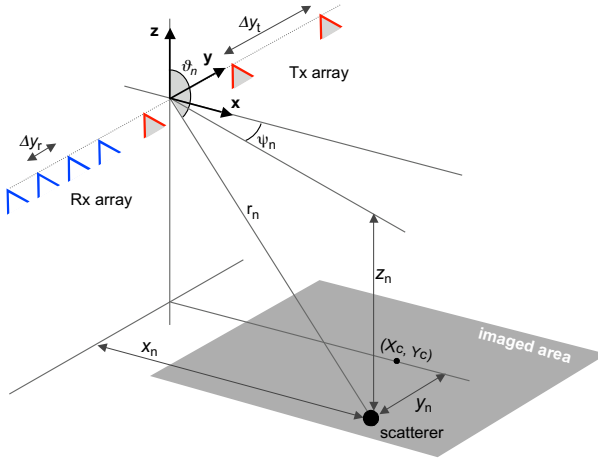


Figure 5.9: Geometry of Tx/Rx antenna elements for the case of a linear uniformly spaced array.

and y_{rc} , respectively, their positions are given by

$$y_{ti} = y_{tc} + i\Delta y_t \quad \text{for } i = -(M-1)/2, \dots, +(M-1)/2 \quad (5.41)$$

$$y_{rj} = y_{rc} + j\Delta y_r \quad \text{for } j = -(N-1)/2, \dots, +(N-1)/2. \quad (5.42)$$

5.6.1 Azimuth Compressed Signal

Next, (5.41) and (5.42) will be used to formulate the azimuth compressed signal derived in section 5.2 in a closed form. Neglecting the constant phase and near field terms, (5.11) gives

$$f'_{ac}(\Delta y_t, \Delta y_r, \mathbf{x}_n) = \sum_{i,j} e^{-j\frac{2\pi}{\lambda}(i\Delta y_t + j\Delta y_r)(\sin\vartheta_n \sin\psi_n - \sin\vartheta_0 \sin\psi_0)}. \quad (5.43)$$

The above can be further simplified to:

$$\begin{aligned}
 f'_{\text{ac}}(\Delta y_t, \Delta y_r, \mathbf{x}_n) &= \sum_i e^{-j \frac{2\pi}{\lambda} i \Delta y_t (\sin \vartheta_n \sin \psi_n - \sin \vartheta_0 \sin \psi_0)} \\
 &\quad \sum_j e^{-j \frac{2\pi}{\lambda} j \Delta y_r (\sin \vartheta_n \sin \psi_n - \sin \vartheta_0 \sin \psi_0)} \\
 &= \frac{\sin\left(\frac{\pi M}{\lambda} \Delta y_t (\sin \vartheta_n \sin \psi_n - \sin \vartheta_0 \sin \psi_0)\right)}{\sin\left(\frac{\pi}{\lambda} \Delta y_t (\sin \vartheta_n \sin \psi_n - \sin \vartheta_0 \sin \psi_0)\right)} \\
 &\quad \frac{\sin\left(\frac{\pi N}{\lambda} \Delta y_r (\sin \vartheta_n \sin \psi_n - \sin \vartheta_0 \sin \psi_0)\right)}{\sin\left(\frac{\pi}{\lambda} \Delta y_r (\sin \vartheta_n \sin \psi_n - \sin \vartheta_0 \sin \psi_0)\right)}. \tag{5.44}
 \end{aligned}$$

In this special case, the azimuth compressed signal is obviously the product of two $\sin x/x$ -functions. The resemblance to the radiation pattern of an antenna array consisting of M subarrays separated by Δy_t (first $\sin x/x$ -function), each of which consists of N single elements separated by Δy_r (second $\sin x/x$ -function) is intuitively clear [6]. It should be noted, that the real array consists of M transmit and N receive subarrays, however, (5.44) combines the Tx and Rx subarrays into one *virtual* receive array; the transmitter in this case would be an equivalent isotropic radiator placed at $\mathbf{x}_t = (0, y_{tc} + y_{rc}, 0)$ [11, 52].

From (5.44) it is evident that, in agreement with reciprocity [5], interchanging the transmitters and receivers will not change the resulting received signals. This is true both for the real (i.e., the product of Tx and Rx patterns) as well as for the virtual (i.e., either all Rx or all Tx and one isotropic element) arrays. Figures 5.10 and 5.11 clarify the interrelation of (5.44) between the Tx and Rx subarrays for the case of a single point scatterer. The Tx and Rx element spacings are $\Delta y_t = 7\lambda$ and $\Delta y_r = 1.3\lambda$, respectively, and the point scatterer is located at $\psi_n = 10^\circ$ and $\vartheta_n = 140^\circ$. The receive array's compressed signal⁶ in Fig. 5.10(a) shows a broad main lobe at the azimuth position of the scatterer. The width of the main lobe (i.e., azimuth resolution) is inversely proportional to the length $N\Delta y_r/\lambda$ of the receive array; the number of receive subarrays determines the main lobe's maximum value (height). On the other hand, the compressed signal of the Tx array⁷ in Fig. 5.10(b) shows a narrower main lobe

⁶This is the signal obtained if only one of M Tx subarray is used together with all N Rx subarrays.

⁷This corresponds to the signal from one of N Rx subarray when each of the M Tx subarrays is sequentially activated.

width (i.e., higher azimuth resolution) as compared to the receive array. This is due to the larger extent (length) $M\Delta y_t/\lambda$ of the Tx array. Using solely the Tx subarrays would result in a highly ambiguous signal, as seen by the large number of vertical strips in the figure.

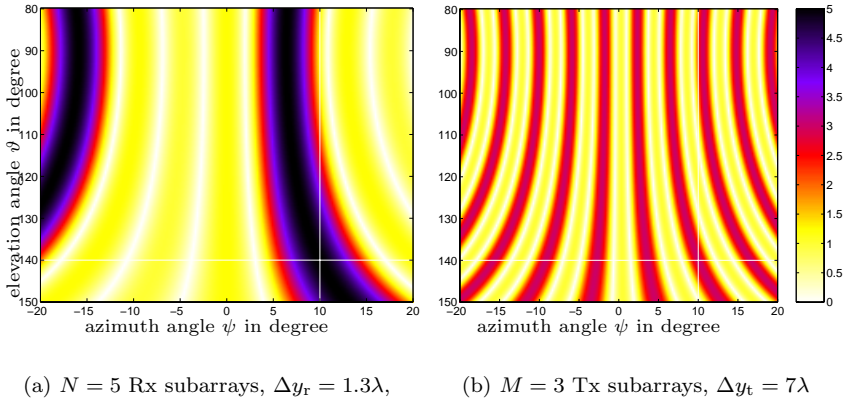


Figure 5.10: Intensity image of compressed signal for a point scatterer at $\psi_n = 10^\circ$ and $\vartheta_n = 140^\circ$ for the receive array (a), and the transmit array (b).

When the signals from the Tx and Rx subarrays are combined, all but the common of these ambiguities are eliminated, as seen in Fig. 5.11. In addition, the combined signal shows a higher contrast, given by the value of the product $NM = 15$ as compared to a peak of $N = 5$ and $M = 3$ of the individual Rx and Tx images, respectively.

As expected, the signal is not compressed in elevation (given by the angle ϑ), which is evident from the vertical strip structure in the figures. The reason is, that all point scatterer positioned at an arbitrary angle ϑ_n in the plane perpendicular to the line connecting the subarrays (in this case the xz -plane) will produce identical phases for all receive subarrays (provided they are in the far field of the stationary array). This can easily be understood by noting that all point scatterers positioned on a circle centered at the line connecting the subarrays (in this case the y -axis) will produce constant phase differences between the receive subarrays.

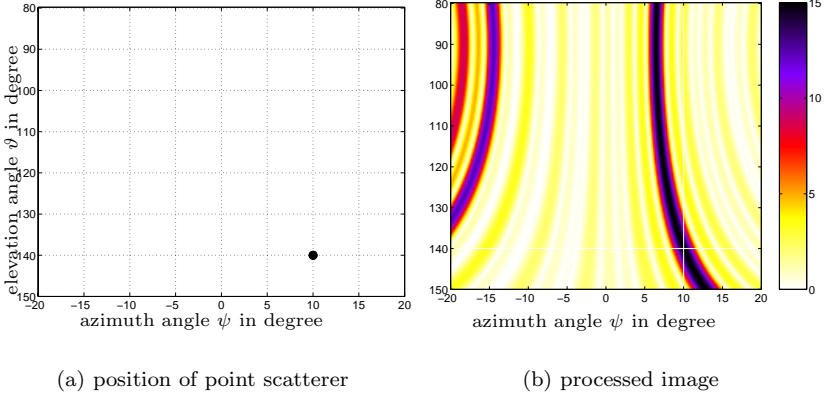


Figure 5.11: Position of point scatterer (a), and processed image (b) using combined signal of all 3 Tx and 5 Rx.

5.6.2 Azimuth Ambiguities

In the following, the azimuth ambiguities are investigated. An example of ambiguities is shown in Fig. 5.11 and manifest through the fact that it is not evident which one of the two vertical strips corresponds to the real azimuth position of the scatterer. Rather than using a geometric derivation based on the incoming plane wavefront [67], the expression in (5.44) will be used instead. The aim is to determine the maximum possible spacings Δy_t and Δy_r , while maintaining a (given) minimum suppression of the azimuth ambiguities.

5.6.2.1 Receive Array

Assuming $\Delta y_r \leq \Delta y_t$ the second $\sin x/x$ in (5.44) shows ambiguities at

$$\begin{aligned} \frac{\pi}{\lambda} \Delta y_t (\sin \vartheta_n \sin \psi_n - \sin \vartheta_n \sin \psi_{\text{amb},\nu}) &= \pi \nu & (5.45) \\ \Rightarrow \sin \psi_n - \sin \psi_{\text{amb},\nu} &= \frac{\lambda}{\Delta y_r \sin \vartheta_n} \nu \quad ; \quad \nu \in \mathbb{Z}, \nu \neq 0 \end{aligned}$$

where $|\nu|$ describes the order of the ambiguity. The justification for setting $\sin \vartheta_0 = \sin \vartheta_n$ in the above expression is valid, since as shown earlier all values

of elevation angle are ambiguous for an array placed parallel to the y -axis independently of the element spacing; hence the elevation angle $\vartheta_0 = \vartheta_n$ is determined through some other means⁸.

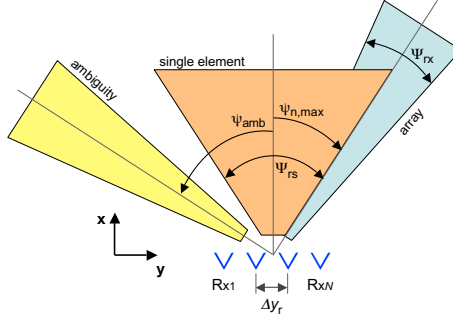


Figure 5.12: Receive subarrays forming a uniformly spaced linear array. The HPBW of each subarray is Ψ_{rs} while the array has a HPBW of Ψ_{rx} ; the ambiguity is at ψ_{amb} .

The approach is to determine the maximum Δy_r in order to avoid ambiguities within the imaged area. Fig. 5.12 shows the imaged angular segment bounded by the half power beam width (HPBW) Ψ_{rs} of the receive subarrays. For elevation and azimuth patterns centered at ϑ_c and 0° , respectively, the extrema of the angles corresponding to the imaged area are

$$\vartheta_{\min/\max} = \vartheta_c \pm \Theta_{rs}/2 \quad (5.46)$$

$$\psi_{\min/\max} = \pm \Psi_{rs}/2. \quad (5.47)$$

Within the angular range $-\pi/2 \leq \psi_n \leq \pi/2$ the sin-function is monotone and if the first order ambiguity (i.e., $|\nu| = 1$) is outside the angular segment bounded by $\psi_{\min} \leq \psi_n \leq \psi_{\max}$ any higher order ambiguities will also be outside this angular segment. Hence, to avoid azimuth ambiguities it is sufficient to

⁸For a forward radar the range r_n is known after chirp compression. The elevation angle ϑ_n of a point scatterer is uniquely defined through the range r_n and the platform height z_n (also see discussion in section 5.4.1).

require that the first order ambiguity lies outside the angular segment

$$\psi_{\text{amb}, \nu=\pm 1} \notin \left[-\gamma \frac{\Psi_{\text{rs}}}{2}; +\gamma \frac{\Psi_{\text{rs}}}{2}\right] \quad , \quad \gamma \geq 1 \quad (5.48)$$

where γ is a *safety factor* which specifies how far outside the main beam the ambiguity can occur. For $\gamma = 1$ the first order ambiguity will be just at the edge, i.e., the -3 dB angle, of the main beam. For all practical purposes the value of γ can be set to $\gamma = 2$.

Using the worst case values for the azimuth and elevation angles, together with (5.45) and (5.48) gives an expression for the maximum allowable receiver spacing

$$\Delta y_{\text{r,max}} = \frac{\lambda}{\sin(\vartheta_c - \Theta_{\text{rs}}/2)} \cdot \frac{1}{\sin(\Psi_{\text{rs}}/2) + \sin(\gamma \Psi_{\text{rs}}/2)}. \quad (5.49)$$

5.6.2.2 Transmit Array

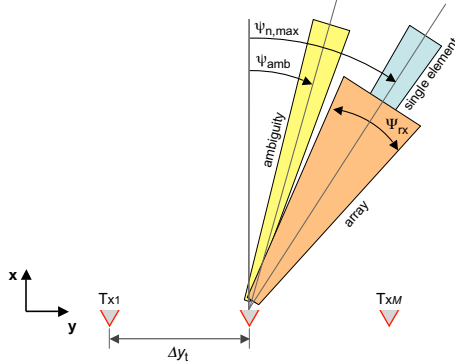


Figure 5.13: Transmit subarrays forming a uniformly spaced linear array. Each subarray is steered to a maximum angle $\psi_{n,\text{max}}$ and has an equivalent HPBW of Ψ_{rx} . The HPBW of the array is Ψ_{tx} .

Next, a similar approach is used to find an expression for the maximum Tx spacing. Investigating the first $\sin x/x$ in (5.44) gives an expression for the ambiguities

$$\sin \psi_n - \sin \psi_{\text{amb}, \nu} = \frac{\lambda}{\Delta y_t \sin \vartheta_n} \nu \quad ; \quad \nu \in \mathbb{Z} \quad , \quad \nu \neq 0 \quad (5.50)$$

However, unlike the receive array, each Tx subarray now has an *equivalent* HPBW of Ψ_{rx} and is steered to ψ_n as is depicted in Fig. 5.13. The reason for this somehow strange HPBW is that due to the product of the two $\sin x/x$ functions in (5.44) each Tx subarray can be thought of as consisting of N Rx elements having a HPBW of Ψ_{rx} . The pattern is no longer centered at $\psi = 0$ and the requirement for avoiding ambiguities becomes

$$\psi_{\text{amb}, \nu=\pm 1} \notin \left[\psi_n - \gamma \frac{\Psi_{\text{rx}}}{2}; \psi_n + \gamma \frac{\Psi_{\text{rx}}}{2} \right] \quad \text{where } \gamma \geq 1 \quad (5.51)$$

Solving (5.50) for $\Delta y_{t, \text{max}}$ using the above conditions yields⁹

$$\Delta y_{t, \text{max}} = \frac{\lambda}{\sin(\vartheta_c - \Theta_{\text{rs}}/2)} \cdot \frac{1}{\sin(\Psi_{\text{rs}}/2) - \sin(\Psi_{\text{rs}}/2 - \gamma\Psi_{\text{rx}}/2)} \quad (5.52)$$

5.6.2.3 Conclusion on Azimuth Ambiguities in Uniform Arrays

To conclude, for the special case of a uniform Tx/Rx array the following requirements have to be fulfilled in order to avoid ambiguities:

- The requirement for the receive array is that no ambiguities occur within the HPBW Ψ_{rs} of the *single receive subarray* (with safety factor $\gamma \geq 1$); the maximum allowable spacing Δy_{r} is given by (5.49).
- For the transmit array it is required that no ambiguities occur within the HPBW Ψ_{rx} of the *steered receive array* (again assuming a safety factor of $\gamma \geq 1$); the maximum allowable spacing Δy_{t} is given by (5.52).
- The maximum Tx and Rx subarray spacings $\Delta y_{t, \text{max}}$ and $\Delta y_{r, \text{max}}$, respectively, both depend on the azimuth HPBW of the single Rx element Ψ_{rs} , in addition the Tx subarray spacing is a function of Rx subarray spacing Δy_{r} through the variable Ψ_{rx} .
- The dependency of the HPBW of the receive array on the steering angle, i.e., $\Psi_{\text{rx}}(\psi_0)$ can be included by replacing Ψ_{rx} by $\Psi_{\text{rx}, \text{max}}$ in (5.52). However this dependency of the HPBW can usually be neglected.

⁹For the upper and lower bounds in (5.51) two values are obtained for $\Delta y_{t, \text{max}}$. However only the lower bound needs to be considered (the resultant $\Delta y_{t, \text{max}}$ is given in (5.52)), since: $\sin\left(\frac{\Psi_{\text{rs}}}{2}\right) - \sin\left(\frac{\Psi_{\text{rs}}}{2} - \frac{\gamma\Psi_{\text{rx}}}{2}\right) \geq \sin\left(\frac{\Psi_{\text{rs}}}{2} + \frac{\gamma\Psi_{\text{rx}}}{2}\right) - \sin\left(\frac{\Psi_{\text{rs}}}{2}\right) \vee \frac{\Psi_{\text{rs}}}{2} + \frac{\gamma\Psi_{\text{rx}}}{2} \leq \frac{\pi}{2}$.

- The results are valid for the case that the main beam in elevation does not cover the angle $\vartheta = 90^\circ$, i.e., $\pi/2 \notin [\vartheta_c - \Theta_{rs}/2; \vartheta_c + \Theta_{rs}/2]$, otherwise the $\sin(\vartheta_c - \Theta_{rs}/2)$ in (5.52) and (5.49) should be replaced by 1.
- The results were obtained under the presumption that $\Delta y_r \leq \Delta y_t$. Due to reciprocity the results can be used for $\Delta y_r > \Delta y_t$ as well by interchanging the transmit and receive arrays.

5.7 Simulator for Multi-Transmit/Receive Radar

A simulation and reconstruction tool was implemented in MATLAB[®] to investigate the performance of a real aperture radar. Using this tool it is possible to simulate the received signals for Tx and Rx subarrays placed at arbitrary positions and point scatterers located within a specified imaged area. Different image reconstruction algorithms can be tested on simulated received signals. The input parameters to the simulator are:

- position $\mathbf{x}_{t_i}, \mathbf{x}_{r_j}$ and number M, N of transmit and receive elements;
- chirp parameters: duration T_p , bandwidth B_w and center frequency f_0 ;
- position X_c, Y_c, Z_c and extent X_0, Y_0 of the imaged area;
- complex reflectivities of point scatterers (image function) $f(x, y)$.

Figure 5.14 shows a block diagram of the implemented reconstruction steps. The diagram makes use of the signal space to represent the dimensionality and independent variables of the signal. Thus, the raw input signal (upper right) is a function of the Tx and Rx antennas' positions and time. The first processing block implements the range compression using FFT and matched filtering in the frequency domain (see section 2.6). The matched filter is independent of the antenna's position and is represented by a 1D function. The near field correction (see section 5.3) involves computing the correction matrix (which is a function of the antennas' positions and the range), a change of variable from range to time, and an element-by-element multiplication by the range compressed data matrix. The resultant signal is still a function of time and antenna position. Next, a time-to-elevation angle mapping is implemented based

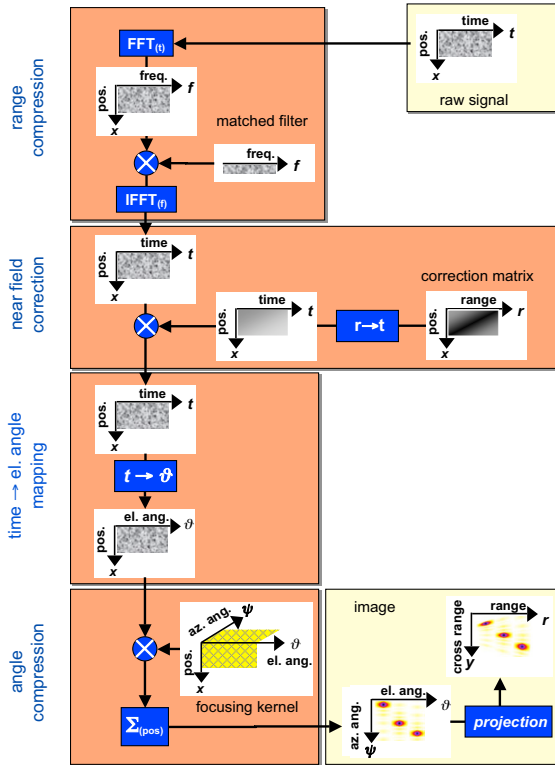


Figure 5.14: Block diagram of image reconstruction algorithm showing signal space.

on the known height of the radar platform (see discussion in section 5.4.1). The angle compression block involves the multiplication by the kernel and subsequent summation over all antenna positions. The compression kernel (see section 5.2) is a function of azimuth and elevation angles as well as the position of the antenna elements. The resultant data space is a function of azimuth and elevation angles. A final projection on the $z = -Z_c$ plane results in an image in Cartesian coordinates.

5.8 Verification

The simulator described in the previous section is used to verify the theoretical results and performance parameters derived earlier in this chapter. Further, the investigation of the processed images serves to get a better understanding of the capabilities of a real aperture radar utilizing multiple transmitters.

5.8.1 Transmit/Receive Resolution

In section 5.6 it was stated that both the Tx and Rx arrays contribute to the azimuth resolution of the forward radar. This was verified for the azimuth compressed signal and the special case of a uniform array. Fig. 5.15 illustrates this for the more general case of 2D processing, where Fig. 5.15(a) shows a distribution of point scatterers and Fig. 5.15(b) the resulting radar image.

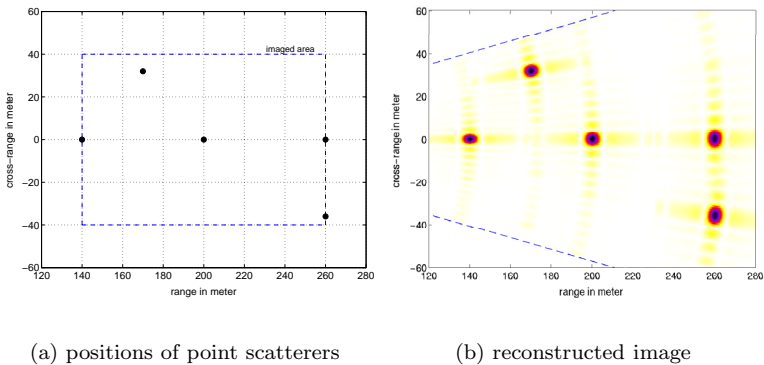


Figure 5.15: Position of point scatterers (a), and 2D reconstructed image using all transmit and receive arrays.

The corresponding system and image parameters are given in Table 5.1. Several properties typical for a forward radar are recognized from the figure: the azimuth resolution (vertical extent of the point scatterers in the image) deteriorates with increasing range, this is due to the fact that the *real* aperture radar has a fixed resolution with respect to the angle, which transforms into a

variable spatial resolution; although all point scatterers are distributed within a rectangular area of X_0 by Y_0 meters, the shape of the imaged area when displayed in spatial coordinates will be trapezoid, since it is really the angular segment bounded by the HPBW of the antennas which is imaged.

antennas	value	imaged area	value	chirp	value
M	6	X_0	120 m	f_c	9.6 GHz
Δy_t	7.2λ	Y_0	80 m	B_w	31 MHz
N	7	X_c	200 m	T_p	0.2 μ s
Δy_r	1λ	Y_c	0 m		
		Z_c	-30 m		
Notes: Linear uniform Tx/Rx array along y -axis. Five point scatterers.					

Table 5.1: The parameters for the simulations of Fig. 5.16.

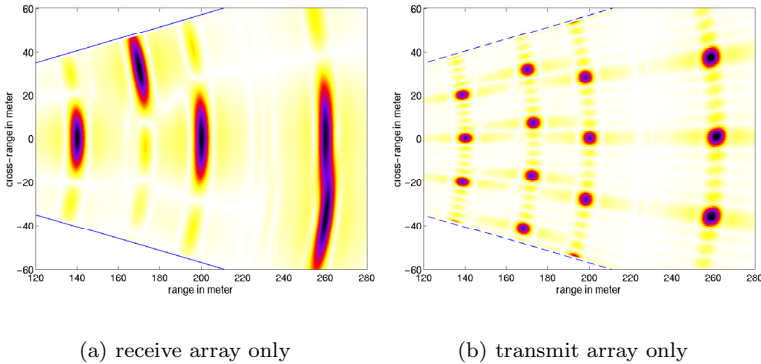


Figure 5.16: 2D reconstructed images using one Tx subarray together with all Rx subarrays (a), and all Tx subarrays together with one Rx subarray (b).

The reconstructed image (cf. Table 5.1 for parameters) resulting from processing only the Rx or the Tx array are shown in Fig. 5.16(a) and Fig. 5.16(b), respectively. The spacing between the elements of the Rx array is smaller than the corresponding spacing between the Tx elements, which results in a broader azimuth extent (resolution) of the point scatterers in Fig. 5.16(a). The large extent of the Tx array (as compared to the receive array) gives a high angular

resolution which, however, contains azimuth ambiguities as seen in Fig. 5.16(b).

An alternative interpretation of this is that the Tx array is used to obtain a high resolution (but ambiguous) image, while the Rx array is used to suppress the azimuth ambiguities. Using all Tx and Rx antennas for the processing will result in the image of Fig. 5.15.

5.8.2 Transmit/Receive Ambiguities

The effect of violating the conditions for the maximum spacing between the Tx and Rx elements is simulated for a system described in Table 5.2. For a given imaged area two parameters influence the appearance of azimuth ambiguities: the spacing between the Rx elements and the spacing between the Tx elements. Violating either one of the conditions derived in section 5.6.2 will result in azimuth ambiguities.

antennas	value [†]			imaged area	value	chirp	value
M	5	5	5	X_0	120 m	f_c	9.6 GHz
Δy_t	12λ	4.2λ	4.2λ	Y_0	80 m	B_w	31 MHz
$\Delta y_{t,\max}$	4.1λ	17.4λ	4.1λ	X_c	200 m	T_p	0.2 μs
N	5	5	5	Y_c	0 m		
Δy_r	1λ	4.2λ	1λ	Z_c	-30 m		
$\Delta y_{r,\max}$	1.3λ	1.3λ	1.3λ				
Notes:	Linear uniform Tx/Rx array along y -axis. Three point scatterers.						

[†]First column: Tx ambiguity, second column: Rx ambiguity, third column: no ambiguities.

Table 5.2: The parameters for the simulations of Fig. 5.17 and Fig. 5.18(b).

Figure 5.17 shows the processed image for three different spacings Δy_r and Δy_t while keeping $\Delta y_t > \Delta y_r$ in all cases¹⁰. Violating the condition for the Tx array, i.e., $\Delta y_t > \Delta y_{t,\max}$ results in ambiguities within the HPBW of the *receive* array as shown in Fig. 5.17(a). These ambiguities are additionally weighted by the pattern of the Rx array. On the other hand when the condition for the

¹⁰Although the Tx and Rx arrays can be interchanged without altering the resultant image, the conditions for avoiding azimuth ambiguities are different for the Tx and Rx arrays. This is in no violation to reciprocity, which merely requires the conditions to be interchanged together with their respective arrays.

spacing between the elements of the Rx array is violated, i.e., $\Delta y_r > \Delta y_{r,\max}$ the ambiguities are distributed over the image (bounded by the HPBW of the *single* element) as seen in Fig. 5.17(b). An ambiguous free image is obtained when both $\Delta y_t \leq \Delta y_{t,\max}$ and $\Delta y_r \leq \Delta y_{r,\max}$ which is shown in Fig. 5.18(b)

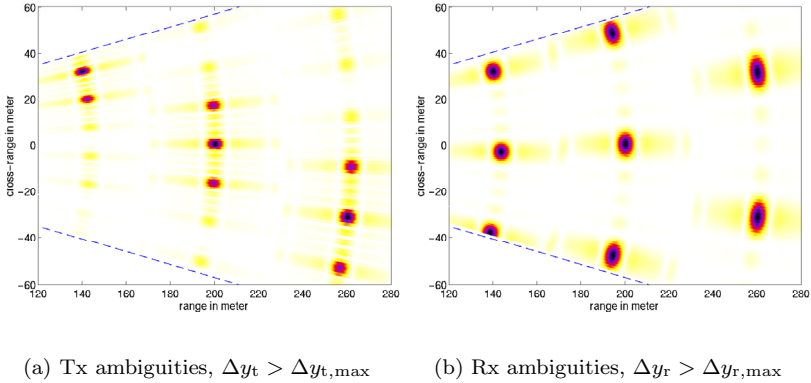


Figure 5.17: Influence of the spacing between elements on the azimuth ambiguities.

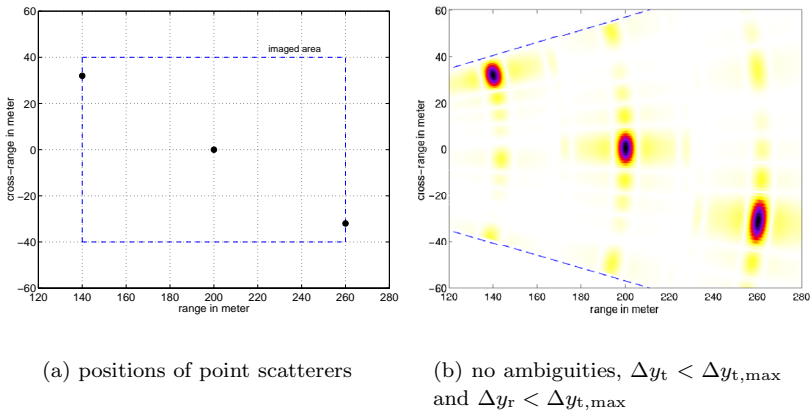


Figure 5.18: Position of point scatterers (a), and 2D Reconstructed ambiguous free image (b).

5.8.3 Near Field Correction

In section 5.3 it was stated that depending on the image and antenna system parameters a near field correction is required to compensate for the quadratic terms in the focusing kernel. The effect of the near field correction is shown in Fig. 5.19 for the system described in Table 5.3.

antennas	value	imaged area	value	chirp	value
M	9	X_0	60 m	f_c	9.6 GHz
Δy_t	19.3λ	Y_0	40 m	B_w	31 MHz
$\max\{ \mathbf{x}_t \}$	77.6λ	X_c	90 m	T_p	$0.2 \mu\text{s}$
N	9	Y_c	0 m		
Δy_r	1λ	Z_c	-10 m		
$\max\{ \mathbf{x}_r \}$	4.0λ				
Notes:	Linear uniform Tx/Rx array. Five point scatterers				

Table 5.3: The parameters for the simulations of Fig. 5.19.

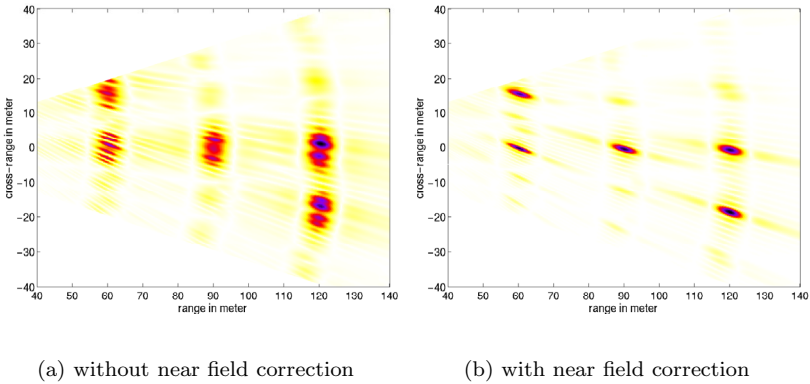


Figure 5.19: The influence of near field term in the azimuth focusing of the image.

Using (5.20) the allowable upper limit for the array extent¹¹ without near

¹¹Since $M = N$ the value is the same for the transmit and receive arrays.

field correction is calculated to be¹²

$$\sqrt{\frac{2R_{\text{near}}\gamma M}{\lambda}} = 1.4\lambda \quad (5.53)$$

for $\gamma = 0.055$, i.e., a maximum 1% image defocusing. As seen from Table 5.3 the actual array extent is above this limit and the corresponding processed image (see Fig. 5.19(a)) shows substantial degradation.

The upper limit for the array extent with near field correction is

$$R_{\text{near}}\sqrt{\frac{\gamma M}{\lambda|\Delta r|}} = 278\lambda \quad (5.54)$$

which is much larger than the actual array extent. The corresponding processed images is shown in Fig. 5.19(b) and shows no degradation.

5.8.4 Pulse Coded Chirp Waveforms

In the following the dual chirp operation described in section 5.5 is demonstrated for the radar system characterized in Table 5.4. Pulse coded chirp operations presumes a radar capable of transmitting two types of chirp waveforms and in addition convert them to different RF frequency bands. In the following simulations the point spread function (PSF) and the intensity image is used to evaluate the results.

First, a conventional single chirp multi-transmit/receive system, where the two transmitters are operated sequentially, i.e., at different time instances is simulated. Fig. 5.20 shows the resultant point spread functions and intensity image. This case is considered as the reference; the PSFs and intensity images of further simulation results will be normalized to the single chirp case.

Next, a system with two simultaneously transmitted identical chirp waveform is simulated. Such a system is of no practical relevance, it is only simulated for comparison purposes. From Fig. 5.21 it is seen that the two transmitted waveforms interfere and the resultant PSF shows two peaks instead of one. In

¹²The expression is reformulated to express the limit in terms of the wavelength.

antennas	value	imaged area	value	chirp	value
M	2	X_0	120 m	B_w	31 MHz
Δx_t	2.7λ	Y_0	120 m	T_p	$1.0 \mu\text{s}$
Δy_t	8.0λ	X_c	300 m		
Δz_t	1.5λ	Y_c	0 m		
N	11	Z_c	-60 m		
Δx_r	0.36λ	x_n	6 m		
Δy_r	1.0λ	y_n	-7.8 m		
Δz_r	0.1λ	z_n	-60 m		
Notes:	Linear uniform Tx/Rx array. One point scatterer.				

Table 5.4: System and imaged area parameters used in simulation.

addition the amplitude (intensity) of the peak is much lower than for the reference case. Physically, the simultaneous operation of both transmitters results in a total radiation pattern of the array formed by the two transmitters, which is different from the patterns of the individual transmit antennas. Mathematically, the poor image quality is due to the fact that the azimuth focusing kernel no longer corresponds to the complex conjugate of the signal received due to the point scatterer.

The simulation results for a system operating in true dual chirp mode is shown in Fig. 5.22 for the case of two inverse chirps occupying the same frequency band (according to section 3.4.2 the integrated range ambiguity ratio for this case is given by $IRAR_{u1d1}$) and transmitted simultaneously. Although the maximum intensity level is improved with respect to later case, the image still shows degradation. This is due to the high $IRAR$ level for this chirp configuration.

Next, a system with two *inverse* chirps occupying adjacent frequency bands is simulated ($IRAR_{u1d2}$). The resultant PSF in Fig. 5.23 shows nearly no degradation with respect to the reference (ideal) case of two sequential chirps as given in Fig. 5.20. Hence, such a system can be used in practice, without any notable image quality degradation.

Last, a system with two up-chirps occupying adjacent frequency bands ($IRAR_{u1u2}$) is simulated. As expected, the resultant PSF (see Fig. 5.24) is

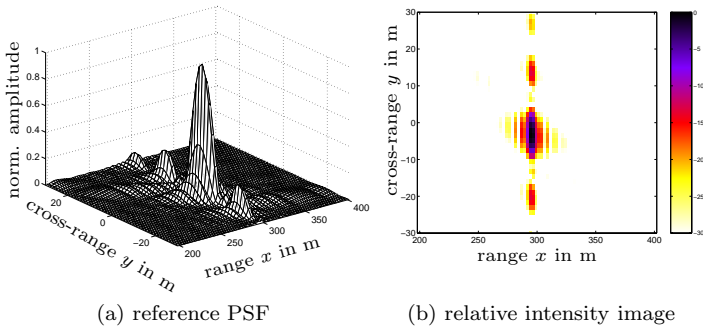


Figure 5.20: Simulation of reference system sequentially transmitting up-chirps.

improvement with respect to the previous case, due to the reduced *IRAR* level.

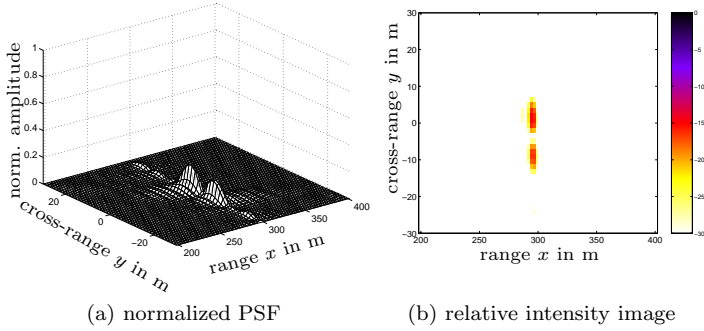


Figure 5.21: Simulation of a system with two up-chirps transmitted simultaneously.

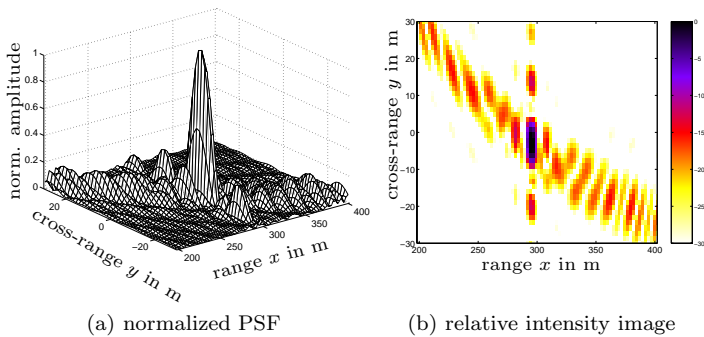


Figure 5.22: Simulation of dual chirp system using two inverse chirps occupying the same frequency band and transmitted simultaneously.

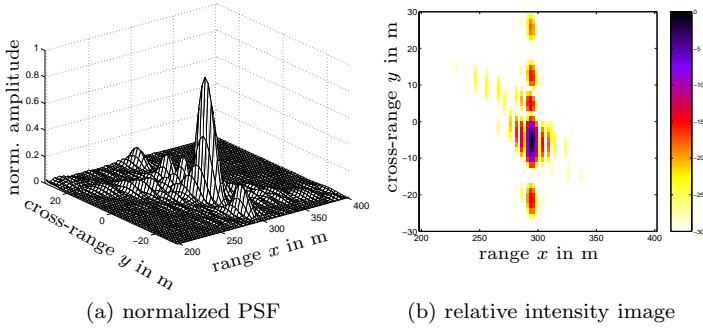


Figure 5.23: Simulation of a dual chirp system using two inverse chirps occupying adjacent frequency bands and transmitted simultaneously.

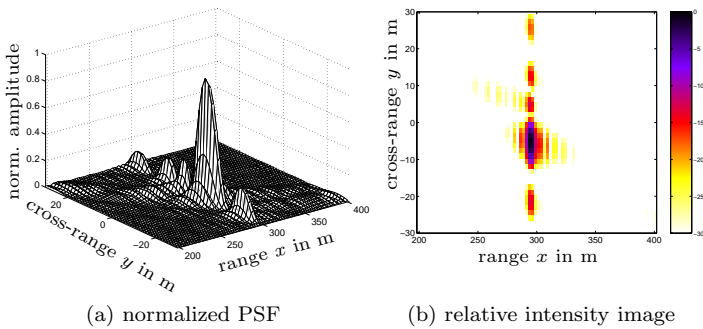


Figure 5.24: Simulation of a dual chirp system using two up-chirps occupying adjacent frequency bands and transmitted simultaneously.

6 Digital Beam-Forming Radar Demonstrator

This chapter describes a multi-receive real aperture radar build to demonstrate the digital beam-forming system concept and imaging capabilities. The radar system known as SIREV (**S**ector **I**maging **R**adar for **E**nhanced **V**ision) [59, 72, 104, 118, 124, 128] consists of a set of active antenna elements strapped rigidly to the carrier platform and operated by a radar receiver. The primary goal is to use DBF to supply high quality radar images of the sector in front of the aircraft, but the system may easily be adapted to supply images in any desired direction [43, 119].

The active antenna hardware implementation is flexible such that the system can be operated in various configurations. In its current implementation the antenna system is operated by a conventional SAR receiver [86]. Thereby, the passive antenna of a conventional airborne SAR is replaced by the active SIREV DBF antenna system. Although the system is mounted on a moving platform, it is evident that the SIREV setup cannot use the forward motion to obtain a synthetic aperture in across-track direction (see section 2.2). Thus, the SIREV system uses a real antenna array as described in chapter 5, instead of the virtual antennas generated in the SAR mode.

The chapter focuses on the active antenna hardware and the results of the demonstration flights. The next two sections describe the hardware system configuration and the geometry for the antenna placement. A detailed description of the active antenna and control hardware realized in the SIREV system is given in section 6.3. The integration of the complete SIREV system in the helicopter is described in section 6.4. The flight campaigns and the resultant processed images is dealt with in section 6.5. Finally, section 6.6 states further possible applications of the SIREV system.

6.1 The Hardware System Configuration

According to the DBF principle (see chapter 2) the system consists of two separate subsystems for transmission and reception. As shown in Fig. 6.1 one transmitting horn antenna and a array of patch subarrays operating in X-band are used. To minimize the demands on the hardware, the receiving antennas are sequentially switched, thus effectively only one element is *active* during the time the radar is “listening” to the echo of one transmitted pulse. The signals received by the active element are amplified and connected to the receiver through the switching matrix. In the receiver the signals are further amplified, filtered, down converted and A/D converted. The data is then stored for later off-line processing.

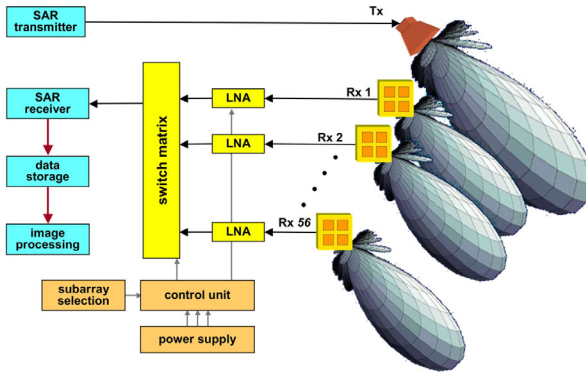


Figure 6.1: The SIREV hardware system concept.

It is evident that the switching approach enables a cost-efficient implementation, since only one receiver and A/D converter is needed. This is the main difference to the DBF system concept given in section 2.1 which would require 56 receivers and A/D converters for simultaneous data acquisition. In general the switching concept for DBF is preferable, whenever the imaged scene changes slowly with respect to the switching interval between the antennas. This is the case for the SIREV system, since it is mounted on a —relatively slow moving— helicopter. It should be noted, that the *sequential* switching of the antenna elements is not an essential aspect of the SIREV principle. The

elements can also be switched randomly or synchronously as long as this is taken into account during the following beam-forming process.

The principal idea of the SIREV system is to keep the radar hardware, including front-end and antenna, comparatively simple and to implement the digital beam-forming by processing the radar raw data for image formation on a computer.

6.2 The SIREV Geometry

In the following, the SIREV geometry shown in Fig. 6.2 is considered. The transmit antenna is centered at across-track position $y_t = 0$ with a vertical offset $z_t = z_{\text{offset}}$. The linear and uniform receive array consists of 56 subarrays, oriented horizontally and orthogonal to the flight direction. The receive subarrays are distributed around $y_{rc} = 0$ on the y -axis with a spacing of $\Delta y_r = 1.6\lambda$. The total receive array length is 2.8 m.

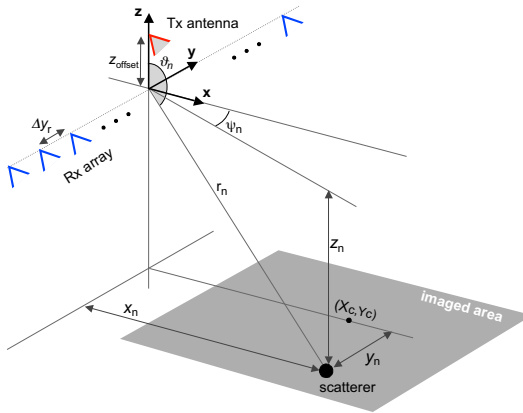


Figure 6.2: Bi-static SIREV geometry.

Cross-track resolution (corresponding to the azimuth direction) is achieved by correlation of the received signals of each antenna element with the appropriate focusing kernel. The forward velocity of the aircraft is, for the most part not relevant for the beam-forming. This is the case, since the relative

aircraft displacement between successive transmitted pulses is negligible. The maximum achievable resolution in the azimuth direction depends on the total length L_{ant} of the antenna array (see section 5.6) and decreases with range r_n . It can be increased only by the use of a shorter wavelength λ or an extension of the length of the array. For a single transmit antenna the azimuth resolution δy is

$$\delta y = \frac{\lambda \cdot r_n}{L_{\text{ant}}} \quad (6.1)$$

Improved azimuth resolution can be obtained if multiple transmit antennas were used to increase the effective length of the array as described in section 5.6. For example two transmit antenna could be placed at both ends of the receive array to double the effective length. Further, it is not necessary to place the antenna array along a straight line. A conformable implementation, which fits the shape of an airframe, for example, is feasible.

6.3 The Active Antenna and Control Hardware

The antenna system consists of one high power horn antenna for transmission and 56 receiving aperture coupled microstrip patch subarrays [124, 83, 64]. The transmitting antenna and each of the receiving subarrays are horizontally polarized and have the same angular coverage. The operating frequency and bandwidth are 9.55 GHz and 400 MHz, respectively.

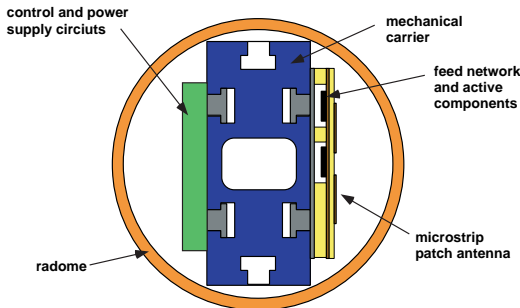


Figure 6.3: Side view of antenna system.

A side view of the system is shown in Fig. 6.3. For environmental protection the antenna is placed inside a PVC pipe forming the radome. The front side of the active antennas consists of the RF hardware and radiating patches. In order to achieve high efficiency along with a compact design and to reduce the noise figure, the active RF-circuits (switches and LNAs) are integrated within the feed network of the receiving antennas [125]. The active components are well shielded from the radiating patches through the large ground plane which contains the coupling slots. The control circuits consisting of voltage converters, signal decoding circuits and active temperature regulators [111, 110] are mounted on the back side of the mechanical carrier.

The RF interface to the antenna system consists of one connector for the transmitting antenna, and one connector for the receive subsystem. In addition one power supply connector and the interface for the digital control signals is required.

6.3.1 Modular Concept

A modular concept was adopted, placing eight subarrays on a common RF-unit (see Fig. 6.4). Each unit has one RF-output and a connector for the power supply and control signal inputs. A corresponding control-unit for each RF-unit is placed on the back of the mechanical carrier.

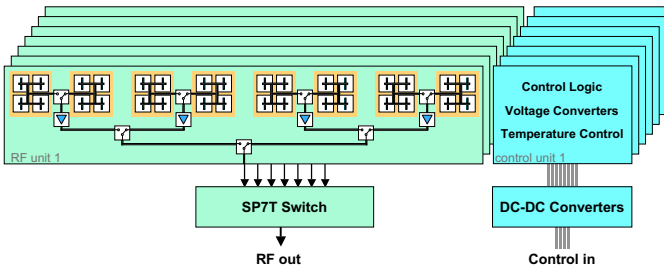


Figure 6.4: Block diagram of antenna system.

As shown in the block diagram of Fig. 6.4, the currently active subarray on each board is selected using three levels of single-pole double-through (SPDT)

switches. The first switch level is followed by low noise amplifiers (LNA) providing a gain of 14 dB. Placing the LNAs after the first switch level is a compromise between the number of LNAs needed as well as space requirements on the one hand and noise figure on the other. The layered structure consisting of the mechanical carrier, the feed network with the integrated active components (LNAs and switches) and the radiating patches is shown in Fig. 6.5.

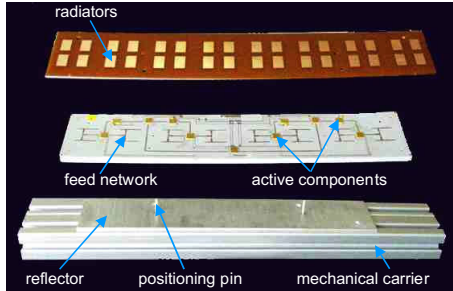


Figure 6.5: RF-unit consisting of radiating patches, feed network, active components, placed on the mechanical carrier.

6.3.2 Transmitting Subsystem

The transmitting subsystem consists of a horn antenna centered along the array and installed outside the radome. The horn antenna was designed to yield a HPBW of 40° in elevation and 38° in azimuth. The horn is protected by a separate radome, which is optimized so as to minimize the effect on the antenna match.

6.3.3 Receiving Subsystem

The receiving subsystem consists of 56 subarrays, where each subarray is formed by combining four single patch elements into a 2×2 subarray by a passive microstrip network. Aperture coupling with slots is used to couple the energy from the feed network to the radiating patches. The LNAs and SPDT switches

are integrated within the feed network of the receive antenna. Fig. 6.6 shows the feed and slot layer of one RF module.

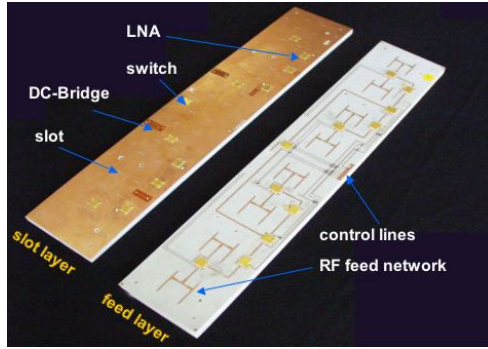
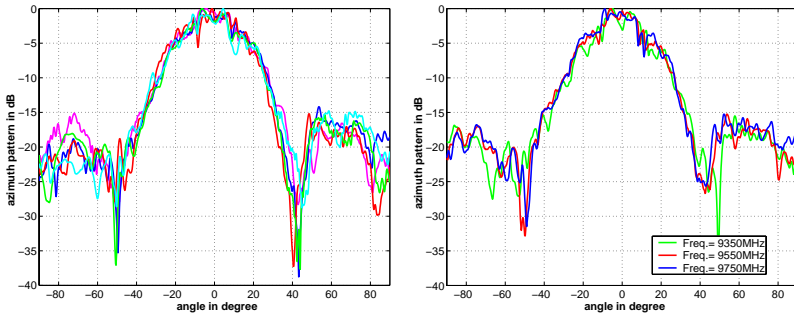


Figure 6.6: The two layers of the RF module containing the feed network, LNAs, and switches on one side, and the radiating slots and DC bridges on the other.



(a) patterns of five different subarrays at 9.55 GHz

(b) single subarray's pattern 9.35 GHz, 9.55 GHz, and 9.75 GHz

Figure 6.7: Measured azimuth (E-Plane) radiation patterns of the receive subsystem.

The azimuth radiation patterns of five representative subarrays distributed along the antenna are shown in Fig. 6.7(a). The antenna patterns of one subarray measured at different frequencies are shown in Fig. 6.7(b). It can be seen that the patterns show a ripple over azimuth angle. The ripple is caused

by coupling between the individual subarrays, reflections from the radome and electromagnetic interaction with the large metal carrier used for mounting the antenna, where the later causes the greatest contribution to the ripple. The signals from all subarrays are involved in the processing, hence the pattern is effectively averaged over the elements. As long as the peaks of the ripple for all the subarrays do not coincide, their contributions are insignificant for all practical purposes.

6.3.4 The Control and Power Unit

Each RF unit has its corresponding control unit to generate the required power levels and the driving signals of the switches. Fig. 6.8 shows a control unit placed on the bottom side of the mechanical carrier. The control units are buffered and connected to each other to form a modular system which can be extended with the number of antennas used. The subarrays can be switched with a *PRF* of up to 50 kHz without any degradation of the driving signals over the whole antenna length.

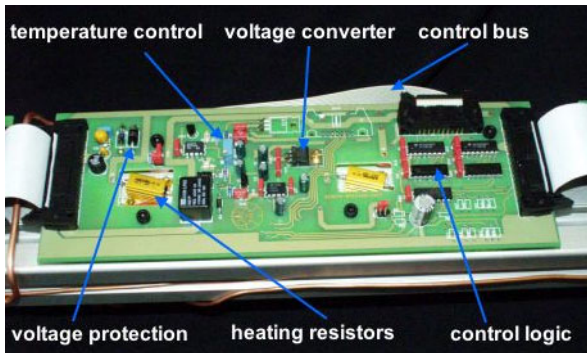


Figure 6.8: Control unit consisting of Power supply, control signal generation circuit and heating system all placed on one board.

6.3.4.1 The Driving Circuit

The driving part of the unit is built in analog and CMOS technology, and can be divided into two main parts. The first part is an analog negative and positive voltage generator to drive the transistor gates of the SPDT switches. These voltages have to be very stable, however, the currents drawn by the SPDTs are also very small. The power levels for the LNAs are also generated within the driving circuit.

The second part of the control unit is the matrix decoding. This digital part is required for multiplexing the SPDTs. The driving bits set by the radar equipment on the aircraft are buffered and converted to the negative and positive SPDT driving levels to switch the channels.

6.3.4.2 The Heating System

A heating system is included in the active antenna. This facilitates operation at high altitudes and severe weather conditions.

To reach high efficiency for the heating system, the heating power is directly drawn from the aircraft power supply without any conversion. Therefore both the RF and data ground are strictly decoupled from the aircraft ground. An individual temperature regulator including a temperature sensor and two heating elements is implemented on each control unit. This allows the temperature regulators to react individually to the temperature profile of the carrier, ensuring a homogeneous heating of the whole antenna system. The maximum heating power is 130 W, thus the maximum current consumption is about 4.5 A, which is the maximum current allocated by the aircraft's power supply for the heating system.

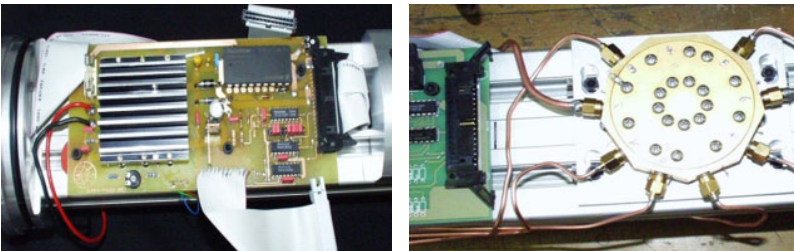
One additional temperature sensor is fixed onto the mechanical carrier and is directly connected to the radar receiver on the aircraft. Thus the system temperature can continuously be monitored from the aircraft during system operation.

6.3.4.3 The Power Unit

The power module inside the pipe is able to handle the common airplane's supply voltage of 28 V DC. The DC-DC converters used are very efficient, thus the current required from the aircraft for the operation of the control and RF hardware does not exceed 1 A (not including the heating system). Fig. 6.9(a) shows a top view of the power module fixed on the bottom side of the carrier.

6.3.5 Central RF Switch

To select one of the seven RF units one central single-pole seven-through switch (SP7T) is placed on the bottom side of the mechanical carrier. The SP7T is a pin diode switch with integrated channel drivers, thus the switch can directly be driven by TTL signals. The required interface to decode the seven channels out of the control bits is placed next to the switch. Fig. 6.9(b) shows the SP7T and the coaxial SMA connections to the seven RF units and the single RF output.



(a) power unit

(b) central switch (SP7T)

Figure 6.9: DC-DC converters to generate the voltage levels and the central switch.

6.4 Integration into the Helicopter

The SIREV demonstrator has been integrated in a BO 103 helicopter. The SAR receiver system AeS-1 [86, 116] is placed inside the helicopter (see Fig. 6.10). A specially constructed holding device is used to fix the active antenna onto the fuselage of the helicopter as shown in Fig. 6.10. The transmit antenna is fixed outside the radome of the receive array.



Figure 6.10: Active antenna and SAR receiver mounted on the helicopter.

6.5 Flight Campaigns and Image Data Analysis

Two flight campaigns have been carried out in the vicinity of Oberpfaffenhofen, Germany. The main objective of the first campaign was to verify the functionality of the components using a large corner reflector, contained in the scene as the main scattering element. During the second campaign large data-sets in static and dynamic flight operation have been acquired during a flight across the river “Lech”. The recording parameters of the flight campaign used for data collection are summarized in Table 6.1.

Parameter		value
center frequency	f_c	9.55 GHz
chirp bandwidth	B_w	100 MHz
antenna length	L_{ant}	2.85 m
number of receive elements	N	56
pulse repetition frequency	PRF	14793 Hz
chirp duration	T_p	1.3 μ s
average helicopter velocity	V	28 m/s
average ground level	Z_c	556 m to 645 m

Table 6.1: Recording parameters of the two flight campaigns carried out over the river “Lech”. A corner reflector has been deployed for calibration.

As the helicopter moves forward, a large number of measurements are taken from a permanently changing sensor position. The frame rate is $f_{\text{frame}} = PRF/N$ where PRF is the pulse repetition frequency and $N = 56$ are the number of receive subarrays. If one image would be generated from each frame, the frame rate would be equal to the image rate f_{image} . During the flight campaign the PRF was set to 14792.9 Hz which yields an image rate of $f_{\text{image}} = 264.15$ Hz. Such a repetition rate by far exceed the critical fusion frequency of the human visual system (the eye), which is in the order of 50 Hz. The extra information was used to enhance the individual images through various averaging techniques.

To verify the digital beam-forming hardware concept, the SIREV data was processed by the Institut für Hochfrequenztechnik und Radarsysteme of the Deutsches Zentrum für Luft- und Raumfahrt [29, 59]. In the following, an overview over some of the processed images is given. The radar images are displayed in terms of a 2D Cartesian slant-range geometry (see geometry in section 3.3), where the time coordinate corresponds to the distance between the main antenna axis and the imaged object, while the angular coordinate is given by the object’s position in azimuth.

Measured Responses of Corner Reflector

Figure 6.11 shows a 3D surface plot of the set of focused data for a corner reflector, extracted for a sequence of 10 000 frames. A phase correction function was used to compensate for the phase discontinuities between signals from different antenna elements¹. From the temporal sequences of the azimuth profiles it becomes apparent that the focusing is almost independent of both azimuth angle and time, i.e., frame number. The changing azimuth position of the corner reflector is due to the helicopters movement.

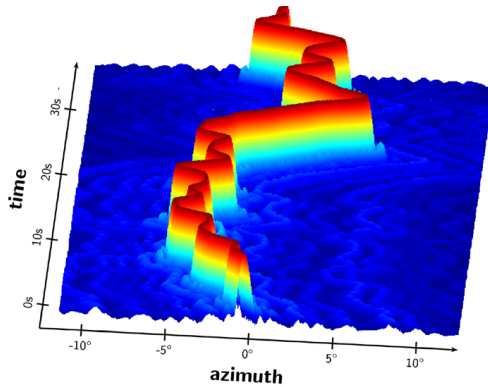


Figure 6.11: Temporal sequence of normalized corner reflector responses [59].

Measured “Lech” River Scene

A processed scene resulting from measurements during the second flight campaign is shown in Fig. 6.12. The images obtained from processing individual frames show substantial noise contamination. This effect is seen in Fig. 6.12(a) for one processed image. The effect of “thermal noise” (see section 2.3.1) can be substantially reduced through averaging over several successive frames [59]. This is especially useful in the context of SIREV where —due to the high

¹The phase compensation function used to account for the *systematic* phase shift due to the receive antenna hardware is not related to the *phase correction function* introduced in section 5.3, which is due to the near field effect.

frame rate f_{frame} — a large number of independent processed frames are available within a short time interval. Fig. 6.12(b) shows the same “Lech” river scene which results after complex averaging.

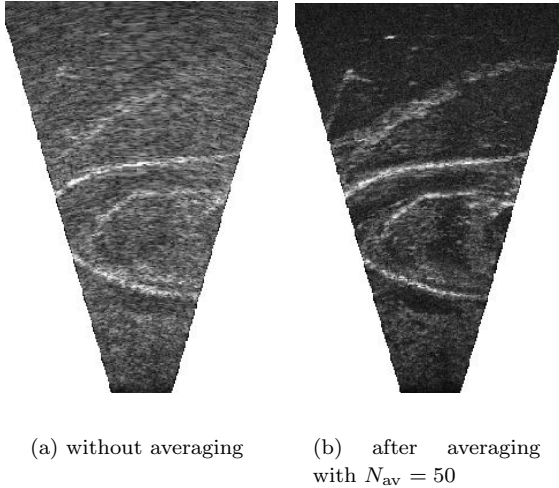


Figure 6.12: SIREV image of the “Lech” river [59].

6.6 Conclusion and Further Possible Applications

The hardware realization of the SIREV system and the successful flight campaigns confirm the superb performance of the digital beam-forming concept for radar. The developed radar system is based on a highly modular concept. With the given active antenna features any radar system with digital beam-forming (in X-band) can be realized. This makes it especially valuable for prototype experiments and performance analysis. The same hardware can be used for a digital beam-forming SAR demonstrator. The subsystems themselves are planar, light weight, low cost with excellent features concerning subarray beam characteristics, switching and temperature and environmental stability.

With the developed subsystems the features of digital beam-forming with increased spatial resolution is investigated while simultaneously a high coverage is maintained. Compared to analog beam-forming (T/R modules) a significant improvement in cost, weight, power consumption, noise figure and coverage is achieved.

One advantage of the SIREV concept is that imaging does not require platform movement, which allows the system to be adapted to supply images in any desired direction [43, 119]. Besides a map of the earth's surface a sequence of SIREV images can be further processed to supply additional information about the topography and rapid temporal changes of the underlying terrain [120].

The SIREV concept may, in addition be used for differential interferometry to measure displacements in the order of centimeters or less using a static antenna array [42]. The line-of-sight displacement can be measured by evaluating the phase change as a function of time. This is an attractive concept for monitoring land slides or water dams.

Another interesting application for the SIREV concept is the monitoring of oil spills on the ocean, where an airborne SAR system with left and right side-looking capability can be combined with a SIREV system, allowing complete imaging of the ocean surface without gaps [61, 117, 119]. Further examples of applications for the SIREV principle are high resolution cloud radars [108, 25] (static or airborne systems), collision avoidance airport traffic monitoring over taxi-way and radars for detecting bird swarm during the aircraft landing.

7 Conclusions

The launch of the German TERRASAR-X remote sensing satellite in 2006 will open a new era in the application of radar remote sensing. For the first time there is a change from data products to information products, aimed for the commercial and public markets. This mission marks a clear move from serving the military and scientific community to supplying the commercial market. It is anticipated that the versatility of needs for remote sensing information products will provide a non-negligible funding for this and similar future missions. At the same time it is, however, this versatility of needs being the shortcoming of current radar remote sensing systems. Up-to-date satellite systems are strongly confined towards a handful of possible applications. Technical solutions part with two clear trends: on one side there is a move towards systems dedicated to a single application; while on the other side, the solution is found by constructing very complex remote sensing systems providing a large number of mutually exclusive operation modes, each of which is dedicated to a certain purpose. Although the second approach offers a certain flexibility, it is at the cost of extremely sophisticated, low efficiency, high weight and high cost vulnerable hardware realizations based to a large extend on analog RF technologies. One common handicap of both trends is that the systems are bound to contradicting requirements on resolution and coverage.

The underlying work presents a comprehensive solution to the above mentioned shortcomings which is based on digital beam-forming (DBF). Further the same novel concept is investigated in the context of real aperture imaging radar. It shows that the digital beam-forming concept provides substantial performance improvement with respect to state-of-the-art systems, while reducing the requirements on the RF hardware.

The emphasis of the work is on the following points:

- introducing the concept and operation of a DBF radar;
- deriving the performance parameters of synthetic and real aperture DBF radar;
- establishing the processing algorithms necessary for image reconstruction; and
- hardware implementing of a demonstrator for DBF radar.

Digital beam-forming requires a completely new view on SAR systems, the mathematical and system-theoretical groundwork of which are established in this work. The developed analytic expressions allow, for the first time, an easy performance optimization for a multiplicity of system parameter sets. Moreover, it is demonstrated that the various operation modes of state-of-the-art systems turn out to be dispensable. This is because digital beam-forming inherently implements an arbitrary number of *simultaneous* operation modes. Thus, the aim of high resolution and wide swath SAR can finally be reached.

The advancement of SAR system is strongly related to the development of highly efficient processing algorithms. Any DBF SAR system requiring the reinvention of all processing techniques is equivalent to a regression. The presented work overcomes this difficulty by developing processing algorithms which can easily be integrated into existing processing codes, while at the same time maintaining the benefits of DBF SAR. These algorithms are implemented in a novel SAR simulation tool which is then used to verify both the DBF SAR performance parameters as well as the processing algorithms.

In contrast to synthetic aperture radar which is mainly used in a side-looking configuration, real aperture radar can, in addition, be used in forward-, backward- or downward-looking configurations. Although real aperture imaging radar with multiple receive antennas is well known, it is not widely implemented due to its limited resolution as compared to a SAR. Within the work it was shown that the digital beam-forming concept when used with multiple transmit/receive antennas can be exploited to dramatically increase the resolution. The work, for the first time establishes mathematical principles by adopting an analogy from antenna array theory to explain the performance of multi-transmit/receive real aperture radar. The emphasis is to derive closed expressions for the system and resulting performance parameters for a general configurations dictated by the carrier platform. Within this framework, a

multi-transmit/receive real aperture radar simulation tool was developed. The simulator was then used to verify the theoretical results obtained earlier.

An issue profitable both for real and synthetic aperture radar is the utilization of pulse coding. The work shows, how multiple chirp waveforms can be used, either to reduce the measurement time for real aperture radar, or to increase the swath width of a synthetic aperture radar. The novel treatment of the subject shows, that multiple chirps can be used for imaging permanent scatterers with a high potential for distributed scatterer imaging radar. The results are considered as a motivation for further studies.

The progressive treatment in the underlying work is aimed to direct the development strategy of radar remote sensing towards systems utilizing digital beam-forming. The future of imaging radar are cooperative and distributed systems which will enable cost-efficient implementations, outperforming state-of-the-art synthetic aperture radar. These system are based on bi- or multi-static antenna configurations for which digital beam-forming is mandatory. Thus, the development of digital beam-forming inherently includes applications such as transmitters of opportunities, sparse arrays imaging, and the use of geostationary communication satellites for radar imaging. Combined, this allows future imaging radar systems to simultaneously provide different end-users with high quality information products depending on their need. This way digital beam-forming will open the way for completely new, enhanced application in radar remote sensing.

Bibliography

- [1] M. M. Abousetta and D. Cooper, “On the use of some FMCW transmission schemes for radar angular resolution improvement,” in *Proc. International Radar Conference*, vol. 1, 1992, pp. 335–339.
- [2] M. Abramowitz and I. A. Stegun, *Handbook of Mathematical Functions*. New York: Dover Publications Inc., 1972.
- [3] J. Andersen, “Array gain and capacity for known random channels with multiple element arrays at both ends,” *IEEE Journal on Selected Areas in Communications*, vol. 18, no. 11, pp. 2172–2178, Nov. 2000.
- [4] S. R. J. Axelsson, “Suppressed ambiguity in range by phase-coded waveforms,” in *Proc. Int. Geoscience and Remote Sensing Symposium IGARSS’01*, vol. 5, 2001, pp. 2006–2009.
- [5] C. A. Balanis, *Advanced Engineering Electromagnetics*. John Wiley, 1989.
- [6] C. A. Balanis, *Antenna Theory Analysis and Design*. John Wiley, 1997.
- [7] R. Bamler, “A comparison of range-Doppler and wavenumber domain SAR focusing algorithms,” *IEEE Transactions on Geoscience and Remote Sensing*, vol. 30, no. 4, pp. 706–713, July 1992.
- [8] R. Bamler, *Mehrdimensionale lineare Systeme*. Springer-Verlag, 1998.
- [9] P. Barton, “Digital beam forming for radar,” *IEE Proceedings*, vol. 127, no. 4, Aug. 1980.
- [10] D. Belcher and C. Baker, “High resolution processing of hybrid strip-map/spotlight mode SAR,” *IEE Proceedings for Radar, Sonar and Navigation*, vol. 143, no. 6, pp. 366–374, 1996.

- [11] M. Bockmair, “Mikrowellenabbildung im Nahbereich,” Ph.D. dissertation, Lehrstuhl für Mikrowellentechnik der Technischen Universität München, 1989.
- [12] E. Bosch, H. Rothacker, and A. Jaeger, “High efficient, low power C- and Ku-band travelling wave tubes for satellite application,” in *Proc. Third IEEE Int. Vacuum Electronics Conference IVEC’2002*, vol. 1, Apr. 2002, pp. 186–187.
- [13] H. M. Braun, “Hochauflösendes SAR auf kleinsatelliten,” in *Workshop Radar and Communication RADCOM’2004*, Hamburg, Germany, Feb. 2004.
- [14] L. E. Brennan and I. S. Reed, “Theory of adaptive radar,” *IEEE Transactions on Aerospace and Electronic Systems*, vol. 9, no. 2, pp. 237–252, Mar. 1973.
- [15] N. Brenner, “Fast Fourier transform of externally stored data,” *IEEE Transactions on Audio and Electroacoustics*, vol. 17, no. 2, pp. 128–132, June 1969.
- [16] S. C. Bundy, “Noise figure, antenna temperature and sensitivity level for wireless communication receivers,” *Microwave Journal*, vol. 41, no. 3, pp. 108–116, Mar. 1998.
- [17] G. D. Callaghan, “Wide-swath space-borne SAR: Overcoming the trade-off between swath-width and resolution,” Ph.D. dissertation, University of Queensland’s, 1999.
- [18] G. D. Callaghan and I. Longstaff, “Wide-swath space-borne SAR and range ambiguity,” in *Proc. Radar Conference, RADAR’97*, Oct. 1997, pp. 248–252.
- [19] G. D. Callaghan and I. Longstaff, “Wide-swath space-borne SAR using a quad-element array,” *IEE Proceedings for Radar, Sonar and Navigation*, vol. 146, no. 3, pp. 155–165, 1999.
- [20] G. Carrara, R. Goodman, and R. Majewski, *Spotlight Synthetic Aperture Radar*. Norwood, MA: Artech House, 1995.

-
- [21] R. E. Collin, *Antennas and Radiowave Propagation*. McGraw-Hill, 1985.
- [22] J. C. Curlander and R. N. McDonough, *Synthetic Aperture Radar: Systems and Signal Processing*. New York: John Wiley, 1991.
- [23] A. Currie and M. Brown, "Wide-swath SAR," *IEE Proceedings for Radar, and Signal Processing*, vol. 139, no. 2, pp. 122–135, 1992.
- [24] G. Davidson and I. Cumming, "Signal properties of spaceborne squint-mode SAR," *IEEE Transactions on Geoscience and Remote Sensing*, vol. 35, no. 3, pp. 611–617, May 1997.
- [25] D. de Wolf, W. Russchenberg, and L. Ligthart, "Radar reflection from clouds: Gigahertz backscatter cross sections and Doppler spectra," *IEEE Transactions on Antennas and Propagation*, vol. 48, no. 2, pp. 254–259, Feb. 2000.
- [26] S. Demir and C. Toker, "Optimum design of feed structures for high G/T passive and active antenna arrays," *IEEE Transactions on Antennas and Propagation*, vol. 47, no. 3, pp. 443–452, Mar. 1999.
- [27] J. B. Detlefsen, "Imaging applications of millimeter wave sensors in robotics and road traffic," in *Proc. IEEE Microwave Systems Conference, NTC'95*, vol. 1, 1995, pp. 115–124.
- [28] J. Dias and P. Marques, "Multiple moving target detection and trajectory estimation using a single SAR sensor," *IEEE Transactions on Aerospace and Electronic Systems*, vol. 39, no. 2, pp. 604–624, Apr. 2003.
- [29] "SIREV: development of a functional model," Deutsches Zentrum für Luft- und Raumfahrt (DLR), Oct. 2000, final report.
- [30] "Strategische Ausrichtung für Raumgestützte Radar-Instrumente, SAFARI," Deutsches Zentrum für Luft- und Raumfahrt (DLR-HR), Astrium GmbH, Institut für Höchstfrequenztechnik und Elektronik (IHE), Nov. 2002, executive summary report.
- [31] G. Duchossois and S. Brouzzi, "SAR evolution and user needs in the post-Envisat time frame," in *Proc. Int. Geoscience and Remote Sensing Symposium IGARSS'95*, vol. 3, July 1995, pp. 1831–1833.

- [32] T. Einstein, "Realtime synthetic aperture radar processing on the RACE multicomputer," Mercury Computer Systems, Application Note 230.0, 1996. [Online]. Available: <http://www.mc.com/literature/>
- [33] R. Elachi, *Spaceborne Radar Remote Sensing: Applications and Techniques*. New York: IEEE Press, 1988.
- [34] J. H. G. Ender, "Space-time processing for multichannel synthetic aperture radar," *IEE Electronics & Communication Engineering Journal*, vol. 11, no. 1, pp. 29–37, Feb. 1999.
- [35] J. H. G. Ender and A. R. Brenner, "PAMIR – a wideband phased array SAR/MTI system," *IEE Proceedings for Radar, Sonar and Navigation*, vol. 150, no. 3, pp. 165–172, June 2003.
- [36] J. H. G. Ender and A. R. Brenner, "High-resolution radar imaging by means of a versatile radar platform," *Frequenz Journal of Telecommunications*, vol. 56, no. 9-10, pp. 85–90, Sept. 2002.
- [37] (2002, Dec.) ASAR product handbook. European Space Agency. [Online]. Available: <http://envisat.esa.int/dataproducts/asar/CNTR.htm>
- [38] O. Föllinger, *Laplace- und Fourier-Transformation*. Hüthig, 1990.
- [39] G. Franceschetti and R. Lanari, *Synthetic Aperture Radar Processing*. CRC Press, 1999.
- [40] G. Franceschetti and G. Schirinzi, "A SAR processor based on two-dimensional FFT codes," *IEEE Transactions on Aerospace and Electronic Systems*, vol. 26, no. 2, pp. 356–366, Mar. 1990.
- [41] A. Freeman, W. Johnson, B. Huneycutt, R. Jordan, S. Hensley, *et al.*, "The 'Myth' of the minimum SAR antenna area constraint," *IEEE Transactions on Geoscience and Remote Sensing*, vol. 38, no. 1, pp. 320–324, Jan. 2000.
- [42] A. K. Gabriel, R. M. Goldstein, and H. A. Zebker, "Mapping small elevation changes over large areas: differential radar interferometry," *Journal of Geophysical Research*, vol. 94, no. B7, pp. 9183–9191, July 1989.

- [43] C. H. Gierull, "Combining the idea of a downward-looking with a forward-looking airborne imaging radar," in *Proc. European Conference on Synthetic Aperture Radar EUSAR'2000*, vol. 1, Munich, Germany, May 2000, pp. 377–380.
- [44] R. Girard and P. Park, "Technical note on coded waveforms for SAR range ambiguities reduction," ESA/ESTEC, MPB Technologies Inc., Tech. Rep. 11649/95/NL/NB MPBT S.O. 482S, 1998.
- [45] W. Hackbusch, H. R. Schwarz, and E. Zeidler, *Teubner Taschenbuch der Mathematik*. B.G. Teubner Verlag, 1996.
- [46] U. Hackenberg, M. Adolph, H. Dreher, K. Ott, R. Reber, *et al.*, "Polarisation agile, highly accurate T/R-module for synthetic aperture radar," in *33rd European Microwave Conference (EuMC)*, vol. 2, Munich, 2003, pp. 875–878.
- [47] F. J. Harris, "On the use of windows for harmonic analysis with the discrete Fourier transform," *Proceedings of the IEEE*, vol. 66, no. 1, pp. 51–83, Jan. 1978.
- [48] C. Heer, "Wide swath high resolution SAR," Astrium GmbH, Tech. Note SAFARI-TN-AST-05, Aug. 2002.
- [49] C. Heer, K. Dumper, and B. Grafmüller, "SAR antenna beam pattern optimisation," in *Proc. Int. Geoscience and Remote Sensing Symposium IGARSS'00*, vol. 5, Honolulu, Hawaii, July 2000, pp. 2263–2265.
- [50] C. Heer, F. Soualle, R. Zahn, and R. Reber, "Investigation on a new high resolution wide swath SAR concept," in *Proc. Int. Geoscience and Remote Sensing Symposium IGARSS'03*, 2003.
- [51] R. T. Hoor and S. Kassam, "The unifying role of the coarray in aperture synthesis for coherent and incoherent imaging," *Proceedings of the IEEE*, vol. 78, no. 4, pp. 735–752, Apr. 1990.
- [52] S. M. Hoppe, "Untersuchung von Systemkonzepten zum Einsatz von Digital Beamforming für ACC-Sensoren," Diplomarbeit, Universität Karlsruhe (TH), 2001.

- [53] D. Hounam, E. Kemptner, G. Krieger, M. Limbach, J. Mittermayer, *et al.*, “Techniques and technologies for small SAR satellite systems,” Deutsches Zentrum für Luft- und Raumfahrt (DLR), Institut für Hochfrequenz- und Radartechnik (IHR), Tech. Note SAFARI-TN-DLR-HR 4010, Nov. 2002.
- [54] N. Kees, E. Schmidhammer, and J. Detlefsen, “Improvement of angular resolution of a millimeterwave imaging system by transmitter location multiplexing,” in *IEEE Microwave Systems Conference*, 1995.
- [55] W. Keydel, “Perspectives and visions for future SAR systems,” *IEE Proceedings for Radar, Sonar and Navigation*, vol. 150, no. 3, pp. 97–103, June 2003.
- [56] J. Kirk, “Motion compensation for synthetic aperture radar,” *IEEE Transactions on Aerospace and Electronic Systems*, vol. 11, pp. 338–348, Mar. 1975.
- [57] R. Klemm, *Principles of space-time adaptive processing*, 2nd ed. London, UK: IEE, 2002.
- [58] G. Krieger, H. Fiedler, J. Mittermayer, K. Papathanassiou, and A. Moreira, “Analysis of multistatic configurations for spaceborne SAR interferometry,” *IEE Proceedings for Radar, Sonar and Navigation*, vol. 150, no. 3, pp. 87–96, 2003.
- [59] G. Krieger, J. Mittermayer, S. Buckreuss, M. Wendler, T. Sutor, and A. Moreira, “Sector imaging radar for enhanced vision,” *Aerospace Science and Technology*, no. 7, pp. 147–158, 2003.
- [60] T. Kurpjuhn, M. Joham, W. Utschick, and J. Nosseck, “Experimental studies about eigenbeamforming in standardization MIMO channels,” in *IEEE Vehicular Technology Conference, VTC’02*, vol. 1, Sept. 2002, pp. 185–189.
- [61] R. LaBelle and C. Anderson, “Offshore oil-spill occurrence rates,” in *Proc. MTS/IEEE Prospects for the 21st Century, OCEANS ’96*, vol. 2, Sept. 1996, pp. 751–753.

-
- [62] R. Lanari, S. Zoffoli, E. Sansosti, G. Fornaro, and F. Serafino, “New approach for hybrid strip-map/spotlight SAR data focusing,” *IEEE Proceedings for Radar, Sonar and Navigation*, vol. 148, no. 6, pp. 363–372, 2001.
- [63] L. R. LeBlanc, J. M. Cuschieri, M. R. Singer, and P.-P. J. Beaujean, “Electronically steered and focused forward-looking scan sonar,” in *Proc. Autonomous Underwater Vehicle Technology, AUV’96*, vol. 1, 1996, pp. 146–153.
- [64] K. F. Lee and W. Chen, Eds., *Advances in Microstrip and Printed Antennas*. John Wiley, 1997.
- [65] A. K. Löhner, “Improved azimuthal resolution of forward looking SAR by sophisticated antenna illumination function design,” *IEEE Proceedings for Radar, Sonar and Navigation*, vol. 145, no. 2, pp. 128–134, Apr. 1998.
- [66] M. Ludwig, H.-P. Feldle, and H. Ott, “A miniaturised X-band T/R-module for SAR-systems based on active phased array techniques,” in *Proc. Int. Geoscience and Remote Sensing Symposium IGARSS’95*, vol. 3, 1995, pp. 2063–2065.
- [67] R. J. Mailloux, *Phased Array Antenna Handbook*. Artech House, 1994.
- [68] D. Massonnet, “Capabilities and limitations of the interferometric cartwheel,” *IEEE Transactions on Geoscience and Remote Sensing*, vol. 39, no. 3, pp. 506–520, Mar. 2001.
- [69] R. E. McIntosh, S. J. Frasier, and J. B. Mead, “FOPAIR: A focused array imaging radar for ocean remote sensing,” *IEEE Transactions on Geoscience and Remote Sensing*, vol. 33, no. 1, pp. 115–124, 1995.
- [70] W. L. Melvin, “A STAP overview,” *IEEE Aerospace and Electronics Systems Magazine*, vol. 19, no. 1, pp. 19–35, Jan. 2004.
- [71] D. L. Mensa, *High Resolution Radar Imaging*. Artech House, 1981.
- [72] J. Mittermayer, M. Wendler, G. Krieger, A. Moreira, T. Sutor, and S. Buckreuss, “Data processing for an innovative forward looking SAR system for enhanced vision,” in *Proc. European Conference on Synthetic*

Aperture Radar EUSAR'2000, Munich, Germany, May 2000, pp. 733–736.

- [73] A. Moccia, N. Chiacchio, and A. Capone, “Spaceborne bistatic synthetic aperture radar for remote sensing applications,” *International Journal of Remote Sensing*, vol. 21, no. 18, pp. 3395–3414, 2000.
- [74] A. Moreira, “Radar mit synthetischer Apertur,” Habilitationsschrift, Universität Karlsruhe (TH), 2000.
- [75] A. Moreira, “SAR remote sensing using new techniques and technologies: Strategy discussion,” Deutsches Zentrum für Luft- und Raumfahrt (DLR),” Tech. Note, May 2000.
- [76] A. Moreira and Y. Huang, “Airborne SAR processing of highly squinted data using a chirp scaling algorithm with integrated motion compensation,” *IEEE Transactions on Geoscience and Remote Sensing*, vol. 32, no. 4, pp. 1029–1040, July 1994.
- [77] A. V. Oppenheim and R. W. Schaffer, *Zeitdiskrete Signalverarbeitung*, 3rd ed. R. Oldenbourg Verlag, 1999.
- [78] A. Papoulis, *Systems and Transforms with Applications in Optics*. New York: McGraw-Hill, 1968.
- [79] J. G. Proakis, *Digital Communications*, 2nd ed. McGraw-Hill, 1989.
- [80] R. K. Raney, “Synthetic aperture imaging radar and moving targets,” *IEEE Transactions on Aerospace and Electronic Systems*, vol. 7, no. 3, pp. 499–505, 1971.
- [81] R. Rieger, B. Schweizer, H. Dreher, R. Reber, M. Adolph, and H.-P. Feldle, “Highly integrated cost-effective standard X-band T/R module using LTCC housing concept for automated production,” in *Proc. European Conference on Synthetic Aperture Radar EUSAR'2002*, Koeln, Germany, June 2002, pp. 303–306.
- [82] J. Rosello-Guasch, “Technology for processing on-board SAR data,” *Preparing for the Future, ESA Newsletter on Industrial Matters & Technology Programmes*, vol. 6, no. 2, June 1996. [Online]. Available: <http://esapub.esrin.esa.it/pff/futuv6n2.htm>

- [83] F. Rostan, “Dual polarisierte Microstrip-Patch-Arrays für zukünftige satelliten-gestützte SAR-Systeme,” Ph.D. dissertation, Institut für Höchstfrequenztechnik und Elektronik, Universität Karlsruhe, June 1996.
- [84] A. Roth, “TerraSAR-X: a new perspective for scientific use of high resolution spaceborne SAR data,” in *GRSS/ISPRS Joint Workshop on Remote Sensing and Data Fusion over Urban Areas*, May 2003, pp. 4–7.
- [85] C. Schaefer, M. Süß, and M. Gottwald, “Compression of SAR raw data using the method of BABC,” in *Proc. European Conference on Synthetic Aperture Radar EUSAR’2000*, May 2000.
- [86] M. Schwäbisch and J. Moreira, “The high resolution airborne interferometric SAR AeS-1,” in *Proc. 4th International Airborne Remote Sensing Conference*, vol. 1, 1999, pp. 540–547.
- [87] M. Schwartz, *Information Transmission, Modulation, and Noise*, 4th ed. McGraw-Hill, 1990.
- [88] M. Skolnik, *Introduction to Radar Systems*, 3rd ed. McGraw-Hill, 2001.
- [89] M. Soumekh, “Bistatic synthetic aperture radar inversion with application in dynamic object imaging,” *IEEE Transactions on Signal Processing*, vol. 39, no. 9, pp. 2044–2055, Sept. 1991.
- [90] M. Soumekh, “A system model and inversion for synthetic aperture radar imaging,” *IEEE Transactions on Image Processing*, vol. 1, no. 1, pp. 64–76, Jan. 1992.
- [91] M. Soumekh, “Digital spotlighting and coherent subaperture image formation for stripmap synthetic aperture radar,” in *IEEE International Conference on Image Processing, ICIP-94*, vol. 1, Nov. 1994, pp. 476–480.
- [92] M. Soumekh, *Synthetic Aperture Radar Signal Processing with MATLAB Algorithms*. John Wiley, 1999.
- [93] U. Stein and M. Younis, “Suppression of range ambiguities in synthetic aperture radar systems,” in *Proc. IEEE International Conference on Computer as a Tool EUROCON’03*, vol. 2, Ljubljana, Slovenia, Sept. 2003, pp. 417–421.

- [94] U. Stein, “Untersuchung von Verfahren zum Einsatz von Digital Beamforming in der Fernerkundung,” Diplomarbeit, Universität Karlsruhe (TH), 2002.
- [95] B. D. Steinberg, “Digital beamforming in ultrasound,” *Digital beamforming in ultrasound IEEE Transactions on Ultrasonics Ferroelectrics and Frequency Control*, vol. 39, no. 6, pp. 716–721, Nov. 1992.
- [96] B. D. Steinberg and H. M. Subbaram, *Microwave Imaging Techniques*. John Wiley, 1991.
- [97] H. Steyskal and J. F. Rose, “Digital beamforming for radar systems,” *Microwaves Journal*, pp. 121–136, Jan. 1989.
- [98] F. G. Stremmer, *Introduction to Communication Systems*, 2nd ed. Addison-Wesley, 1982.
- [99] R. J. Sullivan, *Microwave Radar: imaging and advanced concepts*. Norwood, MA: Artech House, 2000.
- [100] H. Süß, R. Schröder, and K.-H. Wägel, “Applications of small SAR satellite systems,” Deutsches Zentrum für Luft- und Raumfahrt (DLR), Institut für Hochfrequenz- und Radartechnik (IHR), Tech. Note SAFARI-TN-DLR-HR 4030, Dec. 2002.
- [101] M. Süß, B. Grafmüller, and R. Zahn, “A novel high resolution, wide swath SAR,” in *Proc. Int. Geoscience and Remote Sensing Symposium IGARSS’01*, vol. 3, 2001, pp. 1013–1015.
- [102] M. Süß, C. Schaefer, and R. Zahn, “The technology development of a spaceborne on-board SAR-processor and storage demonstrator,” in *Committee on Earth Observation Satellites Workshop, CEOS’99*, Aug. 1999. [Online]. Available: <http://www.estec.esa.nl/ceos99/papers/p006.pdf>
- [103] M. Süß, C. Schaefer, and R. Zahn, “Discussion of the introduction of on-board SAR data processing to spaceborne SAR instruments,” in *Proc. Int. Geoscience and Remote Sensing Symposium IGARSS’00*, vol. 5, 2000, pp. 2331–2333.

-
- [104] T. Sutor, S. Buckreuss, M. Wendler, and F. Witte, "SIREV: Sector Imaging Radar for Enhanced Vision," in *Proc. of the 3rd European Conference on Synthetic Aperture Radar*, Munich, Germany, May 2000, pp. 357–359.
- [105] K. Teitelbaum, "A flexible processor for a digital adaptive array radar," *IEEE Aerospace and Electronics Systems Magazine*, vol. 6, no. 5, pp. 18–22, May 1991.
- [106] I. E. Telatar, "Capacity of multi-antenna Gaussian channels," *European Transactions on Telecommunications*, vol. 10, no. 6, pp. 585–595, Nov. 1999, first published as tech. memorandum, Bell laboratories, Lucent technologies, october 1995.
- [107] K. Tomiyasu, "Performance of a proposed spaceborne synthetic aperture radar with variable antenna height," *IEEE Transactions on Geoscience and Remote Sensing*, vol. 28, no. 4, pp. 609–613, July 1990.
- [108] F. T. Ulaby, R. K. Moore, and A. K. Fung, "Microwave remote sensing fundamentals and radiometry," in *Microwave Remote Sensing Active and Passive*. Addison-Wesley, 1981, vol. 1.
- [109] F. T. Ulaby, R. K. Moore, and A. K. Fung, "Radar remote sensing and surface scattering and emission theory," in *Microwave Remote Sensing Active and Passive*. Addison-Wesley, 1982, vol. 2.
- [110] Y. Venot, M. Younis, and W. Wiesbeck, "Realisation of a compact forward looking sar with digital beamforming on receive only," *Frequenz Journal of Telecommunications*, vol. 55, no. 3-4, pp. 85–90, Mar. 2001.
- [111] Y. Venot, M. Younis, and W. Wiesbeck, "Compact forward looking SAR using digital beamforming on-receive-only," in *Proc. European Conference on Synthetic Aperture Radar EUSAR'2000*, May 2002, pp. 795–798.
- [112] W. Wiesbeck, "SDRS: software-defined radar sensors," in *Proc. Int. Geoscience and Remote Sensing Symposium IGARSS'2001*, vol. 7, Sydney, Australia, July 2001, pp. 3259–3261.
- [113] C. A. Wiley, "Pulsed doppler radar methods and apparatus," U.S. Patent 3.196.436, 1954.

- [114] N. J. Willis, *Bistatic Radar*. Artech House, 1991.
- [115] J. J. W. Wilson, "A design procedure for the design of advanced coded pulse radar waveforms generated from a finite set of samples," in *IEEE Colloquium on Recent Developments in Image Processing: Applications in Remote Sensing*, vol. 1, 1990, pp. 6/1–6/7.
- [116] C. Wimmer, R. Siegmund, M. Schwäbisch, and J. Moreira, "Generation of high precision DEMs of the Wadden sea with airborne interferometric SAR," *IEEE Transactions on Geoscience and Remote Sensing*, vol. 38, no. 5, pp. 2234–2245, Sept. 2000.
- [117] V. Wismann, M. Gade, W. Alpers, and H. Huhnerfuss, "Radar signatures of mineral oil spills measured by an airborne multi-frequency multi-polarization microwave scatterometer," in *Proc. Engineering in Harmony with Ocean, OCEANS'93*, vol. 2, Oct. 1993, pp. II348–II353.
- [118] F. Witte, "Vorwärtssicht-Radar," Bundesrepublik Deutschland Patent DE 4 007 611 C1, May 16, 1991.
- [119] F. Witte, "Forward looking airborne radar in combination with downward and side looking sensors," in *Proc. of IEEE Topical Symposium on Combined Optical, Microwave, Earth and Atmosphere Sensing*, Mar. 1993, pp. 155–158.
- [120] S. Young, S. Harrah, and M. de Haag, "Real-time integrity monitoring of stored geo-spatial data using forward-looking remote sensing technology," in *Proc. 21st Digital Avionics Systems Conference*, vol. 2, 2002, pp. 11D1–1 – 11D1–10.
- [121] M. Younis, M. Baldauf, and W. Wiesbeck, *Advanced Radio Communication I*. Lecture notes, Institut für Höchsthfrequenztechnik und Elektronik der Universität Karlsruhe, WS 2003/2004.
- [122] M. Younis, C. Fischer, and W. Wiesbeck, "An evaluation of performance parameters of software defined radar sensors," in *Proc. European Conference on Synthetic Aperture Radar EUSAR'2002*, June 2002.
- [123] M. Younis, C. Fischer, and W. Wiesbeck, "Digital beamforming in SAR systems," *IEEE Transactions on Geoscience and Remote Sensing*, vol. 41, no. 7, pp. 1735–1739, July 2003.

- [124] M. Younis, Y. Venot, and W. Wiesbeck, "A 56-beam antenna for synthetic aperture radar applications," in *Proc. German Radar Symposium GRS*, Berlin, Germany, Oct. 2000, pp. 327–330.
- [125] M. Younis, Y. Venot, and W. Wiesbeck, "Active antenna array for forward looking SAR," in *Proc. Millennium Conference on Antennas & Propagation AP'2000, Davos, Switzerland*, Apr. 2000.
- [126] M. Younis, C. Waldschmidt, and W. Wiesbeck, "A closed expression for the maximum unambiguous angular segment of nonuniform linear arrays," in *XXVIIth General Assembly of the International Union of Radio Science URSI-GA, Maastricht, Netherlands*, 2002.
- [127] M. Younis and W. Wiesbeck, "SAR with digital beamforming on receive only," in *Proc. Int. Geoscience and Remote Sensing Symposium IGARSS'99*, vol. 3, Hamburg, Germany, June 1999, pp. 1773–1775.
- [128] M. Younis and W. Wiesbeck, "Antenna system for a forward looking SAR using digital beamforming on-receive-only," in *Proc. Int. Geoscience and Remote Sensing Symposium IGARSS'2000*, vol. 5, Honolulu, Hawaii, July 2000, pp. 2343–2345.
- [129] M. Zink, R. Torres, C. Buck, B. Rosich, and J. Closa, "The advanced SAR system on ENVISAT: mission status," in *Proc. European Conference on Synthetic Aperture Radar EUSAR'2002*, Koeln, Germany, June 2002, pp. 175–177.

A Correlation of Chirp Waveforms

The purpose is to find a solution for the general cross-correlation function between two arbitrary chirps defined in (2.14) and (2.15). In addition a closed expression is derived for the auto-correlation function (2.10) of two identical chirp waveforms.

A.1 General Formulation

The correlation between two signals $f(t)$ and $g(t)$ is defined as [98].

$$\int_{-\infty}^{+\infty} f^*(t)g(t + \tau)dt = \int_{-\infty}^{+\infty} f^*(t - \tau)g(t)dt. \quad (\text{A.1})$$

In the following the time delay τ_n is not considered here, since its only contribution is a shift in the resultant curve on the time axis. Inserting $h_{t_1}(t)$ and $h_{t_2}(t)$ into the above gives

$$\begin{aligned} R(\tau) &= \int_{-\infty}^{+\infty} h_{t_1}^*(t)h_{t_2}(t + \tau)dt \quad (\text{A.2}) \\ &= \int_{t_1}^{t_2} \exp\left(-j2\pi f_{s1}t - j2\pi k_{e1}t^2\right) \cdot \\ &\quad \exp\left(+j2\pi f_{s2}(t + \tau) + j2\pi k_{e2}(t + \tau)^2\right) dt \\ &= \int_{t_1}^{t_2} \exp\left(j2\pi\left(-f_{s1}t - k_{e1}t^2 + f_{s2}t + f_{s2}\tau + k_{e2}t^2 + k_{e2}\tau^2 + k_{e2}t\tau\right)\right) dt \end{aligned}$$

where the integration limits t_1 and t_2 were introduced; their values must be such that the integration is over non-vanishing integrands. Multiplying the integrand by

$$\exp\left(j\pi\frac{(f_{s2} + 2k_{e2}\tau - f_{s1})^2}{2(k_{e2} - k_{e1})}\right) \cdot \exp\left(-j\pi\frac{(f_{s2} + 2k_{e2}\tau - f_{s1})^2}{2(k_{e2} - k_{e1})}\right) \equiv 1 \quad (\text{A.3})$$

which corresponds to a quadratic expansion and moving all t -independent terms outside the integral results in

$$R(\tau) = \exp\left(j2\pi f_{s2}\tau + j2\pi k_{e2}\tau^2 - j\pi\frac{(f_{s2} + 2k_{e2}\tau - f_{s1})^2}{2(k_{e2} - k_{e1})}\right) \cdot \int_{t_1}^{t_2} \exp\left(j\frac{\pi}{2}\left(\frac{f_{s2} + 2k_{e2}\tau - f_{s1}}{\sqrt{k_{e2} - k_{e1}}} + 2\sqrt{k_{e2} - k_{e1}}t\right)^2\right) dt. \quad (\text{A.4})$$

The integral can be rewritten by using the substitution

$$\nu(t) = \frac{f_{s2} + 2k_{e2}\tau - f_{s1}}{\sqrt{k_{e2} - k_{e1}}} + 2\sqrt{k_{e2} - k_{e1}}t \quad (\text{A.5})$$

$$d\nu = 2\sqrt{k_{e2} - k_{e1}}dt \quad (\text{A.6})$$

which gives

$$R(\tau) = \underbrace{\frac{\exp\left(j2\pi f_{s2}\tau + j2\pi k_{e2}\tau^2 - j\pi\frac{(f_{s2} + 2k_{e2}\tau - f_{s1})^2}{2(k_{e2} - k_{e1})}\right)}{2\sqrt{k_{e2} - k_{e1}}}}_{K(\tau)} \int_{\nu(t_1)}^{\nu(t_2)} \exp\left(+j\frac{\pi}{2}\nu^2\right) d\nu \quad (\text{A.7})$$

The integral in the above expression is similar to the *Fresnel Integral* defined by [2]

$$C(\nu) + jS(\nu) = \int_0^\nu \exp\left(+j\frac{\pi}{2}u^2\right) du \quad (\text{A.8})$$

for real valued functions $C(\nu)$ and $S(\nu)$. Writing the correlation function (A.7) in terms of the Fresnel Integrals finally gives

$$R(\tau) = K(\tau) \left[C(\nu(t_2)) + jS(\nu(t_2)) - C(\nu(t_1)) - jS(\nu(t_1)) \right]. \quad (\text{A.9})$$

It remains to determine the integral limits. The values of t_1 and t_2 depend on the range of the variable τ . Two cases are recognized:

$$\begin{aligned}
0 \leq \tau \leq T_p \quad \nu(t_1 = 0) &= \frac{f_{s2} + 2k_{e2}\tau - f_{s1}}{\sqrt{k_{e2} - k_{e1}}} \\
\nu(t_2 = T_p - \tau) &= \frac{2(k_{e2} - k_{e1})(T_p - \tau) + f_{s2} + 2k_{e2}\tau - f_{s1}}{\sqrt{k_{e2} - k_{e1}}}
\end{aligned}$$

and

$$\begin{aligned}
-T_p \leq \tau \leq 0 \quad \nu(t_1 = -\tau) &= \frac{-2(k_{e2} - k_{e1})\tau + f_{s2} + 2k_{e2}\tau - f_{s1}}{\sqrt{k_{e2} - k_{e1}}} \\
\nu(t_2 = T_p) &= \frac{2(k_{e2} - k_{e1})T_p + f_{s2} + 2k_{e2}\tau - f_{s1}}{\sqrt{k_{e2} - k_{e1}}}
\end{aligned}$$

the correlation $R(\tau) = 0$ outside the interval $-T_p < \tau < +T_p$.

A.2 Cross-Correlation

The general form of the correlation function (A.7) diverges for $k_{e2} = k_{e1}$. To find the correlation function for two chirps of identical chirp rate, the expression (A.2) is rewritten using $k_{e2} = k_{e1} = k_e$ to yield

$$\begin{aligned}
R(\tau) &= \int_{t_1}^{t_2} \exp\left(j2\pi(-f_{s1}t + f_{s2}t + f_{s2}\tau + k_e\tau^2 + 2k_e t\tau)\right) dt \quad (\text{A.10}) \\
&= \exp\left(j2\pi f_{s2}\tau + j2\pi k_e\tau^2\right) \int_{t_1}^{t_2} \exp\left(j2\pi(f_{s2} - f_{s1})t + j4\pi k_e t\tau\right) dt
\end{aligned}$$

where the integral limits t_1 and t_2 depend on the value of τ . The above integral is split up into

$$\begin{aligned}
I1 &= \int_0^{T_p - \tau} \exp\left(j2\pi(f_{s2} - f_{s1})t + j4\pi k_e t\tau\right) dt \\
&= \frac{\exp\left(j2\pi(f_{s2} - f_{s1} + 2k_e\tau)(T_p - \tau)\right) - 1}{j2\pi(f_{s2} - f_{s1} + 2k_e\tau)}
\end{aligned}$$

for $0 < \tau < T_p$, and

$$\begin{aligned}
I2 &= \int_{-\tau}^{T_p} \exp\left(j2\pi(f_{s2} - f_{s1})t + j4\pi k_e t\tau\right) dt \\
&= \frac{\exp\left(j2\pi(f_{s2} - f_{s1} + 2k_e\tau)T_p\right) - \exp\left(-j2\pi(f_{s2} - f_{s1} + 2k_e\tau)\tau\right)}{j2\pi(f_{s2} - f_{s1} + 2k_e\tau)}
\end{aligned}$$

for $-T_p < \tau < 0$, whereas $I3 = 0$ otherwise. The above results together with (A.10) are written in a compact form yielding

$$\begin{aligned}
R(\tau) &= \frac{\sin(\pi(f_{s2} - f_{s1} + 2k_e\tau)(T_p - |\tau|))}{\pi(f_{s2} - f_{s1} + 2k_e\tau)} \\
&\quad \exp\left(+j\pi((f_{s2} - f_{s1})T_p + (f_{s2} + f_{s1})\tau + 2k_e T_p \tau)\right) \text{rect}\left[\frac{|\tau|}{T_p}\right].
\end{aligned} \tag{A.11}$$

A.3 Auto-Correlation

The auto-correlation function (2.10) given by

$$R(\tau) = \int_{-\infty}^{+\infty} e^{-j2\pi k_e t^2} \text{rect}\left[\frac{t}{T_p}\right] e^{+j2\pi k_e (t+\tau-\tau_n)^2} \text{rect}\left[\frac{t+\tau-\tau_n}{T_p}\right] dt \tag{A.12}$$

Expanding the $(t + \tau - \tau_n)^2$ term and simplifying gives

$$R(\tau) = e^{+j2\pi k_e (\tau - \tau_n)^2} \int_{-\infty}^{+\infty} e^{+j4\pi k_e t(\tau - \tau_n)} \text{rect}\left[\frac{t}{T_p}\right] \text{rect}\left[\frac{t+\tau-\tau_n}{T_p}\right] dt. \tag{A.13}$$

In the above expression the integral limits depend on the value of $\tau - \tau_n$ through the rect-function. The integration is split up into

$$I1 = \int_0^{-(\tau-\tau_n)+T_p} e^{+j4\pi k_e (\tau - \tau_n)t} dt = \frac{e^{j4\pi k_e (\tau - \tau_n)(T_p - (\tau - \tau_n))} - 1}{j4\pi k_e (\tau - \tau_n)}$$

for $0 < \tau - \tau_n < T_p$, and

$$I2 = \int_{-(\tau-\tau_n)}^{T_p} e^{+j4\pi k_e(\tau-\tau_n)t} dt = \frac{e^{j4\pi k_e(\tau-\tau_n)T_p} - e^{-j4\pi k_e(\tau-\tau_n)^2}}{j4\pi k_e(\tau - \tau_n)}$$

for $-T_p < \tau - \tau_n < 0$, whereas $I3 = 0$ otherwise.

The result can be written in a compact form given by:

$$R(\tau) = \frac{\sin(2\pi k_e(T_p|\tau - \tau_n| - (\tau - \tau_n)^2))}{2\pi k_e(\tau - \tau_n)} e^{+j2\pi k_e T_p(\tau - \tau_n)} \text{rect}\left[\frac{|\tau - \tau_n|}{T_p}\right]. \quad (\text{A.14})$$

B Relevant Orbital Geometry and Mechanics

B.1 Spacecraft Velocity for Circular Orbits

The linear velocity V of the spacecraft of mass m_a in a circular orbit around a spherical homogeneous earth (see Fig. B.1) can be derived from the inward gravitational force F_g and the outward centrifugal force F_c given by:

$$F_g = m_a g_s \left(\frac{R_{\text{earth}}}{R_{\text{orbit}}} \right)^2 \quad \text{and} \quad (\text{B.1})$$

$$F_c = \frac{m_a V^2}{R_{\text{orbit}}}, \quad (\text{B.2})$$

respectively. In the above g_s is the surface gravity constant $g_s = 9.81 \text{ m/s}^2$; while R_{earth} and R_{orbit} are the earth and orbit radii, respectively. For a stable orbit the two forces are equal and thus

$$F_g \stackrel{!}{=} F_c \quad \Rightarrow \quad V = \sqrt{\frac{g_s R_{\text{earth}}^2}{R_{\text{orbit}}}}. \quad (\text{B.3})$$

B.2 Slant-Range Distance for Curved Earth

The purpose is to determine the slant-range R_s as a function of the local angle of incidence ϑ_1 and the orbit height H_{orbit} . With reference to the triangle ABC

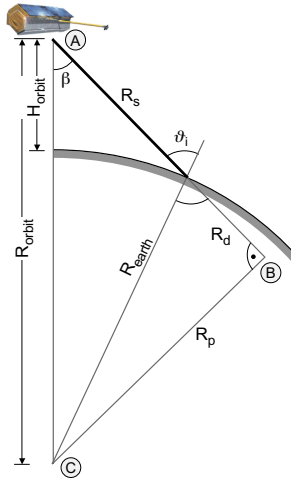


Figure B.1: Geometry of satellite orbit and local angle of incidence on the curved Earth

in Fig. B.1

$$R_{\text{orbit}}^2 = (R_s + R_d)^2 + R_p^2$$

$$\Rightarrow R_s = \sqrt{R_{\text{orbit}}^2 - R_p^2} - R_d \quad (\text{B.4})$$

where $R_{\text{orbit}} = H_{\text{orbit}} + R_{\text{earth}}$ is the orbit's radius. Writing R_d and R_p in terms of the local Earth radius R_{earth} and the angle of incidence gives

$$R_p = R_{\text{earth}} \cdot \sin \vartheta_i \quad (\text{B.5})$$

$$R_d = R_{\text{earth}} \cdot \cos \vartheta_i. \quad (\text{B.6})$$

Inserting into (B.4) gives

$$R_s = \sqrt{R_{\text{orbit}}^2 - R_{\text{earth}}^2 \sin^2 \vartheta_i} - R_{\text{earth}} \cos \vartheta_i \quad (\text{B.7})$$

which when written in terms of the orbit height H_{orbit} and after simplification yields

$$R_s = \sqrt{H_{\text{orbit}}^2 + 2H_{\text{orbit}}R_{\text{earth}} + R_{\text{earth}}^2 \cos^2 \vartheta_i} - R_{\text{earth}} \cos \vartheta_i. \quad (\text{B.8})$$

C Spatial Fourier Transform of Spherical Phase SAR Signals

The appendix describes how to use the asymptotic evaluation of integrals and specifically the method of stationary phase in order to solve the spatial Fourier transform integral of the spherical phase function common to the signals of SAR systems.

C.1 Asymptotic Evaluation of Integrals

The aim is to solve the spatial domain Fourier integral in (4.10) given by

$$\int_{-L/2}^{+L/2} \exp\left(-j2k\sqrt{x^2 + (y - u - \alpha v)^2} - jk_u u\right) \cdot \exp\left(+jk\frac{(y - u)(1 - 2\alpha)}{(x^2 + (y - u)^2)^{\frac{1}{2}}}v - jk\frac{x^2(1 - 2\alpha^2)}{2(x^2 + (y - u)^2)^{\frac{3}{2}}}v^2\right) du. \quad (\text{C.1})$$

The first exponent of the above integrand is a *fast* varying term with respect to the variable u . The fast varying term is given in (C.2) by $w(u)$. The second exponential term varies slowly, because of the large value of x^2 and y^2 in the denominators of the exponent; this term is the *slow* varying term as given in (C.3). As an example, Fig. C.1 shows one possible plot of the two terms.

$$\exp(-jw(u) - jk_u u) = \exp\left(-j2k\sqrt{x^2 + (y - u - \alpha v)^2} - jk_u u\right) \quad (\text{C.2})$$

$$W(u) = \exp\left(+jk\frac{(y - u)(1 - 2\alpha)}{(x^2 + (y - u)^2)^{\frac{1}{2}}}v - jk\frac{x^2(1 - 2\alpha^2)}{2(x^2 + (y - u)^2)^{\frac{3}{2}}}v^2\right). \quad (\text{C.3})$$

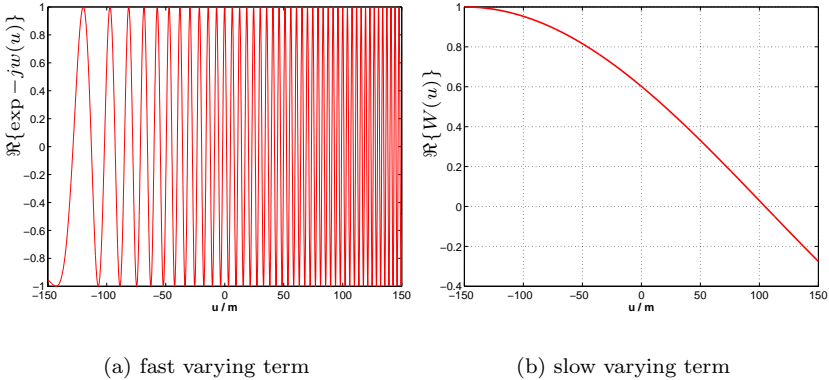


Figure C.1: Comparison of the slow and fast varying terms of the integral in (C.1) as defined in (C.2) and (C.3). The parameters are $x = 8$ km, $y = 150$ m and $\alpha = 0.35$

This type of integral can be solved using an asymptotic evaluation [78]. Suppose that $w(u)$ has a maximum at the point u_s on the integration path; at this point the derivative is zero and thus the variation of $w(u)$ in the vicinity of u_s is small. It follows that the oscillation of $\exp w(u_s)$ is small near u_s . The idea behind the *method of stationary phase* is to approximate the integral by the path contributions in the vicinity of u_s only, since the contribution from the remainder of the path will be negligible, due to the high oscillation of $w(u)$ between its positive and negative extrema. If $W(u)$ is regular and slowly varying in the vicinity of u_s as compared to $w(u)$ it may be approximated by $W(u_s)$ and taken outside the integral. Approximate integration of the remaining term can be achieved by expanding $w(u_s)$ in a power series about u_s and retaining only the first few terms, such that the remaining integral can be converted into a form, which can be solved analytically.

The *stationary* or *saddle points* are found by differentiating the fast term with respect to u and equating the result to zero

$$\frac{\partial}{\partial u}(-w(u) - k_u u) = \frac{2k(y - u - \alpha v)}{\sqrt{x^2 + (y - u - \alpha v)^2}} - k_u \stackrel{!}{=} 0. \quad (\text{C.4})$$

Solving for the stationary points $u = u_s$ results in

$$u_s = y - \alpha v \pm \frac{k_u x}{\sqrt{4k^2 - k_u^2}}. \quad (\text{C.5})$$

It is only in the vicinity of these points that the integral needs to be evaluated. When u_s is inserted into the slow varying term, the function $W(u_s)$ can be drawn outside the integral¹. The fast varying term is expanded into a Taylor series in the neighborhood of the stationary points (third and higher order terms are neglected)

$$w(u) + k_u u \approx w(u_s) + k_u u_s + \frac{1}{2} w''(u_s)(u - u_s)^2 \quad (\text{C.6})$$

where $w''(u_s)$ is the second derivative with respect to u at the point u_s and is given by

$$w''(u_s) = \frac{2kx^2}{(x^2 + (y - u_s - \alpha v)^2)^{\frac{3}{2}}} = \frac{(4k^2 - k_u^2)^{\frac{3}{2}}}{x(2k)^2} > 0 \quad (\text{C.7})$$

Note that the first derivative is zero for $u = u_s$, i.e., when $w'(u_s) = 0$. Inserting (C.6) and $W(u_s)$ into (C.1) gives

$$W(u_s) \cdot \exp(-jw(u_s) - jk_u u_s) \int_{-\infty}^{+\infty} \exp\left(-j \frac{w''(u_s)}{2} (u - u_s)^2\right) du \quad (\text{C.8})$$

The limits of the above integral have been extended to infinity, since the main contribution comes from the vicinity of u_s where the exponential term is varying slowly, hence extending the limits has no influence on the result.

¹The integral to be solved after drawing out the slow varying (i.e., *bi-static phase*) term is identical to the integral that would result from the mono-static configuration. Hence, when comparing the mono-static and bi-static cases the remaining integral need not be evaluated, once $W(u_s)$ is obtained. Nevertheless, the solution is stated here for completeness.

Next a variable transformation $u - u_s$ to ν is introduced, giving

$$\begin{aligned} \frac{w''(u_s)}{2}(u - u_s)^2 &= \frac{\pi}{2}\nu^2 \\ du &= \sqrt{\frac{\pi}{w''(u_s)}}d\nu \end{aligned} \quad (\text{C.9})$$

which when inserted into (C.8) gives (note that the integral is symmetric about $\nu = 0$)

$$W(u_s) \cdot \exp(-jw(u_s) - jk_u u_s) \cdot 2\sqrt{\frac{\pi}{w''(u_s)}} \int_0^{+\infty} \exp\left(-j\frac{\pi}{2}\nu^2\right) d\nu. \quad (\text{C.10})$$

The integral is recognized as being the complex Fresnel integral [45], the solution of which is known [2]

$$\int_0^{+\infty} \exp\left(-j\frac{\pi}{2}\nu^2\right) d\nu = \frac{1}{\sqrt{2}} \exp\left(-j\frac{\pi}{4}\right). \quad (\text{C.11})$$

Substituting the above and u_s from (C.5) into (C.10) finally gives

$$W(u_s) \cdot k\sqrt{\frac{2\pi x}{(4k^2 - k_u^2)^{\frac{3}{2}}}} \exp\left(-j\sqrt{4k^2 - k_u^2}x - jk_u(y - \alpha v) - j\frac{\pi}{2}\right). \quad (\text{C.12})$$

C.2 Determining the Slow Varying Term

The value of $W(u_s)$ is determined by substituting (C.5) into (C.3) which gives

$$W(u_s) = \exp\left(+jk\frac{(1 - 2\alpha)v}{(1 + (x/\xi)^2)^{\frac{1}{2}}}\right) \cdot \exp\left(-jk\frac{x^2(1 - 2\alpha^2)v^2}{2(x^2 + \xi^2)^{\frac{3}{2}}}\right) \quad (\text{C.13})$$

where the substitution

$$\xi = \alpha v \pm \frac{k_u x}{\sqrt{4k^2 - k_u^2}} \quad (\text{C.14})$$

is introduced.

For airborne or spaceborne SAR systems the range x is in the order of tens of kilometers while the value of αv is in the order of a few meters. This validates the approximation

$$\xi \approx \pm \frac{k_u x}{\sqrt{4k^2 - k_u^2}} \quad (\text{C.15})$$

which when inserted into (C.13) gives

$$W(u_s) = \exp\left(+jk_u \frac{(1-2\alpha)v}{2}\right) \cdot \exp\left(-jk \frac{(1-2\alpha^2)v^2}{16x} \left(\frac{4k^2 - k_u^2}{k^2}\right)^{\frac{3}{2}}\right) \quad (\text{C.16})$$

Curriculum Vitae

Persönliche Daten

Name: Marwan Younis
Geburtsdatum: 7. April 1970
Geburtsort: Las Cruces, New Mexico, USA
Staatsangehörigkeit: US. Amerikanisch
Familienstand: ledig

Schulbildung

1976 - 1982 Grundschule, Bagdad, Irak
1982 -1988 Gymnasium *Baghdad College*, Bagdad, Irak

Studium und Berufsweg

1988 - 1992 Studium *Electrical Engineering* an der *University of Baghdad*, Irak
Juni 1992 Studienabschluss: *Bachelor of Science* (B.Sc.)
1993 - 1997 Studium der Elektrotechnik an der Universität Karlsruhe (TH)
Schwerpunkt: Nachrichten- und Hochfrequenztechnik
1996 Praktikum JPL/NASA, Pasadena Kalifornien
Dez. 1997 Diplom in Elektrotechnik an der Universität Karlsruhe
seit 1998 Wissenschaftlicher Angestellter am Institut für Höchstfrequenztechnik und Elektronik (IHE) der Universität Karlsruhe. Mitarbeit in Forschung und Lehre

